Site U1423[1]

R. Tada, R.W. Murray, C.A. Alvarez Zarikian, W.T. Anderson Jr., M.-A. Bassetti, B.J. Brace, S.C. Clemens, M.H. da Costa Gurgel, G.R. Dickens, A.G. Dunlea, S.J. Gallagher, L. Giosan, A.C.G. Henderson, A.E. Holbourn, K. Ikehara, T. Irino, T. Itaki, A. Karasuda, C.W. Kinsley, Y. Kubota, G.S. Lee, K.E. Lee, J. Lofi, C.I.C.D. Lopes, L.C. Peterson, M. Saavedra-Pellitero, T. Sagawa, R.K. Singh, S. Sugisaki, S. Toucanne, S. Wan, C. Xuan, H. Zheng, and M. Ziegler[2]

Chapter contents

[1]Tada, R., Murray, R.W., Alvarez Zarikian, C.A., Anderson, W.T., Jr., Bassetti, M.-A., Brace, B.J., Clemens, S.C., da Costa Gurgel, M.H., Dickens, G.R., Dunlea, A.G., Gallagher, S.J., Giosan, L., Henderson, A.C.G., Holbourn, A.E., Ikehara, K., Irino, T., Itaki, T., Karasuda, A., Kinsley, C.W., Kubota, Y., Lee, G.S., Lee, K.E., Lofi, J., Lopes, C.I.C.D., Peterson, L.C., Saavedra-Pellitero, M., Sagawa, T., Singh, R.K., Sugisaki, S., Toucanne, S., Wan, S., Xuan, C., Zheng, H., and Ziegler, M., 2015. Site U1423. *In* Tada, R., Murray, R.W., Alvarez Zarikian, C.A., and the Expedition 346 Scientists, *Proc. IODP,* 346: College Station, TX (Integrated Ocean Drilling Program). doi:10.2204/iodp.proc.346.104.2015
[2]**Expedition 346 Scientists' addresses.**

Background and objectives

Integrated Ocean Drilling Program (IODP) Site U1423 is in the northeastern part of the marginal sea surrounded by the Japanese Islands, the Korean Peninsula, and the Eurasian continent at 41°41.95′N, 139°4.98′E and 1785 meters below sea level. The site is ~130 km south of Ocean Drilling Program (ODP) Site 796 and ~100 km northwest of the entrance of the Tsugaru Strait (Fig. **F1**). Site U1423 is situated on a terrace on the middle of the slope from Oshima Island, a small volcanic island 30 km to the southeast. The site is under the direct influence of the Tsushima Warm Current (TWC) that flows further north beyond the Tsugaru Strait toward the Soya Strait (Yoon and Kim, 2009). Because the sill depth of the Soya Strait is only 55 m, the influence of the TWC on the site should have been significantly affected by glacioeustatic sea level changes during the Quaternary. Although Site U1423 is relatively close to Site 796, the tectonic setting of the two sites seems different. Site 796 has been directly influenced by west–east compression caused by incipient subduction along the nearby plate boundary between the North American and Eurasian plates (Tada, 1994). In contrast, Site U1423 seems less influenced by this compression because seismic profiles suggest conformable deposition for at least for the last ~5 m.y. (upper 300 m of sediment). Relatively low linear sedimentation rates (LSRs) are anticipated based on results from the site survey. The rates are likely to be low enough to detect the contribution of eolian dust from the Asian continent. Analyses of a site survey core confirm occasional dropstones in the upper 150 m of the sequence, suggesting its appropriateness for studies of ice-rafted debris (IRD).

Site U1423 is the middle site of the northern half of the latitudinal transect targeted by IODP Expedition 346 and is also the middle depth site of the depth transect. The location of Site U1423 in the northern part of the marginal sea was selected to identify the spatial extent of IRD events and their temporal variations. Because sea ice formation in this marginal sea occurred along its northwestern margin as a result of strong winter cooling by the East Asian winter monsoon (EAWM) wind (Talley et al., 2003), we expected the intensity of the IRD events to reflect the strength of the EAWM. At Site U1423, we hoped to reconstruct the EAWM intensity through examination of IRD abundance and distribution along the northern latitudinal transect in the marginal sea. Because stronger EAWM wind produces deep water, called Japan Sea

doi:10.2204/iodp.proc.346.104.2015

Proper Water (JSPW), through sea ice formation in the northwestern part of the sea (Talley et al., 2003), sea ice formation and deepwater ventilation could also reflect EAWM intensity.

Because of the relatively shallow water depth of Site U1423, calcareous microfossils were expected to be better preserved than at the other sites in the Japan Basin. Planktonic microfossils may allow us to study the nature and strength of the influx of the TWC through the Tsushima Strait and/or the intensity of winter cooling, whereas study of benthic microfossils may allow us to discern the nature of the deep water (e.g., oxygenation, saturation level with respect to $CaCO_3$, temperature, and salinity). Examination of the relation between surface water and deepwater characteristics may allow us to explore the linkage between the nature of the TWC and deepwater ventilation. Furthermore, comparison of $CaCO_3$ burial flux and its temporal changes at this site to those at IODP Site U1422 will allow us to reconstruct behavior of the calcium carbonate compensation depth.

Site U1423 is also appropriate for reconstruction of eolian dust flux, sediment grain size, and provenance changes since 5 Ma, considering the relatively low expected LSR. Although only a slight contribution of IRD to the total terrigenous flux may be expected, the specific grain size range (4–32 µm) may be used to differentiate the eolian dust component from other terrigenous components, including IRD.

Operations

Three holes were drilled at Site U1423 (proposed Site JB-2) (Table **T1;** see also Fig. **F2** in the "Expedition 346 summary" chapter [Tada et al., 2015a]). Hole U1423A was cored using the advanced piston corer (APC) to 206.6 m core depth below seafloor (CSF-A) (see the **"Methods"** chapter [Tada et al., 2015b]). Similarly, Hole U1423B was cored with the APC to 249.1 m CSF-A. Hole U1423C was drilled without coring to 114 m CSF-A. From this depth to 180 m CSF-A, we cut and recovered six cores in a series of alternating drilled and cored intervals with the objective of filling gaps in APC cores recovered from the previous two holes. Real-time stratigraphic correlation indicated that the carefully orchestrated coring operation appeared to be successful. Downhole measurements were carried out in Hole U1423B using a modified version of the triple combination (triple combo) tool string (paleo combo) and the Formation MicroScanner (FMS)-sonic tool string. A total of 56 cores were required to obtain 502.6 m of sediment (105.2% recovery).

Transit from Site U1422

The transit to Site U1423 was very short, and the 125 nmi distance was covered uneventfully in 12 h at an average speed of 10.4 kt. The sea passage ended at 2342 h on 21 August 2013. The vessel was maneuvered over the location coordinates, control of the vessel was turned over to dynamic positioning at 0030 h on 22 August, and a seafloor positioning beacon was deployed at 0215 h the same day.

Hole U1423A

Operations in Hole U1423 started on 22 August 2013. The same three-stand APC/extended core barrel (XCB) bottom-hole assembly used at the previous site was deployed, and the drill string was lowered to 1774 meters below rig floor (mbrf). After picking up the top drive and spacing out the drill string, an APC core barrel was deployed at 0530 h on 22 August. The bit was positioned at 1784.4 mbrf for the mudline core; however, the driller was unable to pressure up the drill string. Suspecting that the shear pins had prematurely failed during deployment, the barrel was recovered to the rig floor, where it was discovered empty and with all shear pins sheared. The pins were replaced, and the bit was lowered 10 m to 1794.4 mbrf for a second attempt. Hole U1423A started at 0640 h on 22 August. Core 346-U1423A-1H was recovered with 7.26 m of core, establishing a seafloor depth of 1796.6 mbrf. Cores 1H through 22H were taken from 0 to 206.6 m CSF-A and recovered 212.9 m of core (103%). Four temperature measurements were taken using the advanced piston corer temperature tool (APCT-3) temperature shoe on Cores 4H, 7H, 10H, and 13H (35.8, 64.3, 92.8, and 121.3 m CSF-A, respectively). With the top drive left in place, the drill string was pulled clear of the seafloor at 2355 h on 22 August, ending Hole U1423A.

Hole U1423B

The ship was offset 15 m north of Hole U1423A and the bit was positioned at 1791.4 mbrf. Hole U1423B was spudded at 0050 h on 23 August 2013. Core 346-U1423B-1H was recovered with 4 m of core, establishing a seafloor depth of 1797 mbrf. Cores 1H through 28H extended to 249 m CSF-A and recovered 250 m of core (100%). The recovery amount was negatively impacted because of zero recovery for Core 18H (151.6–158.1 m CSF-A), the result of a space-out error on the rig floor, resulting in an inadvertent drilling of hole that was to be cored on the next core. APC overpull (using full-length core barrels) varied between 60,000 and 80,000 lb between 142 and 249 m CSF-A (Cores 17H through 28H),

with the exception of Core 27H (230.1–239.6 mbrf), when overpull reached 100,000 lb. The last core on deck was recovered at 1530 h.

To prepare for downhole logging, the hole was circulated clean, the logging tools were moved forward to the rig floor, the top drive was set back, and the drill string was pulled to a logging depth of 80.0 meters below seafloor (mbsf). The paleo combo tool string was deployed and recorded spectral gamma ray, caliper, magnetic susceptibility, resistivity, and lithologic density logs. The second string consisted of the FMS-sonic tool string, which recorded resistivity images of the borehole, sonic velocity, caliper, and natural gamma radiation (NGR) data over the entire interval. Both logging tool strings were able to reach total hole depth. The logging tools were then rigged down, and the drill string was pulled clear of the seafloor at 0515 h on 24 August. This marked the end of Hole U1423B.

Hole U1423C

The ship was offset 15 m south of Hole U1423A, and Hole U1423C was spudded at 0655 h on 24 August 2013. The operations plan for this hole was altered to save time and allow for recovering a few gaps in the stratigraphic record remaining after coring Holes U1423A and U1423B. The hole was drilled without coring (using an XCB center bit) to 114 m CSF-A. At that depth, APC coring commenced, recovering six cores interspersed with appropriate drilled intervals to properly space out the core breaks and cover the areas of interest. Hole U1423C was terminated at 180.5 m CSF-A. After setting back the top drive, the bit cleared the seafloor at 1700 h and was back on the rig floor at 2040 h. The positioning beacon was recovered aboard at 1756 h while tripping the drill string. After breaking out the bit and nonmagnetic drill collar, the rig floor was secured for transit, thrusters/hydrophones were raised, and the sea passage to IODP Site U1424 began at 2136 h.

Lithostratigraphy

Drilling at Site U1423 penetrated to a maximum subbottom depth of 249.1 m in Hole U1423B, recovering a total of 250 m of sediment for a recovery rate of 100%. The shipboard lithostratigraphic program involved detailed visual assessment of sediment composition, color, sedimentary structures, and bioturbation intensity, supplemented by petrographic analysis of smear slides and bulk mineralogic analysis by X-ray diffraction (XRD). These were used to describe and define facies and facies associations in each hole. A total of 61 smear slides from Hole U1423A, 66 smear slides from Hole U1423B, and 12 smear slides from Hole U1423C were made and examined to help determine lithologic names. A total of 25 samples were selected for XRD analysis. The major characteristics of the sedimentary sequence at Site U1423 are summarized in Figures **F2, F3,** and **F4,** and the stratigraphic correlation between the three holes is shown in Figure **F5.**

The sedimentary succession recovered at Site U1423 extends from the Pliocene to Holocene and is dominated by clay, silty clay, and diatom ooze with discrete foraminifer-bearing clay levels. Volcaniclastic material represents a minor component throughout the sediment succession, except in tephra layers where it is the dominant component.

The section is divided into two major lithologic units (I and II), distinguished on the basis of sediment composition, referring particularly to the biosiliceous fraction content. Unit I is further divided into two subunits based on the occurrence of alternating dark and light color variations and the intensity of bioturbation. The character of the sediment physical properties, including NGR, magnetic susceptibility, color reflectance parameters, and density, records the distribution of the various sediment components and lithologies (see **"Physical properties"**).

Unit I

Intervals: 346-U1423A-1H-1, 0 cm, to 12H-1, 105 cm; 346-U1423B-1H-1, 0 cm, to 12H-3, 140 cm
Depths: Hole U1423A = 0–103.35 m CSF-A; Hole U1423B = 0–103.50 m CSF-A
Age: Holocene to early Pleistocene (2.2 Ma)

Lithologies and structures

Unit I consists of Holocene to early Pleistocene silty clay and clay with lesser amounts of diatom-bearing and diatom-rich silty clay, as well as rare calcareous layers containing abundant foraminifers. Discrete tephra (volcanic ash) layers ranging in thickness from a few millimeters to >10 cm are numerous. The total thickness of tephra layers in each core (Fig. **F6;** Table **T2**) reaches a broad maximum in lower Subunit IA but with high thickness totals also recorded in discrete intervals of Subunits IIA and IIB. Pyrite can be found as a minor component in most lithologies, whereas fine-grained tephra occurs as a dispersed component throughout much of the section based on smear slide analysis. Unit I is characterized primarily as representing fine-grained material derived from terrigenous sources.

Color banding suggested to be related to variable content of organic matter and pyrite are the most diagnostic features of Unit I, with dark, organic-rich intervals (dark gray to dark olive-gray) interspersed

between lighter colored, organic-poor intervals (light green to light greenish gray). The relative frequency of these color alternations as well as the intensity of bioturbation are the criteria used for recognizing and distinguishing between Subunits IA and IB.

Bulk mineralogy

The results of XRD analysis are listed in Table T3. In general, Pliocene–Pleistocene sediment at this site is composed mainly of quartz, plagioclase, and clay minerals (including smectite, illite, and kaolinite and/or chlorite), as well as biogenic opal-A and minor amounts of halite and pyrite. Calcite (mostly foraminifers and nannofossils) is present in the upper 46 m of Unit I, reaching a maximum at 36.71 m CSF-A in Hole U1423A.

Figure F7 shows the downhole variations in peak intensity of the identified minerals at Site U1423. In general, the contents of quartz, plagioclase, smectite, illite, and kaolinite and/or chlorite show a long-term trend toward increasing counts toward the top of the sequence. In general, the peak heights of these minerals are higher within Unit I and typically lower in Unit II. In contrast, K-feldspar generally increases uphole throughout Unit II and Subunit IB but then fluctuates markedly in Subunit IA sediment, with several pronounced minima where K-feldspar contents drop to near zero. Peaks of opal-A are generally much lower in Unit I and higher in Unit II. The peak intensity of pyrite at 2.5 m CSF-A in Hole U1423A is very high. Halite, presumably precipitated from pore water, is present in all samples with higher intensities in Unit II and lower intensities in Unit I.

Subunit IA

Intervals: 346-U1423A-1H-1, 0 cm, to 9H-6, 135 cm; 346-U1423B-1H-1, 0 cm, to 10H-2, 136 cm
Depths: Hole U1423A = 0–82.65 m CSF-A; Hole U1423B = 0–82.92 m CSF-A
Age: Holocene to early Pleistocene (1.8 Ma)

Lithology and structures

Subunit IA is primarily recognized by having a much higher frequency of dark layers (Fig. F8). It is also characterized by low L*, a*, and b* values in color reflectance and high NGR values with significant fluctuations. Subunit IA is composed mainly of silty clay and clay with subordinate amounts of diatomaceous clay and foraminifer-bearing silty clay. Bioturbation is moderate to intense throughout this subunit and is most noticeably observed at the interface between lighter colored intervals and darker colored beds. Two types of dark intervals can be recognized based on the color shade. Somewhat lighter brown layers are affected by slight bioturbation at various levels, which possibly hides any original lamination. Dark brown layers, on the other hand, typically show fine parallel lamination, frequently highlighted by the presence of biogenic carbonate (mostly planktonic foraminifers), which is light in color and visible to the naked eye. The lower contact of the darker brown layers is typically sharp, whereas the upper contact often appears to be gradual at the transition to the light gray-greenish bed. In some cases, the opposite pattern is observed where the top contact of a dark brown layer is sharp and the dark color fades gradually downhole (see Fig. F8, Section 346-U1423B-5H-3 for examples).

Among the dark colored layers, a very dark greenish brown bed is observed in interval 346-U1423B-5H-6, 30–123 cm. It appears to be different compared to other dark colored beds because of its considerable thickness (~100 cm) and very dark color. This interval is finely laminated with marked color banding (very dark gray and lighter gray alternation) visible in its upper portion. A peculiar characteristic of the very dark greenish interval at 346-U1423B-5H-6, 30–123 cm, is that it contains abundant small pyrite framboids (see "Composition") distributed throughout the layer, which is otherwise composed of terrigenous components and clay minerals. Diatoms and sponge spicules are abundant in this layer, but no biogenic carbonate is found.

Tephra layers are a minor but common component in Subunit IA. An especially prominent tephra layer is found in interval 346-U1423B-8H-4, 50–60 cm. This 10 cm thick tephra is fine grained and white in color and consists of silt-sized volcanic glass and crystals. The volcanic glass contains semiregular shapes with sharp borders on the fragments mixed with rectangular, subparallel pipe vesicles. The volcanic material does not show any trace of postdepositional alteration.

Composition

The principal lithologic components in Subunit IA are terrigenous, volcanic, and biogenic in origin (see Site U1423 smear slides in "Core descriptions"). Diatoms dominate the biogenic fraction, with a minor component of calcareous microfossils, mostly foraminifers and nannofossils (Fig. F9).

Terrigenous components in this subunit are dominated by clay and fine silty clay fractions. Volcanic glass and pumice account for nearly 100% of the tephra layers.

In the upper part of Subunit IA, the light greenish gray intervals are mostly composed of siliciclastic fine-grained material (up to 80%) dominated by clay minerals. A very low biogenic component is ob-

served. Conversely, the dark brown laminated beds are relatively rich in biosiliceous microfossils and biogenic carbonates. Planktonic foraminifers are observed, but the biogenic carbonate fraction is estimated to be no greater than 20%.

Subunit IB

Intervals: 346-U1423A-9H-6, 135 cm, to 12H-1, 105 cm; 346-U1423B-10H-2, 136 cm, to 12H-3, 140 cm

Depths: Hole U1423A = 82.65–103.35 m CSF-A; Hole U1423B = 89.92–103.50 m CSF-A

Age: early Pleistocene (1.8–2.2 Ma)

Lithology and structures

Subunit IB sediment is dominated by silty clay that contains variable amounts of biosiliceous material (mostly diatoms and siliceous sponge debris). The frequency of the dark and light color alternation is considerably less pronounced than in Subunit IA (Fig. **F10**). Bioturbation increases gradually with depth, and sediment mottling and disruption of laminae and color banding is more prevalent. A subtle decrease in NGR values in Subunit IB sediment suggests decreasing amounts of organic matter and/or clay mineral content relative to Subunit IA.

Composition

The principal lithologic components in Subunit IB are terrigenous, volcanic, and biogenic materials (see Site U1423 smear slides in **"Core descriptions"**). The major difference between lithologies of Subunits IA and IB is the less frequent occurrence of calcareous microfossils and slightly greater contents of the biosiliceous component (mostly diatoms and sponge spicules) in Subunit IB than in Subunit IA. In Subunit IB, terrigenous materials are the major component (>80%) of the sediment, and they are dominated by clay and fine silty clay fractions. The biogenic fraction is generally low (<10%) in Subunit IB and is dominated by diatoms and sponge spicules with fewer calcareous microfossils (mostly rare nannofossils). Volcanic glass usually occurs as a minor dispersed component (~5%) throughout the sections.

Unit II

Intervals: 346-U1423A-12H-1, 105 cm, to 22H-7, 66 cm; 346-U1423B-12H-3, 140 cm, to 28H-CC, 22 cm

Depths: Hole U1423A = 103.35–206.76 m CSF-A; Hole U1423B = 103.50–249.52 m CSF-A

Age: early Pleistocene (2.2 Ma) to Pliocene (<3.9 Ma)

Lithology and structures

Unit II is dominantly composed of moderate to heavily bioturbated diatomaceous silty clay and clay and diatom ooze. Unit II is distinguished from Unit I on the basis of a significant increase in diatom content relative to terrigenous sediment from top to bottom. Color banding is less common in Unit II than in Unit I and nearly disappears in the lowest part of the unit. Sediment of Unit II is moderately to heavily bioturbated and often shows a mottled facies (Figs. **F11, F12**).

In contrast to Site U1422, turbidites are rarely observed in Unit II sediment at this site. Tephra beds are frequently found in Subunit IIB (Table **T2**), but their numbers decrease significantly downhole even if single beds are generally much thicker than in Unit I. Rare but thick tephra deposits strongly contribute to the total thickness peaks of tephra in Unit II (Table **T2;** Fig. **F6**).

Composition

The major lithologies in Unit II are dominated by fine-grained material (see Site U1423 smear slides in **"Core descriptions"**). In Core 346-U1423A-10H and 11H smear slides of Subunit IB, the dominant fine-grained component is clay sized, in which abundant clay minerals and quartz are commonly found. Biosiliceous components are present in these cores but occur in low abundances (5%–10%). Biosilica rapidly becomes more abundant (>70%) in smear slides from Core 12H downhole, and this increase is adopted as the boundary between Unit I and II sediments. Diatoms and siliceous sponge spicules dominate the biosilica fraction in Unit II, whereas radiolarians and silicoflagellates are found only in rare or trace amounts (1%–5%). The above-mentioned siliceous fossil assemblages are observed both in the brownish and greenish colored sediment in the "diatom ooze" category.

Dispersed pyrite is found mostly in brownish intervals, but the total amount of pyrite (framboids and/or irregular masses) and other opaque minerals is not particularly abundant (<5%) except in one dark layer found at Section 346-U1423A-12H-4, 2 cm. Here, pyrite is abundant (~10% of the bulk sediment).

Tephra layers that are several centimeters thick were found in Unit II. The volcaniclastic layer found in interval 346-U1423A-8H-7, 46–48.5 cm, is unusual. It shows normal grading, and the bottom layer (4 mm) yields coarse sand-sized pyroclastic material (interpreted to be ballistic debris from eruptions), which is opaque under transmitted light microscope analyses. Another noteworthy tephra is observed in interval 20H-6, 74–93 cm. This volcanic deposit is coarse

grained (sand size) and contains abundant biotite flakes and bubble-wall shards with cuspate and lunate forms (Fig. F13). In general, tephra beds consist of pristine volcanic glass shards.

Bulk mineralogy

The results of XRD analyses conducted on Hole U1423C sediment are listed in Table T3. In general, the bulk mineral assemblage of Unit II sediment is similar to that of Unit I. The major difference is the higher opal-A peak intensities and the disappearance of the calcite peak in samples of Unit II. Figure F7 indicates a slight downhole decrease in quartz, plagioclase, illite, kaolinite and/or chlorite, and pyrite contents, countered by the significant increase in opal-A and halite.

Subunit IIA

Intervals: 346-U1423A-12H-1, 105 cm, to 14H-1, 0 cm; 346-U1423B-12H-3, 140 cm, to 14H-2, 118 cm

Depths: Hole U1423A = 103.35–121.30 m CSF-A; Hole U1423B = 103.50–120.78 m CSF-A

Age: early Pleistocene to late Pliocene (2.2–3.0 Ma)

Unit II is divided into two subunits (IIA and IIB) with Subunit IIA considered to be somewhat transitional between the silty clay of Unit I and the ubiquitous diatom ooze of Subunit IIB. Subunit IIA consists of diatom-rich clay (Fig. F11), but compared to Subunit IIB, the siliciclastic fraction still remains dominant. NGR values in Subunit IIA gradually decrease with respect to Unit I as the biosiliceous component rises but the values remain highly variable (Fig. F14).

Subunit IIB

Intervals: 346-U1423A-14H-1, 0 cm, to 22H-7, 66 cm; 346-U1423-14H-2, 118 cm, to 28H-CC, 22 cm

Depths: Hole U1423A = 121.30–206.76 m CSF-A; Hole U1423B = 120.78–249.52 m CSF-A

Age: late Pliocene (>3.0 Ma)

Subunit IIB is composed of diatom ooze and clayey diatom ooze (Fig. F12). The abundance of diatoms and other siliceous components is uniformly high throughout Subunit IIB (90% and above) and is recorded by reduced variability and a significant decrease in NGR values. The siliciclastic fraction is a minor component and usually includes abundant clay minerals and rare quartz fragments. It may be mixed with vitric tephra and sparse pyrite. Bioturbation is moderate to intense, and distinctive mottling is displayed in some sections.

Discussion

Overall, the sedimentary succession at Site U1423 records a history of terrigenous and biosiliceous deposition since the Pliocene. Unit II sediment, which is late Pliocene to early Pleistocene in age, is characterized by dominantly diatom rich strata, as compared to Unit I, possibly corresponding to a period of elevated biological productivity and good overall circulation in the basin. In contrast to the counterpart Unit II sediment at Site U1422, no turbidites were identified at this site. This lack of turbidite deposits at Site U1423 has allowed further division of Unit II sediment into Subunits IIA and IIB, which extends beyond the original lithostratigraphy described at nearby ODP Site 794 (Tamaki, Pisciotto, Allan, et al., 1990; Tada and Iijima, 1992; Tamaki et al., 1992; Tada, 1994). Tada and Iijima (1992) and Tada (1994) later refined and completed the lithostratigraphy of sedimentary units recognized at Site 794, but nonetheless retained only a single, undifferentiated Unit II.

Visually, there is no clear characteristic allowing straightforward division of Unit II into Subunits IIA and IIB, but the decrease in NGR values at the transition between Units I and II and the further decline at the top of Subunit IIB appear to be significant. This decrease is mainly due to a drop in uranium content and thus probably reflects the overall decrease in organic matter content (Fig. F14) in Unit II (see "Geochemistry"). However, the decrease in organic matter is itself accompanied by a concomitant increase in diatom content, which suggests that the low NGR values in Unit II are driven by dilution from the high input and accumulation of biogenic opal. The siliceous biogenic component remains relatively low in the transitional Subunit IIA except for a very few horizons, whereas Subunit IIB mainly comprises of diatom ooze.

The occurrence of authigenic pyrite is frequent throughout the sediment succession and is found most abundantly in the brownish and dark brown layers in both Units I and II. The size and distribution of this mineral is of great interest for determining the transition from oxic to suboxic/euxinic conditions in the basin, as well as the water column stratification. Pyrite is ubiquitous in modern anoxic sediment and preserved in many ancient sediment rocks. Small (<10 µm) scattered framboids can be considered a reliable marker of low oxygen conditions within the water column (Wilkin et al., 1996, 1997; Wilkin and Arthur, 2001), as previously observed in dark layers deposited during the last glacial in the marginal sea (Masuzawa and Kitano, 1984). On the other hand, the diagenetic pyrite is com-

monly found in discrete layers (few millimeters thick) and is composed of larger (~100 µm), sometimes euhedral, crystals.

More than 100 visible tephra beds were observed in cores from Hole U1423A (Table T2). The thickest tephra layer (maximum thickness = 17 cm) occurs in Subunit IIB, although most of the layers were <1 cm thick. The total thickness of tephra layers in each core shows a peak in the transition from the lower part of Subunit IA to Subunit IB (Fig. F6). Tephra occurrence decreased remarkably in Unit II, although a few thick tephra deposits strongly contribute to the total thickness peaks in Unit II. Some especially distinctive tephra beds were observed. One is a thick white tephra found at 45.41–45.57 m CSF-A in Hole U1423A (interval 346-U1423A-6H-1, 11–27 cm). This tephra contains abundant thin bubble-wall type volcanic glass shards. The distinctive glass morphology suggests that this layer may be correlative to the Hakkoda-Daiichi (Hkd-1 or Hkd-Ku) tephra erupted from Hakkoda Volcano in northern Honshu, Japan. This tephra occurs just above the Brunhes/Matuyama paleomagnetic boundary (Machida and Arai, 2003). Another characteristic tephra was found at 186.37–186.54 m CSF-A in Hole U1423A (interval 20H-6, 77–94 cm). This tephra is dominated by "bubble-junction" type glass shards with biotite as the dominant heavy mineral. These features are the same as in the Znp-Ohta tephra that occurs in central Honshu, Japan (Satoguchi and Nagahashi, 2012). Another characteristic tephra was observed at 69.29–69.395 m CSF-A in Hole U1423A (interval 8H-4, 49–59.5 cm). This tephra consists of thick bubble-wall glass shards and biotite, as well as clinopyroxene and orthopyroxene as heavy minerals. One possible match for this tephra is the OM-SK110 tephra, which occurs in the Pliocene sequence above the Olduvai event in central Japan (Satoguchi and Nagahashi, 2012). These initial correlations will be further examined by shore-based research.

Biostratigraphy

At Site U1423, a ~250 m thick succession of Pliocene to Holocene sediment was recovered. Calcareous nannofossils are generally rare and sporadically distributed in the upper 80 m. Planktonic foraminifers are rare to absent with moderate to poor preservation throughout most of the succession but are abundant in the upper part of the succession above 74.19 m CSF-A. However, the regional zonal scheme only has limited application, as few planktonic foraminiferal datums were identified. Radiolarians are generally common to abundant with rare occurrences at 83.6 m CSF-A. The radiolarian biostratigraphic zonation ranges from the *Larcopyle pylomaticus* Zone (Pliocene) to the *Botryostrobus aquilonaris* Zone (Late Pleistocene). The diatoms are well preserved with abundances ranging from 2%–5% to >60%. Diatom mats and oozes are found in the Pliocene samples. The diatom stratigraphy spans the interval from Zone NPD 7 (Pliocene) to NPD 12 (Late Pleistocene). The nannofossil, radiolarian, and diatom datums and zonal schemes generally agree, with only minor inconsistencies. The integrated calcareous and siliceous microfossil biozonation is shown in Figure F15, and microfossil datums are shown in Table T4. A preliminary age-depth plot including biostratigraphic datums is shown in Figure F16. See **"Stratigraphic correlation and sedimentation rates"** for a discussion on sedimentation rates at Site U1423. Benthic foraminifers occur intermittently throughout the succession, exhibiting marked changes in abundance, preservation, and species distribution. The overall assemblage composition indicates bathyal paleodepths. However, the assemblage composition also reflects substantial variations in organic export flux to the seafloor and deepwater oxygenation.

Calcareous nannofossils

Calcareous nannofossil biostratigraphy is based on the analysis of core catcher and split-core section samples from Holes U1423A–U1423C. Thirty of 76 samples studied at Site U1423 contain nannofossils (Table T5).

Nannofossils are present in Pleistocene sediment from 26.8 to 76.06 m CSF-A in Hole U1423A (Samples 346-U1423A-4H-1, 50–51 cm, to 9H-2, 75–76 cm) and from 28.10 to 77.36 m CSF-A in Hole U1423B (Samples 346-U1423B-4H-4, 53–54 cm, to 9H-5, 75–76 cm). Nannofossils are absent in Hole U1423A between 83.60 and 207.02 m CSF-A (Samples 346-U1423A-9H-CC to 22H-CC), with the exception of a short interval from 142.78 to 150.24 m CSF-A (Samples 16H-2, 98–99 cm, to 16H-CC), where rare to abundant nannofossils are observed (Fig. F17). These samples have been disturbed by drilling operations (see **"Lithostratigraphy"**) and thus represent assemblages that are not in situ. Samples from Hole U1423B were barren below 82.87 m CSF-A (Sample 346-U1423B-10H-2, 130–131 cm) with the exception of a short interval containing rare nannofossils between 136.45 and 151.91 m CSF-A (Samples 16H-3, 85–86 cm, to 17H-CC). All samples from Hole U1423C are devoid of calcareous nannofossils.

Nannofossil diversity at Site U1423 is low, although it is higher than at previous Site U1422. The nannofossil assemblage consists of relatively few taxa including *Braarudosphaera bigelowii, Calcidiscus lepto-*

porus, Calcidiscus macintyrei, Coccolithus pelagicus, Emiliania huxleyi, Gephyrocapsa caribbeanica, Gephyrocapsa muellerae, Gephyrocapsa oceanica, Gephyrocapsa spp. (>4 µm), *Gephyrocapsa* spp. (<4 µm), *Helicosphaera carteri, Helicosphaera* spp., *Pontosphaera japonica, Pontosphaera multipora, Pontosphaera* spp., *Pseudoemiliania lacunosa, Reticulofenestra minuta, Reticulofenestra minutula, Reticulofenestra* spp., and *Syracosphaera* spp. *Helicosphaera sellii* is present in the disturbed interval (Sample 346-U1423A-16H-2, 98–99 cm; 142.79 m CSF-A), and *Cyclicargolithus floridanus* is documented as a reworked species in Samples 6H-2, 94–95 cm, and 6H-CC. Preservation is generally poor to moderate with sporadic occurrences of good preservation in samples with high nannofossil abundances (e.g., Sample 4H-4, 92–93 cm; 31.68 m CSF-A), composed almost entirely of small *Gephyrocapsa* (<4 µm).

Two nannofossil zones are recognized (Fig. F15). Nannofossil Zones CN15/NN21 are recognized based on the first occurrence (FO) of *E. huxleyi* (Sample 346-U1423B-2H-4, 69–70 cm; 9.29 m CSF-A), and the bases of nannofossil Zones CN14b/NN20 are recognized based on the last occurrence (LO) of *P. lacunosa* (Sample 346-U1423A-5H-1, 113–114 cm; 36.93 m CSF-A).

Radiolarians

A total of 29 core catcher samples from Holes U1423A (Samples 346-U1423A-1H-CC to 22H-CC) and U1423B (Samples 346-U1423B-22H-CC to 28H-CC) were prepared for radiolarian analysis (Table T6). Radiolarians are generally common to abundant in the entire succession (Fig. F17), although they are rare at 83.6 m CSF-A (Sample 346-U1423A-9H-CC).

Nine radiolarian datums were found in Hole U1423A (Table T4). Late Pleistocene datums, the LOs of *Lychnocanoma sakaii* (0.05 Ma), *Amphimelissa setosa* (0.08 Ma), and *Spongodiscus* sp. (0.29 Ma), are observed at 7.2 m CSF-A (Sample 346-U1423A-1H-CC), 17.0 m CSF-A (Sample 2H-CC), and 26.6 m CSF-A (Sample 3H-CC), respectively. The LO of *Axoprunum acquilonium* (2.2 Ma) is at 93.2 m CSF-A (Sample 10H-CC) just below the sparse interval at 83.6 m CSF-A (Sample 9H-CC). The Pleistocene/Pliocene boundary is close to the FO of *Cycladophora davisiana* (2.7 Ma) at 112.1 m CSF-A (Sample 12H-CC) and the LO of *Hexacontium parviakitaensis* (2.7 Ma) at 131.2 m CSF-A (Sample 14H-CC). The FO of *H. parviakitaensis* (3.9/4.3 Ma) was found at 168.9 m CSF-A (Sample 18H-CC). Deeper than 178.3 m CSF-A (Sample 19H-CC), the *Siphocampe arachnea* group shows an acme zone (4.46–4.71 Ma). The FO and LO of *Dictyophimus bullatus* are primary datums that define the top and base of the *Dictyophimus bullatus* Zone. Although this species is very rare, the LO and FO datums are recognizable at 187.7 m CSF-A (Sample 20H-CC) and 197.2 m CSF-A (Sample 21H-CC). The abundant occurrence of the *S. arachnea* group in the absence of *D. bullatus* at the base of Hole U1423A (207.0 m CSF-A; Sample 22H-CC) suggests an age between 4.4 and 4.71 Ma.

In the lower part of Hole U1423B, two radiolarian datums, the LO of *D. bullatus* (4.4 Ma) and a rapid increase (RI) of the *S. arachnea* group (4.71 Ma), are at 192.3 m CSF-A (Sample 346-U1423B-22H-CC) and 220.8 m CSF-A (Sample 25H-CC), respectively (Table T4). The base of Hole U1423B (249.5 m CSF-A; Sample 28H-CC) is deeper than the RI of the *S. arachnea* group (4.71 Ma) and shallower than the LO of *Larcopyle pylomaticus*, suggesting an age younger than 5.3 Ma.

Diatoms

Diatom biostratigraphy was based on smear slides from core catcher samples. Twenty-two core catcher samples were examined from Hole U1423A (Samples 346-U1423A-1H-CC to 22H-CC), and five NPD datums were identified (Tables T4, T7):

- The LO of *Proboscia curvirostris* (older than 0.3 Ma) marks the base of NPD 12 (Sample 4H-CC).
- The LO of *Actinocyclus oculatus* (older than 1.0 Ma) marks the base of NPD 11 (Sample 6H-CC).
- The LO of *Neodenticula koizumii* (older than 2.0 Ma) marks the base of NPD 10 (Sample 8H-CC).
- The LO of *Neodenticula kamtschatica* (older than 2.6–2.7 Ma) marks the base of NPD 9 (Sample 9H-CC).
- The FO of *N. koizumii* (younger than 3.4–3.9 Ma) marks the base of NPD 8 (Sample 14H-CC).

Sample 22H-CC, which is younger than 5.6 Ma, is the deepest sample from Hole U1423A (LO of *Shionodiscus oestrupii*).

Ten core catcher samples were collected from Hole U1423B (Samples 346-U1423B-15H-CC to 17H-CC and 22H-CC to 28H-CC), and two datums were identified (Tables T4, T7). The samples from Hole U1423B were collected to complement the observations from Hole U1423A because the base of Hole U1423B was deeper than in Hole U1423A. Therefore, the ages in samples from Hole U1423B define the following NPD zones: the FO of *Neodenticula koizumii* (younger than 3.4–3.9 Ma) marks the base of NPD 8 (Sample 16H-CC), and Sample 28H-CC (NPD 7) is younger than 4.81 Ma based on the LO of *Thalassiosira jacksonii*.

Overall, diatom abundance ranged from 2%–5% to >60% in the observed smear slides (Fig. F17). Preservation was good in all samples, and there were no

signs of dissolution. Diatom valve fragmentation was normal. In addition, the ratio between preserved >50 µm centrics and <20 µm pennates was constant. Diatom range abundance is shown in Table T7.

Diatom samples with abundance >60% were identified in Samples 346-U1423A-8H-CC to 14H-CC, and diatom mats were identified in Samples 346-U1423A-7H-CC, 13H-CC, 15H-CC, 20H-CC, and 21H-CC and 346-U1423B-23H-CC (Fig. F17). The comparison of these samples with qualitative abundances of *Chaetoceros* spores, an upwelling indicator, suggests different high-productivity systems: one dominated by *Chaetoceros* spores that is analogous to modern upwelling systems and a different one that produces diatom mats and oozes with lower *Chaetoceros* spore abundances.

Freshwater diatom species were absent in all samples except for rare occurrences in Samples 346-U1423A-5H-CC and 6H-CC (Table T7).

Planktonic foraminifers

Planktonic foraminifers were examined in core catcher samples from Holes U1423A (22 samples), U1423B (10 samples), and U1423C (6 samples) and in toothpick samples from Hole U1423A (8 samples) and U1423B (15 samples) taken after the core sections were split. Planktonic foraminifers are mainly confined to the upper part of the succession (shallower than Sample 346-U1423A-8H-CC; 74.19 m CSF-A) (Fig. F18). Of the 23 toothpick samples examined from dark layers (Table T8), 14 samples contained >80 specimens, 1 sample contained 22 specimens, and 2 samples had <5 specimens.

Taxon relative abundances and estimates of assemblage preservation are presented in Table T8. Planktonic foraminifers are abundant shallower than Sample 346-U1423A-6H-CC (54.96 m CSF-A) and are absent or rare in the interval deeper than Sample 7H-CC (64.64 m CSF-A), except in Samples 346-U1423A-16H-CC (150.20–150.24 m CSF-A), 346-U1423B-15H-CC (132.80–132.85 m CSF-A), and 346-U1423C-4H-CC (142.65–142.70 m CSF-A), where high abundance peaks occur. Preservation is moderate to good in most core catcher samples, and fragmentation and/or pyritization are common.

Site U1423 planktonic foraminiferal assemblages above Sample 346-U1423A-8H-CC (74.19 m CSF-A) are characteristic of cold, midlatitude, restricted environments, consisting mainly of *Globigerina bulloides* and *Neogloboquadrina pachyderma* (sinistral) with rare occurrences of *Globigerina umbilicata, Globigerina quinqueloba, Neogloboquadrina pachyderma* (dextral), *Neogloboquadrina dutertrei* (= *Neogloboquadrina himiensis*), *Neogloboquadrina incompta, Neogloboquadrina kagaensis* group (*Neogloboquadrina kagaensis* and *Neogloboquadrina inglei*), and *Neogloboquadrina* cf. *asanoi*. In addition to these species, *Globorotalia praeinflata* is common in Samples 346-U1423B-15H-CC (132.80–132.85 m CSF-A) and 346-U1423C-4H-CC (142.65–142.70 m CSF-A). *N. pachyderma* (dextral) is dominant in Sample 346-U1423A-16H-CC (150.20–150.24 m CSF-A), where rare specimens of *Orbulina universa* are also found. The LO of *N. kagaensis* group, reported as 0.7 Ma by Kucera and Kennett (2000), was identified in Sample 346-U1423A-5H-4W, 77–78 cm (41.07–41.08 m CSF-A). The peak in planktonic foraminiferal abundance in Sample 346-U1423A-16H-CC (150.20–150.24 m CSF-A) corresponds to Zone PF6 of Maiya (1978), based on the co-occurrence of *O. universa* and *N. pachyderma* (dextral), indicating that this horizon is older than 3.0 Ma (Miwa, 2014).

Benthic foraminifers

Benthic foraminifers were examined in core catcher samples from Holes U1423A (22 samples), U1423B (10 samples), and U1423C (6 samples) and in toothpick samples from Holes U1423A and U1423B taken after cores were split. Mudline samples recovered in Holes U1423A and U1423B were also investigated. Samples with an average volume of ~30 cm^3 were processed from all core catchers to obtain quantitative estimates of downhole benthic foraminiferal distribution patterns. To assess assemblage composition and variability, all specimens from the >150 µm fraction were picked and transferred to slides prior to identification and counting. The distribution of benthic foraminifers was additionally checked in the 63–150 µm fraction to ensure that assemblages in the >150 µm fraction were representative and that small species such as phytodetritus feeders or small infaunal taxa were not overlooked.

Benthic foraminifers occur intermittently through the ~250 m thick biosiliceous-rich succession recovered at Site U1423 (Fig. F18; Table T9). Abundance and diversity are generally low, except for three samples (Table T9) found to contain at least 100 specimens per 30 cm^3 of sediment and to exhibit much higher diversity. Preservation varies substantially throughout the succession. The assemblages consist of calcareous and agglutinated taxa, and their overall composition indicates bathyal paleodepths throughout the Pleistocene and Pliocene. Prominent variations in the downcore distribution of benthic foraminifers appear to reflect changes in organic export flux to the seafloor and/or in oxygenation at the seafloor (Fig. F18).

A total of 44 benthic foraminiferal taxa were identified. Census counts from core catcher and split-core

section samples are presented in Table T9. Figure F18 summarizes the downcore distribution of the more common benthic foraminiferal taxa in core catcher samples from Holes U1423A–U1423C. Common species include *Bolivina pacifica, Epistominella pulchella, Eggerella bradyi, Globobulimina pacifica, Martinotiella communis*, and *Miliammina echigoensis* (Figs. F19, F20). In Samples 346-U1423A-4H-CC and 5H-CC, the high abundances of *B. pacifica* and *E. pulchella* suggest enhanced surface productivity and higher organic export flux during deposition. *B. pacifica* is an ectobiont-bearing foraminifer, which also displays cytoplasmic adaptations (plasma membrane invaginations) that are thought to promote inhabitation of microxic environments (trace or 0.1 mL/L; sensu Bernhard and Sen Gupta, 1999) (Bernhard et al., 2010). Thus, the dominance of this species in Sample 346-U1423A-5H-CC indicates microxic pore water associated with intense oxygen depletion of bottom water during deposition of this sedimentary interval. Samples 346-U1423A-16H-CC (150.2 m CSF-A), 346-U1423B-15H-CC (132.8 m CSF-A), and 346-U1423C-4H-CC (142.65 m CSF-A) are characterized by a diverse assemblage indicating substantially improved oxygenation at the seafloor at ~3 Ma (Fig. F19). The assemblage includes cosmopolitan taxa such as *Cibicidoides mundulus, Cibicidoides refulgens, Cibicidoides robertsonianus, Globobulimina pacifica, Hoeglundina elegans* (which has an aragonitic test), *Melonis barleanum, Melonis pompilioides, Pullenia quinqueloba, Oridorsalis umbonatus*, and *Pyrgo murrhina*, as well as a few ostracods (see below). These intervals do not appear to be correlative, based on hole-to-hole stratigraphic correlation (see **"Stratigraphic correlation and sedimentation rates"**). They may, however, correspond to several transient episodes of improved deepwater circulation in the marginal sea, although the low resolution of our sample set does not allow resolution of individual events in Holes U1423A–U1423C. Moderately to well-preserved diatoms and radiolarians are common to abundant in residues >150 and >63 µm throughout the succession and become dominant deeper than 100 m CSF-A. Most samples deeper than 100 m CSF-A, except for Samples 346-U1423A-16H-CC (150.2 m CSF-A), 346-U1423B-15H-CC (132.8 m CSF-A), and 346-U1423C-4H-CC (142.65 m CSF-A), are either barren or impoverished, mainly containing rare agglutinated species.

Ostracods

Core catcher samples were also examined for the presence of ostracods during shipboard preparation of benthic foraminifer samples. Ostracods are absent from all but Sample 346-U1423A-16H-CC (150.2 m CSF-A), where three valves and one carapace belonging to *Krithe* spp., one carapace of *Henryhowella* cf. *H. circumdentata* (Brady, 1880), and one valve of *Legitimocythere* sp. were found. Preservation of the shells ranges from moderate to very good (Fig. F21). This same assemblage was found previously at Site 435 in the Japan Trench during Deep Sea Drilling Project Leg 56 (Hanai et al., 1980). All three taxa are common in bathyal environments.

Mudline samples

Mudline samples from Holes U1423A and U1423B were gently washed in order to preserve fragile agglutinated specimens with extremely low fossilization potential. The mudline sample from Hole U1423A contains only organically cemented agglutinated foraminifers, including *Cribrostomoides subglobosus, Haplophragmoides sphaeriloculum, Hyperammina elongata, Jaculella* cf. *acuta, Miliammina echigoensis, Paratrochammina challengeri*, and *Rhabdammina* sp. (Fig. F20). These organically cemented tests are extremely delicate and fragile (except for *M. echigoensis*) and thus have virtually no fossilization potential. Only two specimens of *M. echigoensis* were stained with rose bengal. These specimens exhibit much better preservation than unstained specimens. Diatoms are dominant, and planktonic foraminifers are absent in the mudline sample, suggesting that planktonic calcareous tests may be dissolved and that unfavorable conditions prevent calcareous benthic foraminifers from inhabiting the upper few centimeters of the sediment.

Geochemistry

Site U1423 was the second of three sites drilled in the Japan Basin. Similar to Sites U1422 and U1424, the primary goal behind drilling was to generate high-resolution paleoceanographic records, especially including the history of eolian dust and IRD. However, the water depth (1785 m) and landward proximity of Site U1423 contrasts with those at the other two sites. Furthermore, the location of Site U1423 had not been previously drilled. In short, the sedimentary record and geochemical profiles were expected to be somewhat different from those at Sites U1422 and U1424, but we had limited information before operations.

The main focus of the geochemistry program at Site U1423, other than meeting minimum requirements, was to generate profiles of solids, gases, and interstitial waters that could constrain fluxes of reactants and products resulting from microbial decomposition of organic matter. With this goal, comparisons to profiles at Sites U1422 and U1424 might provide insight to interactions between the "deep biosphere" and overlying waters of the sea. We endeavored to

construct a set of detailed records, although this was difficult given the limited time during operations at the site (~2.9 days) and the transit (~6 h) to the next site (U1424). In particular, while drilling at Site U1423 cores arrived on deck every 25–45 min, which left minimal time for analyses.

Sample summary

The geochemistry group collected and analyzed a range of samples. These included the following (Tables T10, T11, T12):

- 1 mudline (ML) water sample from inside the core liner above sediment of Core 346-U1423A-1H. We collected 50 mL.
- 50 interstitial water samples from whole-round squeezing (IW-Sq) from Hole U1423A (44 samples) and the lower cores of Hole U1423B (6 samples) at nominal 4.5 m spacing. For most samples, we collected between 35 and 45 mL of interstitial water.
- 0 interstitial water samples from Rhizons.
- 41 sediment samples from the interstitial water squeeze cakes of Holes U1423A (35 samples) and U1423B (6 samples). All interstitial water squeeze cake samples from lithologic Unit I were analyzed, whereas alternate interstitial water squeeze cake samples from lithologic Unit II were analyzed.
- 50 headspace (HS) gas samples. All of these samples were "paired" with the IW-Sq samples.
- No gas samples on voids (Vacutainer) were taken because no large gas voids occurred during core recovery at Site U1423.

Carbonate and organic carbon

Sediment recovered at Site U1423 had only minor amounts of $CaCO_3$ (~0.4 wt%) (Fig. F22). In general, $CaCO_3$ contents decrease from ~1 wt% at 1.4 m CSF-A to 0.2 wt% at 18 m CSF-A and remain relatively low further downcore. The exceptions are samples centered around 56.3 and 70.3 m CSF-A, which have slightly elevated $CaCO_3$ (Table T10), and one sample at 41.8 m CSF-A with a $CaCO_3$ content of 14.3 wt%. This sample coincides with a zone rich in foraminifers (see "Biostratigraphy").

Total carbon content of sediment is primarily controlled by the total organic carbon (TOC) content, which has variable and high values in lithologic Subunit IA (Fig. F22). In the uppermost 20 m below seafloor, TOC ranges from 2.1 wt% in the uppermost sample at 1.45 m CSF-A to 0.2 wt% at 8.8 m CSF-A. The variability partly reflects the nature of discrete sampling of shallow sediment in the marginal sea. Sediment sequences in this region, particularly lithologic Subunit IA, have numerous centimeter-scale dark and light layers containing different amounts and compositions of organic matter (Föllmi et al., 1992; Tada et al., 1992). Our samples, which come from intervals squeezed for interstitial water, represent short thicknesses (originally ~5 cm) separated nominally by 4.5 m. In any case, similar TOC variability has been observed in shallow sediment at other drill sites of the Japan Basin (Tamaki, Pisciotto, Allan, et al., 1990). Samples from lithologic Subunit IB, between ~83 and 103 m CSF-A, generally have lower TOC contents than those of lithologic Subunit IA. Interestingly, the highest TOC levels of Subunit IB are found near the base of the unit. Deeper than 103 m CSF-A and within lithologic Unit II, TOC contents are low, averaging 0.54 wt%.

The mean value of total nitrogen (TN) is 0.2 wt%. The maximum TN content (0.3 wt%) is found at ~30 m CSF-A.

Manganese and iron

The dissolved Mn profile (Fig. F23) exhibits a fairly smooth trend with depth. Close to the seafloor, Mn concentration is below detection limit (determined to be 0.5 µM). However, by 1.5 m CSF-A, dissolved Mn concentrations spike to 120 µM (Table T11). Beneath this depth, Mn concentrations decrease. The decrease is concave downward and decreases below detection limit at ~37 m CSF-A. At ~70 m CSF-A, dissolved Mn begins to increase again, reaching ~25 µM at ~175 m CSF-A.

The initial rise in dissolved Mn likely indicates a zone where microbes utilize Mn oxides and hydroxides to consume organic carbon (Froelich et al., 1979; Masuzawa and Kitano, 1983). Although our profile suggests dissolved Mn decreases to zero at the seafloor, the depth of zero dissolved Mn may lie somewhere between the seafloor and the uppermost sample at 1.5 m CSF-A (Masuzawa and Kitano, 1983). Our samples lack sufficient depth resolution to document a possible change in the slope of dissolved Mn concentration at shallow sediment depth. The second and deeper low in dissolved Mn, from ~37 to 70 m CSF-A, suggests a horizon where a mineral removes Mn and then redissolves. This zone corresponds to the alkalinity maximum (Fig. F24). It is possible that dissolved Mn^{2+} released at shallow depth diffuses downhole to a zone of high HCO_3^- concentration to form rhodochrosite ($MnCO_3$). In turn, with burial, the rhodochrosite may recrystallize as a different carbonate mineral, such as siderite, releasing dissolved Mn^{2+} at depth. Such an interpretation is consistent with theory (Middelburg et al., 1987), and previous studies provide evidence for this process in this marginal sea, in particular at ODP Site

799 (Masuzawa and Kitano, 1983; Matsumoto, 1992). However, a thorough study comparing interstitial water and solid phases is required to confirm this interpretation.

The Fe profile at Site U1423 (Fig. F23) exhibits a high degree of variance, which may indicate the complexity of Fe cycling within the sediment, the challenges of measuring Fe, or both. Unlike Mn, Fe can be a major element in multiple authigenic minerals, including sulfides, phosphates, carbonates, and clay (Berner, 1981). Thus, the "bumpy" profile, where variations in dissolved Fe occur over short depth intervals, may reflect intervals where Fe is removed or liberated from different mineral phases. However, Fe also readily precipitates from water when exposed to oxygen. It is possible that when whole-round interstitial water samples are separated and squeezed, exposure to atmospheric oxygen causes precipitation of variable amounts of dissolved Fe. Furthermore, Fe concentrations may be near the detection limit of the instrument, which is quantified to be 0.9 µM for this site.

Smooth interstitial water Fe profiles have been obtained using Rhizon samples at certain locations (e.g., the Arctic Ocean [Backman, Moran, McInroy, Mayer, and the Expedition 302 Scientists, 2006]). Moreover, the Rhizons can be inserted over very short depth increments in the event that dissolved Fe concentrations truly change over a short vertical distance. It would be intriguing to examine Fe concentrations using Rhizons across short depth intervals. No Rhizon sampling was done at this site, however.

Alkalinity, ammonium, and phosphate

The alkalinity, NH_4^+, and PO_4^{3-} profiles at Site U1423 (Fig. F24) are similar to those at Site U1422 (see Fig. F25 in the "Site U1422" chapter [Tada et al., 2015c]) with two notable differences. First, the prominent inflection in alkalinity observed at Site U1422 is not found at Site U1423. Second, through the upper 50 m below the seafloor, concentrations of NH_4^+ and PO_4^{3-} are slightly greater at Site U1423 than at Site U1422.

Alkalinity increases from 2.4 mM at the seafloor to 28 mM at 51 m CSF-A. Below this depth, alkalinity decreases steadily to 15 mM at 244 m CSF-A. The profile is concave downward to 50 m CSF-A and slightly concave downward deeper than 50 m CSF-A. The lack of a shallow alkalinity inflection at Site U1423 suggests that a prominent sulfate–methane transition (SMT) does not exist at this location, although a change in slope can be observed at 27 m CSF-A.

Ammonium increases from 93 µM near the seafloor to 2352 µM at 56 m CSF-A. Below this depth, NH_4^+ drops steadily to ~1776 µM at 244 m CSF-A. The profile is concave downward until 50 m CSF-A but fairly linear below 50 m CSF-A.

Phosphate increases from 1.4 µM at the seafloor to 106 µM at 23 m CSF-A. Below this depth, PO_4^{3-} decreases steadily to <10 µM at 136 m CSF-A. This decrease in PO_4^{3-} has a concave downward profile.

Somewhat similar to Site U1422, the magnitude and overall shape of the profiles relate to microbial diagenesis of organic matter and authigenic mineral precipitation. Organic matter landing on the seafloor has a nominal C:N:P ratio of 106:16:1 (Froelich et al., 1979). During sediment burial, Bacteria and Archaea consume the organic matter through a suite of microbial reactions, which release HCO_3^-, NH_4^+, and PO_4^{3-} to interstitial water. Dissolution of metal oxides also releases dissolved PO_4^{3-} to shallow sediment (Cha et al., 2005). At great depth, HCO_3^- and PO_4^{3-} precipitate into or onto mineral phases (Berner, 1981).

The higher NH_4^+ and PO_4^{3-} concentrations in the upper 50 m at Site U1423 compared to those at Site U1422 suggest greater input of organic carbon from at least the last few million years. However, NH_4^+ and PO_4^{3-} concentrations throughout deeper depths are higher overall at Site U1422 than at Site U1423, indicating a relatively higher organic carbon input at Site U1422 on a longer timescale. One possibility is that at Site U1423, although the products of organic decomposition occur in higher concentrations in Holocene and Late Pleistocene sediment, present lower concentrations than at Site U1422 when integrated over a longer time interval. These differences may be explained by a time of slow sedimentation (see **"Stratigraphic correlation and sedimentation rates"**), when organic inputs accumulated more slowly or when the HCO_3^-, NH_4^+, and PO_4^{3-} products were lost through diffusion or mineral precipitation.

Interestingly, the NH_4^+ concentration gradient at Site U1423 (as well as Site U1422 and other locations; see **"Geochemistry"** in the "Site U1422" chapter [Expedition 356 scientists, 2015c]) implies a modest upward flux of nitrogen from the interstitial water to the bottom water. Given the previous section and discussion about the Mn profile, we wonder whether NH_4^+ concentration decreases to zero at the seafloor

or, alternatively, at some sedimentary horizon below the seafloor.

Volatile hydrocarbons

Methane is the only hydrocarbon gas in all HS samples at Site U1423. No ethane or heavier hydrocarbons were detected.

In general, CH_4 concentrations at Site U1423 (Fig. F25) are much lower than those at Site U1422. Concentrations are nearly zero over the upper 30 m CSF-A. Methane values increase downhole, reaching a peak of 2006 ppmv at 70 m CSF-A. The CH_4 peak is prominent, but recall that saturation values of 10,000 ppmv were regularly measured at Site U1422 (see "Geochemistry" in the "Site U1422" chapter [Tada et al., 2015c]). Below 70 m CSF-A, CH_4 concentrations decrease rapidly to below 10 ppmv at 155 m CSF-A and remain so to the bottom of Hole U1423B.

Degradation of organic matter produces modest amounts of CH_4 between 30 and 130 m CSF-A. Production is probably greatest at ~70 m CSF-A, where peak CH_4 concentration occurs and dissolved alkalinity and NH_4^+ concentrations are highest. Because of the relatively low concentrations, no major gas voids were observed at Site U1423.

A downhole comparison of CH_4 and SO_4^{2-} concentrations (Fig. F26) shows that an SMT occurs at Site U1423. However, this SMT is diffuse, occurring over ~20 m between 30 and 50 m CSF-A.

Sulfate and barium

Profiles of dissolved SO_4^{2-} and dissolved Ba at Site U1423 (Fig. F27) are somewhat similar to those at Site U1422. The major difference is the shape of the SO_4^{2-} profile.

Dissolved SO_4^{2-} concentration in the mudline sample is 28.6 mM, which compares favorably with an inferred 28.5 mM in JSPW (see "Geochemistry" in the "Methods" chapter [Tada et al., 2015b]). From the seafloor to ~50 m CSF-A, values steadily decrease. This decrease in SO_4^{2-} exhibits a concave downward profile, in contrast to the more linear profile at Site U1422 (Fig. F27). Deeper than ~50 m CSF-A, SO_4^{2-} concentrations are consistently <0.7 mM.

Dissolved Ba concentrations are <30 µM until ~27 m CSF-A when values steadily rise. The highest Ba standard included in the inductively coupled plasma–atomic emission spectroscopy (ICP-AES) calibration curve was 364 µM, and this value is exceeded at 41.75 m CSF-A. Ba concentrations of each sample below this depth exceed this highest standard and are thus unconstrained. Therefore, any Ba values greater than 364 uM are untrustworthy and Ba is thus reported here as "preliminary."

In contrast to Site U1422, the upward flux of CH_4 and anaerobic oxidation of methane (AOM) play a minor role at Site U1423. Instead, the dominant net sink of SO_4^{2-} below the seafloor is through microbial decomposition of solid organic carbon. This alternative pathway for sulfate reduction can be expressed in simplified form as follows (Berner, 1980):

$$2CH_2O + SO_4^{2-} \rightarrow HS^- + 2HCO_3^- + H^+.$$

Because this reaction dominates SO_4^{2-} consumption and occurs over a thick depth interval, the SO_4^{2-} profile has significant curvature and the alkalinity profile lacks a prominent kink.

Site U1423 is interesting to studies of Ba cycling in deep-sea sediment. Ba is released into pore water from barite dissolution when SO_4^{2-} concentrations approach zero. As SO_4^{2-} is depleted at depth, methanogenesis becomes the primary process oxidizing organic material, and thus high barium concentrations commonly occur with high CH_4 concentrations. Site U1423 indicates that high dissolved Ba concentrations can occur without high CH_4 concentrations at depth, which is unusual. The lack of methane suggests that fluxes of organic material are relatively low.

Calcium, magnesium, and strontium

At the mudline, dissolved Ca concentration is 10.2 mM, which compares closely to the 10.4 mM inferred in JSPW (see "Geochemistry" in the "Methods" chapter [Tada et al., 2015b]). Calcium concentrations smoothly decrease to ~4.6 mM at 32 m CSF-A (Fig. F28). This is close to but shallower than the depth where alkalinity reaches a maximum (~51 m CSF-A). Deeper than 32 m CSF-A, Ca concentrations steadily rise, reaching 13 mM at the base of Hole U1423B (244 m CSF-A).

Magnesium concentration in the mudline sample (51.7 mM) is lower than that of inferred JSPW (53.3 mM) (see "Geochemistry" in the "Methods" chapter [Tada et al., 2015b]). Below the seafloor, dissolved Mg concentrations steadily decrease to 40 mM at ~22 m CSF-A. Deeper in the sediment column, Mg concentrations continue to decrease, reaching 23 mM at the base of Hole U1423B.

The Sr profile at Site U1423 is much smoother than at Site U1422, presumably because of improved shipboard analytical techniques. Dissolved Sr concentration is 87 µM at the seafloor, which compares to 92 µM inferred in JSPW (see "Geochemistry" in the "Methods" chapter [Tada et al., 2015b]). The shal-

lowest interstitial water sample at 1.45 m CSF-A has a Sr concentration of 93 µM. At ~27 m CSF-A, Sr concentrations begin to increase, reaching 172 µM at ~70 m CSF-A (Fig. F28). The initiation of the Sr rise, and by inference the release of Sr into interstitial water, occurs at approximately the same depth as the minimum in dissolved Ca, the inflection in dissolved Mg, and is ~20 m shallower than the maximum in alkalinity. Below 75 m CSF-A, Sr concentrations continue to increase, but the rate of increase is more gradual. Dissolved Sr is 202 µM at 244 m CSF-A.

As at Site U1422 (see "Geochemistry" in the "Site U1422" chapter [Tada et al., 2015b]), two primary processes impact the Ca, Mg, and Sr profiles at Site U1423. Between ~20 and 40 m CSF-A, there appears to be a phase that consumes Ca and Mg while releasing Sr. It is likely that dolomite [$Ca,Mg(CO_3)_2$] is precipitating in this interval, perhaps concurrent with dissolution of $CaCO_3$, which would add Sr to the interstitial water. The anomalous peak in $CaCO_3$ concentrations in the sediment occurs at the bottom of this interval at 41 m CSF-A. We note that the decrease in Mg concentrations (14 mM) is much greater than that of Ca concentrations (6 mM) over the upper 30 m (Fig. F28). Further discussion involving flux-based calculations of a dissolved species into and out of the horizon will aid this interpretation. Specifically, as evidenced by the diffusion gradients, dissolved Ca is also entering the "precipitation" horizon from depth, whereas dissolved Mg is leaving the precipitation horizon to depth. If one considers fluxes above and below the probable reaction interval, the consumption of Ca and Mg from interstitial water is much closer to 1:1, which is consistent with dolomite formation.

The other main process affecting the Ca, Mg, and Sr profiles at Site U1423 is basalt alteration, as was seen in many of the ODP Leg 127/128 interstitial water profiles (Murray et al., 1992). This general reaction consumes Mg and produces both Ca and Sr (Gieskes and Lawrence, 1981).

Salinity, chlorinity, sodium, and pH

Water beneath the thermocline in the marginal sea is often called JSPW. It has a practical salinity (*S*) of 34.06 ± 0.01 (Sudo, 1986). Once calibrated to molarity, measured concentrations of conservative ions in the mudline sample have values similar to JSPW (Table T11). This includes Cl^- and Na. We measured concentrations of 541 mM or 547 mol/kg of seawater for Cl^- and 468 mM or 473 mol/kg of seawater for Na, which compare to 551 mol/kg of seawater Cl^- and 473 mol/kg of seawater Na for seawater with *S* of 34.06.

The depth profiles of salinity, Cl^-, and Na each indicate a zone that is less saline than JSPW between the seafloor and ~52 m CSF-A (Fig. F29). Although salinity, Cl^-, and Na values are not measured precisely with standard shipboard instruments, they collectively suggest water with salinity ~32 in this depth interval. Interstitial water that is less saline than JSPW was also found in shallow sediment at sites drilled during Leg 127. At the time, the shipboard scientific party attributed the low-salinity waters to sulfate reduction (Tamaki, Pisciotto, Allan, et al., 1990). However, this does not seem a reasonable explanation because although sulfate reduction may decrease the total mass of dissolved ions in seawater, it would not decrease Cl^- or Na concentrations.

There appear to be two general possibilities for the relatively low salinity water. First, and given the proximity of Site U1423 to land, groundwater could be extending from the coast in relatively permeable horizons beneath the seafloor. This occurs along many continental margins, as seen, for example, at ODP drill sites across the New Jersey margin (Malone et al., 2002; van Geldern et al., 2013). Second, this water represents the evolving remnant of interstitial water that was in diffusive exchange with bottom water of the sea that was fresher sometime in the recent past. Most of the world's deep ocean water was more saline during the Last Glacial Maximum (LGM) relative to present day. As such, interstitial water salinity usually increases over the uppermost 40–50 m below the seafloor (Schrag et al., 1996; Adkins et al., 2002). However, this marginal sea has a complicated late Quaternary history, in part because shallow sills restrict deepwater flow to and from the adjacent Pacific Ocean (Oba et al., 1991). Low-salinity deep water during the LGM may explain the $\delta^{18}O$-depleted benthic foraminifers found in sediments of this age in this marginal sea (Oba et al., 1991).

Irrespective of origin, the presence of lower salinity water in shallow sediment will enhance deviations in concentration profiles.

Potassium

K concentration (Fig. F29) is ~10.1 mM in the mudline sample, which compares to 10.3 mM for inferred JSPW (see "Geochemistry" in the "Methods" chapter [Tada et al., 2015b]). After an increase to ~11.6 mM at 1.45 m CSF-A, concentrations remain high to deeper than 8.75 m CSF-A when K concentrations decrease steadily, reaching 7.4 mM at 244 m CSF-A. An increase in K concentrations immediately below the seafloor was also found at Site U1422 and may reflect exchange during authigenic mineral formation. The decrease in K concentrations with depth perhaps results from further reactions with ash and

basalt (Murray et al., 1992), although formation of glauconite would also remove K^+ from interstitial water (Föllmi and von Breymann, 1992).

It is noteworthy that K concentrations between 10 and 60 m CSF-A deviate from the general downhole trend to lower values. This deviation may result from the aforementioned freshening.

Lithium and boron

Li concentration (Fig. F30) is 22 µM in the mudline sample. Li values decrease to as low as 15 µM at 13 m CSF-A. Below this depth, Li concentrations increase to 110 µM at 244 m CSF-A.

B concentration (Fig. F30) is 412 µM at the mudline, which is approximately that of JSPW. Values increase to >1072 µM at the bottom of Site U1423 (244 m CSF-A). The profile is very similar to that presented for ODP Site 795 (Brumsack and Zuleger, 1992). They suggested multiple possible explanations for the downhole variations in B. We note that below 25 m CSF-A, B concentrations increase more rapidly than at shallower depths, suggesting that deep microbial reactions may somehow affect B concentrations in interstitial water.

Silica

Silica concentrations in interstitial water at Site U1423 (Fig. F30) increase from initial values of 98 µM in the bottom water (0 m CSF-A) to ~1550 µM at 244 m CSF-A. The opal-A/opal-CT boundary was not drilled at Site U1423, so the expected decrease in dissolved H_4SiO_4 at depth (Tamaki, Pisciotto, Allan, et al., 1990) was not observed.

The profile of Si measured using ICP-AES and the profile of H_4SiO_4 measured using the spectrophotometer match fairly well.

Preliminary conclusions

The geochemistry at Site U1423 has similarities and differences to that at Sites 794 and 795, as well as Sites U1422 and U1424. At all these sites, modest amounts of organic carbon land on the seafloor. Microbes then utilize this organic material to drive a series of reactions that conform to an established sequence (Froelich et al., 1979). The sum of the reactions releases HCO_3^-, PO_4^{3-}, and NH_4^+ to interstitial water, whereas component reactions affect concentrations of select dissolved constituents. For example, metal oxide reduction releases Mn and Fe to interstitial water and sulfate reduction removes SO_4^{2-} from interstitial water. The changing interstitial water composition also leads to mineral dissolution and precipitation.

Superimposed on this organic diagenesis framework are three other processes that impact all sites in the region. Two of these processes—alteration of basalt and recrystallization of biogenic silica—occur deeper than 300 m CSF-A but still affect water composition throughout the sediment column. The other apparently important process is changing chemistry at the seafloor, specifically the presence of lower salinity deep water in the recent past.

The primary difference between the sites is the degree of organic diagenesis, at least over long time frames. For example, CH_4 levels at Site U1422 are at least 16 times higher than those at Site U1423, and this leads to a prominent SMT and significant AOM at the first location. Potentially, different types of organic matter could cause major variations in alkalinity, NH_4^+, PO_4^{3-}, SO_4^{2-}, and CH_4 concentrations, as they are all involved in organic matter degradation. More likely though, differential supply of similar organic matter over time causes the variations at the sites.

Paleomagnetism

Paleomagnetic samples and measurements

Paleomagnetic investigations for cores collected at Site U1423 included the measurement of magnetic susceptibility of whole-core and archive-half split-core sections and of natural remanent magnetization (NRM) of archive-half sections. NRM was measured before and after alternating field (AF) demagnetization with a 20 mT peak field for all archive-half sections from Hole U1423A. Because of increased speed of core flow, NRM of archive-half sections from Holes U1423B and U1423C was measured only after 20 mT AF demagnetization at every 5 cm interval. The FlexIT core orientation tool (see **"Paleomagnetism"** in the "Methods" chapter [Tada et al., 2015b]) was used to orient 20 APC cores in Hole U1423A, starting from Core 346-U1423A-2H. Core orientation data collected in Hole U1423A are reported in Table **T13.**

We typically collected one paleomagnetic discrete cube sample (see **"Paleomagnetism"** in the "Methods" chapter [Tada et al., 2015b]) from the first section of each core in Hole U1423A, and occasionally from deep sections when the first section was not suitable for collecting a discrete cube sample. Four discrete samples were collected at deep depths from the bottom four cores in Hole U1423B, and two additional discrete samples were collected from Hole U1423C. Depth levels where the discrete samples were taken are marked by triangles along the left side of the paleomagnetic inclination data column in Fig-

ure F31. Stepwise AF demagnetization on 12 discrete samples from Hole U1423A, 1 discrete sample from Hole U1423B, and 2 discrete samples from Hole U1423C was performed at successive peak fields of 0, 5, 10, 15, 20, 25, 30, 35, 40, 45, 50, 55, and 60 mT to verify the reliability of the split-core measurements and to determine the demagnetization behavior of the recovered sediment. Following each demagnetization step, NRM of the discrete samples was measured with the sample placed in the "top-toward" or "+*z*-axis toward magnetometer" orientation (see "Paleomagnetism" in the "Methods" chapter [Tada et al., 2015b]) on the discrete sample tray.

We processed data extracted from the shipboard Laboratory Information Management System (LIMS) database by removing all measurements collected from disturbed and void intervals and all measurements that were made within 10 cm of the section ends, which are slightly biased by measurement edge effects. A modified version of the UPmag software (Xuan and Channell, 2009) was used to analyze the NRM data of both the split-core section and the discrete cube samples. The disturbed and void intervals used in this process are reported in Table T14. The processed NRM inclination, declination, and intensity data after 20 mT AF demagnetization are reported in Table T15 and shown in Figure F31.

Natural remanent magnetization and magnetic susceptibility

The intensity of NRM after 20 mT AF demagnetization in all three holes is similar in magnitude for overlapping intervals, mostly ranging from ~10^{-5} to 10^{-2} A/m. For core sections from the uppermost ~25 m, NRM intensity is on the order of 10^{-2} A/m. NRM intensity drops downcore to the order of 10^{-4} to 10^{-3} A/m between ~25 and ~50 m CSF-A. Deeper than ~50 m CSF-A until the bottom of the holes, NRM intensities are mostly on the order of ~10^{-4} A/m.

The AF demagnetization behavior of eight discrete samples from normal and reversed polarity intervals at varying depths is illustrated in Figure F32. Declination and inclination values acquired from the discrete sample measurement generally agree well with the split-core measurement after 20 mT AF demagnetization. All samples exhibit a steep, normal overprint that was generally removed after AF demagnetization at peak fields of ~10–15 mT, demonstrating that the 20 mT AF demagnetization is, in general, sufficient to eliminate the overprint. For measured discrete samples from deeper than ~50 m CSF-A, NRM intensities before and after stepwise demagnetizations are generally one magnitude lower than those from shallower than this level. NRM measurement of discrete samples from the deep depth with weak intensity values often appears to be significantly affected by an anhysteretic remanent magnetization, possibly acquired because of bias caused by ambient magnetic field during AF demagnetization.

Magnetic susceptibility measurements were taken on whole cores from all three holes as part of the Whole-Round Multisensor Logger (WRMSL) analysis and on archive-half split-core sections using the Section Half Multisensor Logger (SHMSL) (see "Physical properties"). The WRMSL-acquired susceptibility was stored in the database in raw meter units. These were multiplied by a factor of 0.68×10^{-5} to convert to the dimensionless volume SI unit (Blum, 1997). A factor of $(67/80) \times 10^{-5}$ was multiplied by the SHMSL-acquired susceptibility stored in the database. Magnetic susceptibility varies between 10×10^{-5} and 90×10^{-5} SI for sediment from the uppermost ~25 m of the holes and is generally $<10 \times 10^{-5}$ SI for sediment from below ~25 m CSF-A (Fig. F31, fourth panel). Magnetic susceptibility measurements are consistent between the two instruments and, in general, mimic NRM intensity, suggesting that the magnetic minerals that carry NRM are the same or at least coexist with those that dominate magnetic susceptibility.

Magnetostratigraphy

In spite of the drill string overprint and generally low NRM intensity, paleomagnetic inclination and declination data of the holes appear to show patterns that allow for the determination of magnetic polarity for the uppermost ~110 m of recovered sediment in Holes U1423A and U1423B. Both paleomagnetic declination and inclination after 20 mT AF demagnetization were used when possible for magnetostratigraphic interpretation at Site U1423. The geomagnetic field at the latitude of Site U1423 (41.6992°N) has an expected inclination of ~60.7°, assuming a geocentric axial dipole field model, which is sufficiently steep to determine magnetic polarity in APC cores that lack horizontal orientation. We identified the Brunhes/Matuyama boundary (0.781 Ma), the Jaramillo (0.988–1.072 Ma) and Olduvai (1.778–1.945 Ma) Subchrons, and the Matuyama/Gauss boundary (2.581 Ma) at Site U1423 (Table T16).

The Brunhes/Matuyama boundary is recorded at ~52.5 m CSF-A in Hole U1423A and at ~51.7 m CSF-A in Hole U1423B. Shallower than this boundary, inclination values after 20 mT AF demagnetization vary around the expected dipole inclination value of ~60.7°. Just deeper than this boundary, inclination is dominated by shallow and negative values. The two

discrete samples from 17.69 and 46.27 m CSF-A measured with stepwise AF demagnetization show stable and positive inclinations around the expected dipole value of ~60° (Fig. **F32A, F32B**). In Hole U1423A around this boundary, the FlexIT-corrected declination appears to change from values close to 0° to values mostly ~180°. The depth of the Brunhes/Matuyama boundary is consistent with the appearance of a tephra layer at ~45 m CSF-A, recognized as the "Hkd-ku," and with a known age of ~0.78 Ma (see **"Lithostratigraphy"**).

Between ~57.3 and ~61.2 m CSF-A in Hole U1423A, FlexIT-corrected declination shows values mainly around 0°, and inclination appears to be dominated by the expected normal polarity dipole value of the site. We interpret this ~4 m interval as the Jaramillo Subchron (C1r.1n, 0.988–1.072 Ma). In Hole U1423B, the Jaramillo Subchron is recognized between ~58.4 and ~62.3 m CSF-A with inclination varying mostly around the expected normal polarity dipole value (Fig. **F31B**).

Between ~76.4 and ~94.5 m CSF-A in Hole U1423A, the FlexIT-corrected declination values clearly vary around 0°, with inclination values dominated by the expected normal polarity dipole value. We interpret this interval as the Olduvai Subchron (C2n, 1.778–1.945 Ma). The declination of Core 346-U1423B-9H, although not oriented, shows an ~180° shift at ~76 m CSF-A, whereas inclination appears to change from shallow and negative values to mostly positive dipole values. This depth level is recognized as the top of the Olduvai Subchron recorded in Hole U1423B. The bottom of the Olduvai Subchron is not clearly recorded in Hole U1423B. The depth levels of the Olduvai Subchron in the holes are consistent with the LO of *Axoprunum acquilonium* (1.2–1.7 Ma) at ~74.14–93.17 m CSF-A in Hole U1423A (see **"Biostratigraphy"**).

At ~112 m CSF-A in Hole U1423A and ~113.6 m CSF-A in Hole U1423B, inclination after 20 mT AF demagnetization in both holes appears to change from shallow and negative values to dominant steep positive values. In Hole U1423A just deeper than this level, FlexIT-corrected declinations vary around 0°. We tend to interpret this level as the Matuyama/Gauss boundary (2.581 Ma). This interpretation agrees with the FO of *Cycladophora davisiana* (2.7 Ma) at ~112.06–121.7 m CSF-A in Hole U1423A. Deeper than ~140 m CSF-A in Holes U1423A and U1423B, inclination and declination both show large scatter, and it is difficult to make any reliable magnetostratigraphic interpretations. For the six measured APC cores recovered from Hole U1423C, inclination after 20 mT AF demagnetization shows mostly positive values that are apparently steeper than the expected dipole value. The lack of orientation and significant changes in paleomagnetic directions make it difficult for magnetostratigraphic interpretations for Hole U1423C.

Physical properties

Physical properties measurements at Site U1423 were conducted to provide high-resolution data on the bulk physical properties and their downhole variations in Holes U1423A and U1423B. High-resolution scanning at 2.5 cm intervals on whole-round sections was immediately performed with both the WRMSL (Sections 1, 2, and 3) and Special Task Multisensor Logger (STMSL) (Sections 4, 5, 6, and 7) after the cores were sectioned on the catwalk. The WRMSL was used to measure gamma ray attenuation (GRA) bulk density, magnetic susceptibility, and *P*-wave velocity, whereas the STMSL measured GRA bulk density and magnetic susceptibility. The GRA bulk density and magnetic susceptibility from each section were combined into individual core data sets for stratigraphic correlation. *P*-wave velocities measured in Sections 1, 2, and 3 with the WRMSL were consolidated into individual core data sets as well.

After the sections reached thermal equilibrium with the ambient room temperature of ~20°C, thermal conductivity (one per core) and NGR measurements (eight per full section) completed the suite of whole-core measurements. Cores were then split parallel to the core axis. One half was reserved for archiving and one half was for analysis and sampling (working half). Shear stress measurements (one per core) were performed on the working halves of Hole U1423A and the lower part of Hole U1423B (below 205 m CSF-A) with more success. Moisture and density measurements were performed on discrete core samples (two per core) collected from the working halves of Hole U1423A and the lower part of Hole U1423B. Spectral diffuse reflectance (mostly at 1 cm intervals) and point magnetic susceptibility (mostly at 2 cm intervals) were measured using the SHMSL on the archive halves. Physical properties measurements are presented in Figures **F33, F34, F35,** and **F36.**

Thermal conductivity

Thermal conductivity was measured once per core using the full-space probe, usually near the middle of Section 4. Thermal conductivity values range from ~0.8 to ~1.1 W/(m·K). Values are largely scattered from 0 to 120 m CSF-A and nearly constant at ~0.9 W/(m·K) deeper than 120 m CSF-A. This highly variable feature in lithologic Subunits IA, IB, and IIA and the lack of an increasing trend downhole suggest a compositional control on this parameter.

Moisture and density

GRA wet bulk density was measured using the WRMSL and STMSL. Although measurement error exists in GRA bulk density data because of the presence of air between sediments and the core liner, in general, GRA bulk density tends to reflect the characteristic of each lithologic unit (Fig. F33; see "Lithostratigraphy"). Similar to Site U1422, GRA bulk density at Site U1423 is highly variable in the upper part (between 0 and 103 m CSF-A) with values ranging from 1.2 to 1.8 g/cm^3. High variations of GRA bulk density in this interval are closely related to the alternating very dark brown to black organic-rich sediment and lighter olive and green hemipelagic sediment. This relationship is matched well with the high GRA bulk density values characteristic of the dark layer–organic rich intervals in Site U1422. After sharply decreasing at ~103 m CSF-A, coinciding with the lithologic Unit I/II boundary, GRA bulk density tends to decrease slightly with depth to 249 m CSF-A. GRA bulk density at Site U1423 correlates well with the density log acquired in open Hole U1423B (see Fig. F37 and "Downhole measurements").

Although discrete wet bulk density and grain density are relatively constant for the entire interval, ranging from 1.2 to 1.6 g/cm^3 and from 2.4 to 2.8 g/cm^3, respectively, the primary trends agree well with GRA bulk density (Fig. F35). Porosity and water content show generally reversed trends when compared to density, ranging from 68.1% to 84.7% and from 45.0% and 70.5%, respectively. Discrete bulk density and grain density have small step increases between 0 and 20 m CSF-A, where porosity and water content of the sediment decrease inversely. The trend of increasing density downhole reverses at ~20 m CSF-A and then generally decreases to the bottom of the hole. Porosity and water content gradually increase below 20 m CSF-A and vary highly with depth. However, all discrete bulk density, grain density, porosity, and water content measurements remain relatively constant from 103 m CSF-A to the bottom of the hole, corresponding to lithologic Unit II. The largest scatter of discrete bulk density and porosity occurs between 55 and 75 m CSF-A.

Magnetic susceptibility

Magnetic susceptibility is the degree to which a material can be magnetized by an external magnetic field. Therefore, magnetic susceptibility provides information about sediment composition. Magnetic susceptibility at Site U1423 generally decreases with depth (Fig. F33). Although the mean values remain between 10 × 10^{-5} and 20 × 10^{-5} SI for this site, the highest magnetic susceptibility readings occur shallower than ~22 m CSF-A (average = 91.5 × 10^{-5} SI) with high variation. A magnetic susceptibility maximum occurs between 20 and 22 m CSF-A, where values as high as 200 × 10^{-5} SI were measured. This occurrence of high magnetic susceptibility in the uppermost part (as was also the case with Site U1422) is likely due to highly magnetic authigenic mineral formation because there is no apparent primary lithologic correspondence to this region (see "Lithostratigraphy"). This lack of correlation between magnetic susceptibility and decimeter-scale lithology also suggests a diagenetic influence is decreasing the signal between 0 and 22 m CSF-A near the SMT zone with the signal severely muted deeper. After a large step decrease of magnetic susceptibility between 22 and 25 m CSF-A, magnetic susceptibility tends to decrease slightly downhole, with the exception of spikes of low magnetic susceptibility from 110 to 123 m CSF-A. Magnetic susceptibility also shows a small decrease at ~70 m CSF-A.

Point magnetic susceptibility from the SHMSL agrees with the whole-core trends as well (Fig. F33), but values become significantly greater with depth than the whole-core equivalents. The increasing gap between two magnetic susceptibility values in the lower part of the hole may be related to fractures in the whole-core sediment and the inherent smoothing imposed by the magnetic susceptibility loop, resulting in reduced the whole-core intensity.

Natural gamma radiation

The variation patterns of NGR are conformable with GRA bulk density and correlate well with the total gamma ray log acquired in open Hole U1423B (see Fig. F37 and "Downhole measurements"). Between 0 and 20 m CSF-A, the total NGR counts show a large step increase from 15 to 40 cps and then slightly increase to 70 m CSF-A. Although the total NGR counts show strong cyclicity between 20 and 125 m CSF-A, the highest NGR counts (82 cps) occur at ~70 m CSF-A, corresponding to a maximum in GRA bulk density. NGR counts gradually decrease between 70 and 125 m CSF-A, which coincides with the lithologic Subunit IIA/IIB boundary and also approximates the depth at which the logging Subunit LIa/LIb boundary has been placed (see Fig. F38). The sharp decrease from 40 to 17 cps near 103 m CSF-A coincides with the Unit I/II boundary and the depth of decreasing GRA bulk density and magnetic susceptibility. As discussed at Site U1422, these variation patterns of NGR may be explained by increased U associated with organic-rich layers in Unit I. This interpretation is in agreement with the downhole spectral gamma ray measurements performed in Hole U1423B, evidencing a higher mean uranium

content above ~103 mbsf compared to the rest of the hole (see Fig. F38). Subsequently, low NGR counts remain stable to 180 m CSF-A with relatively less scatter. NGR counts again slightly decrease between 180 and 200 CSF-A and then inversely increase to the bottom of the hole.

Compressional wave velocity

Compressional *P*-wave velocity was measured with the WRMSL in Sections 1, 2, and 3 of each core for Holes U1423A and U1423B. Although *P*-wave velocity is generally measured with the WRMSL after the sections reach thermal equilibrium with the ambient room temperature of ~20°C because *P*-wave velocity is significantly affected by temperature (Shumway, 1958), *P*-wave velocity at Site U1423 was measured before temperature equilibrium (~12°C) for quick stratigraphic correlation. Therefore, we remeasured *P*-wave velocity after temperature equilibrium (~20°C) in Cores 346-U1423B-3H, 7H, and 16H to compare with *P*-wave velocity measured before temperature equilibrium (~12°C). The two sets of *P*-wave velocity values matched well (Fig. F34) with average maximum differences of 5 m/s (i.e., Core 3H was 1509 m/s before and 1514 m/s after, Core 7H was 1517 m/s before and 1519 m/s after, and Core 16H was 1525 m/s before and 1526 m/s after). However, because of poor sediment-to-liner coupling or the influence of small cracks in the relatively stiff and brittle sediment, results from the WRMSL include significantly higher or lower values than a typical data set. These values were removed manually, and then the *P*-wave velocity was combined as one data set of values from each hole (Fig. F33).

P-wave velocity at Site U1423 varies from 1451 to 1570 m/s (average = 1524 m/s) and generally increases with depth. Although *P*-wave velocity also shows relatively higher variation above 103 m CSF-A relative to the lower part, the trend is not clear enough to reflect the lithologic changes.

Vane shear stress

Undrained shear strength of soft sediment in the working half of the core was measured using an analog vane shear device. Shear strength ranges from 5.5 to 126 kPa and generally increases with depth (Fig. F35). In spite of the small scatter in the values, the curve does not show general trends that can be divided into successive intervals, although shear strength values at some depths (e.g., ~56 and ~189 m CSF-A) reflect well the composition of sediment. Although the stratigraphic distance between two measurements obtained from a black organic layer (56.45 m CSF-A) and a paired light green hemipelagic layer (56.55 m CSF-A) of Core 346-U1423A-7H is only 10 cm, shear strength sharply increases from 39.6 to 50.1 kPa in this interval. Shear strength abruptly decreases at 189 m CSF-A, where a highly diatomaceous layer occurs. The high fluid content in the diatomaceous layer at this depth is likely responsible for this decrease in shear strength.

Diffuse reflectance spectroscopy

Color reflectance data measured on the split archive-half sections show high variation of color, especially between 0 and 100 m CSF-A (Fig. F36). The L*, a*, and b* values represent lightness, red-green ratio, and yellow-blue ratio, respectively. These variations in color reflectance are closely related to lithologic changes. For example, the lithologic characteristic of Unit I, which consists of alternating very dark brown to black organic-rich sediment and lighter olive and green hemipelagic sediment, is responsible for the high variation of color reflectance. As was the case at Site U1422, as the dark bands fade out downhole in Unit II the color reflectance of L* and a* shows little variation to the bottom of the hole.

Summary

Physical properties measured at Site U1423 generally show trends that follow lithostratigraphy. Magnetic susceptibility, bulk density, and NGR have higher values in lithologic Unit I than in Unit II, whereas porosity and water content show opposite trends. *P*-wave velocity and shear strength gradually increase with depth because of sediment compaction. Color reflectance shows higher variation in lithologic Unit I than in Unit II, and the variations are closely related to the lithology of Unit I, which consists of alternating very dark brown to black organic-rich bands and lighter olive to green hemipelagic sediment.

Downhole measurements

Logging operations

Downhole logging measurements in Hole U1423B were made after completion of APC coring to a total depth of 249.1 m CSF-A. In preparation for logging, the hole was circulated and the pipe was pulled up to 80 m CSF-A. Two tool strings were deployed in Hole U1423B: the paleo combo and FMS-sonic (Fig. F39) (see "Downhole measurements" in the "Methods" chapter [Tada et al., 2015b]; for tool acronyms see Table T12 in the "Methods" chapter [Tada et al., 2015b]).

On 22 August 2013 at 0915 h UTC, the paleo combo tool string (comprising resistivity, density, NGR, and magnetic susceptibility tools) descended from the rig

floor into the pipe. A downlog was taken at ~600 m/h and reached the base of the hole at ~251 m WSF (see "Downhole measurements" in the "Methods" chapter [Tada et al., 2015b]). The hole was logged up (Pass 1) to ~121 m WSF at 540 m/h. The tool string returned for a second pass (main pass) from the bottom of the hole to the seafloor.

The FMS-sonic was rigged at ~1200 h on 22 August. A downlog was taken at 850 m/h, from which we established the best settings for the source frequency and the automated picking of *P*-wave velocity from the sonic waveforms. The tool string reached the base of the hole at 250.7 m WSF. Two uphole passes of the FMS-sonic were run, Pass 1 to ~120 m WSF and Pass 2 to the seafloor, both at 550 m/h. Rig down was completed at 1855 h.

The seafloor depth was given by the step in the gamma logs. There is typically some variability in choosing the exact point because the seafloor can appear as a gradual change. The paleo combo downlog found the seafloor at 1794.5 m WRF and the uplog (Pass 2) found it at 1793.5 m WRF. The second pass of the FMS-sonic found the seafloor at 1795.2 m WRF, compared to the drillers mudline tagged at 1796.8 mbrf (Hole U1423B). Tides were negligible and seas were calm (maximum peak-to-peak heave of 20 cm), giving little contribution to the offset between the FMS-sonic and the paleo combo downlog and uplog seafloor depths. The remaining difference possibly comes from wireline stretching. A reasonably good depth match of the open hole NGR logs between logging runs and with the core data was achieved using a seafloor of 1794.6 m WRF for paleo combo Pass 2 and 1794.2 m WRF for the second pass of the FMS-sonic.

Logging data quality

Tool calibration was performed both before and after the logging runs to ensure quality control. In Hole U1423B, borehole conditions were good with a baseline diameter (12–13 inches) close to the bit size (9.875 inches) (Fig. F37). Only a short section larger than 13 inches, although not exceeding 14 inches, was found between ~157 and 167 mbsf. As a consequence of good borehole conditions and negligible heave during downhole logging data acquisition, log data quality is generally very good.

Agreement between physical properties data and logging data is excellent for the density and NGR logs along almost the entire borehole (Fig. F37, Columns 2 and 3). From ~125 mbsf to the pipe entrance, the uplog gamma ray data, however, deviates from the core NGR data to lower values and no longer overlaps with the downlog (Fig. F37, Column 2). The gamma ray and density data are corrected from borehole diameter, although as the caliper was closed over this interval, the data quality is no longer ensured. We related this shift to be the result of an artificial correction of the gamma ray signal from the borehole size, with the caliper reading a smaller hole diameter than the actual size. For the same reason, the density log shows slightly lower values than the core data over the same interval. The natural and spectral gamma ray and density downlogs should thus be preferred for interpretations over this interval (from ~125 mbsf to the pipe entrance). Also, natural and spectral gamma ray data recorded shallower than 80 mbsf should only be used qualitatively because of the attenuation of the signal through the pipe (Fig. F37). The resistivity curve worked well, except for some high-frequency noise on the uplog starting ~40 m below the pipe and increasing uphole. The downlog should be preferred for interpretations.

The Magnetic Susceptibility Sonde tool diagnostics were normal during the runs. However, because of the very low magnetic susceptibility signal in the sediment, we were possibly operating at the lower limits of detection in the tool. The sensor electronics are sensitive to borehole temperature, and the acquired magnetic susceptibility data were thus strongly affected by a nonlinear long-period temperature-related drift superimposed on low signal variability. Preliminary processing was completed offshore to remove the temperature drift by calculating a least-squares polynomial fit to the data and subtracting the calculated trend from the data set. The residual components from both the high-resolution and deep readings are plotted in Figure F37 (Column 5) and should be an indication of the magnetic signal variability in the formation. The drift-corrected high-resolution log correlates relatively well with the magnetic susceptibility measurements on cores, especially shallower than 150 mbsf and deeper than 205 mbsf. The corrected deep-reading low-resolution log is generally inversely correlated with the density log. Further processing remains necessary. The velocity log shows a downhole increasing trend with higher values than the *P*-wave velocities measured on cores, especially deeper than 180 mbsf (Fig. F37, Column 6). The FMS resistivity images were of excellent quality because of good contact with the borehole wall (Fig. F38).

Logging units

The Hole U1423B logs change gradually downhole, with no major steps in base levels. The entire logged interval was thus assigned to one logging unit (LI; Fig. F37). At the scale of this unit, the upper part

(from below pipe to ~123 mbsf) is characterized by higher gamma ray, density, and resistivity than the rest of the hole. The sonic velocity log increases downhole, reflecting low sediment compaction with depth. Resistivity has a negative downhole gradient rather than the normal increasing downhole compaction trend (see below). Density decreases in the upper part of the hole and remains relatively flat deeper in the hole. The above log trends and their correlation with in situ lithologies (see below) are generally in good agreement with the logging data acquired during Legs 127 and 128 at ODP Sites 794B, 795, 797, and 798, which show similar patterns.

The Hostile Environment Natural Gamma Ray Sonde signal ranges on average from 20 to 45 gAPI, with peak values reaching 70 gAPI. The signal shows moderately high amplitude variability on a several-meter to submeter scale, and given the sedimentological context (see **"Lithostratigraphy"**), it most likely tracks clay and organic matter content (silica and calcite contain no radioactive elements). The potassium and thorium curves are generally well correlated (Fig. **F38**). Uranium behaves differently from potassium and thorium because it is not chemically combined in the main terrigenous minerals. It does, however, show locally good correlations with thorium and potassium, particularly where prominent peaks are observed in the total gamma ray log. Uranium generally accounts for 25%–45% of the total gamma radiation signal, and locally for >50%. Uranium is usually associated with the organic matter–rich intervals in lithologic Unit I (above ~82.5 mbsf, see **"Lithostratigraphy"**), in which it shows the highest values (see below). The uranium content remains relatively high in lithologic Unit II (from ~82.5 mbsf to the bottom of the hole), which is less rich in organic matter.

Logging Unit LI has been divided into two subunits on the basis of changes in character of gamma ray and density logs.

Logging Subunit LIa: base of drill pipe (~80 mbsf) to ~124 mbsf

The upper logging subunit is characterized by moderate to high-amplitude swings in NGR (and its U, Th, and K components), with an overall decreasing downhole trend. The gamma ray signal correlates well with the bulk density log, which shows high-amplitude variations ranging from 1.25 to 1.55 g/cm^3 (Fig. **F37**). The sonic curve is relatively flat, with values generally increasing downhole. Below ~103 mbsf, progressive decreases in U, Th, and K contents are observed, likely reflecting a decrease in organic matter and clay content. Slightly higher values in K content are, however, observed between ~107 and ~115 mbsf (Fig. **F38**). The depth of ~103 mbsf fits well with the transition between lithologic Unit I (primarily fine-grained material derived from terrigenous sources with color banding that is suggested to be related to variable content of organic matter and pyrite) and Unit II (dominantly composed of moderate to heavily bioturbated diatomaceous silty clay and clay and diatom ooze), placed in Section 346-U1423A-12H-1 at ~103.35 m CSF-A (see **"Lithostratigraphy"**) and reflecting a significant downhole increase in diatom content relative to terrigenous sediment.

The main changes in character of the downhole logs have been correlated with the base of logging Subunit LIa, which approximates the depth of the lithologic Subunit IIA/IIB boundary, placed at ~121 m CSF-A in Hole U1423A (Section 346-U1423A-14H-1) (see **"Lithostratigraphy"**). From a sedimentological point of view, however, no clear characteristic allowed straightforward division of lithologic Unit II into Subunits IIA and IIB. The relative decrease in NGR core and downhole log values was the basis for differentiating these two lithologic subunits (see also **"Physical properties"**).

Logging Subunit LIb: ~124–250 mbsf

Logging Subunit LIb is distinguished from logging Subunit LIa by lower values in total and spectral NGR, likely reflecting the abundance of nonradioactive elements within lithologic Subunit IIB (diatoms and other siliceous components, see **"Lithostratigraphy"**). Logging Subunit LIb is also characterized by moderate-amplitude swings in NGR and its U, Th, and K components. Two prominent peaks in at least two of these components are observed at ~142 and ~193 mbsf and correlate well with the NGR data measured on cores. The peak observed at ~193 mbsf does not correlate with anything obvious in the cored sediment. The peak at ~142 mbsf may correspond to a prominent ash layer, which is >10 cm thick (interval 346-U1423B-16H-6, 84–96 cm). This ash layer is also clearly associated with a peak in the density log. Another peak in density at ~238 mbsf also correlates with a thick ash layer in interval 346-U1423B-27H-6, 23–33 cm, and a prominent peak in the NGR data measured on the core. Logging Subunit LIb is also distinguished from logging Subunit LIa by lower values in bulk density, showing a relatively uniform trend, with values <1.45 g/cm^3 associated with lower amplitude oscillations compared to Subunit LIa. Sonic velocity increases downhole. At the borehole scale, the resistivity curves show an opposite trend to the sonic curve, with mean values decreasing downhole from 0.9 to 0.4 Ωm, although this gradient becomes gentler in logging Subunit LIb.

Similar downhole decreasing resistivity patterns have also been observed at Sites 794, 795, 797, and 798 (Ingle, Suyehiro, von Breymann, et al., 1990; Tamaki, Pisciotto, Allan, et al., 1990) and in the upper 300 m of the sediment column. This negative gradient is likely due to the increasing temperature with depth and the high porosities (see **"Physical properties"**), making the physical properties of the pore water dominate the resistivity log response. The prominent peak in magnetic susceptibility observed at ~206 mbsf on both core and log data correlate well with a dark ash layer found in interval 346-U1423B-24H-4, 129–131 cm.

FMS images

Because of the good borehole conditions in Hole U1423B, the FMS resistivity data quality allows the borehole formation resistivity to be interpreted at several scales. At the scale of the borehole, the interval above ~206 mbsf is characterized by relatively high conductivities (dark colored upper interval in the FMS image in Fig. **F38**) and high resistivities below (light color in the FMS image). This change does not correlate in core with any major change in lithology (see **"Lithostratigraphy"**). At a finer scale, the FMS images reveal numerous resistive and conductive intervals, with thicknesses ranging from several tens of centimeters to a few meters. As an example, the conductive intervals observed from 110 to 126 mbsf on the FMS images generally correlate with lower values in the gamma ray, bulk density, and resistivity logs (Fig. **F40**) and seem to correspond in cores, although not always, to brownish intervals. These intervals contrast with lighter, more grayish intervals that are less conductive on the FMS images and correlate with higher values in the NGR, bulk density, and resistivity logs. Transitions between alternations are mainly gradual, although some sharp contacts are observed locally. Inclined bedding (appearing as sinusoids) at slight angles is observed at some depths. It will be possible to map their occurrence and measure dip directions and angle. As shown in Figure **F41,** decimetric to centimetric resistive and conductive intervals are also clearly observed in the bottom part of the hole (234–243 mbsf) in an interval dominated by homogeneous lithology (diatomaceous silty clay and clay and diatomite ooze, see **"Lithostratigraphy"**). The conductive layers correlate in cores with intervals characterized by low gamma ray and high L* values, possibly reflecting an increase in biosiliceous fraction content. These initial correlations need to be further examined by shore-based research. FMS resistivity images also reveal stratigraphic information at a finer spatial resolution than the standard logs. In Figure **F41,** the highly resistive layers around 236.4 and 238 mbsf (with thicknesses ~0.1 m), correlate with two thick ash layers observed in intervals 346-U1423B-27H-5, 0–10 cm, and 27H-6, 23–33 cm. Other ash layers are also observed at other depths on the FMS images (e.g., Fig. **F40**).

In situ temperature and heat flow

APCT-3 downhole temperature measurements were performed in Hole U1423A at five depths, including the mudline. In situ temperatures range from 5.50°C at 35.8 m CSF-A to 17.45°C at 121.3 m CSF-A (Table **T17**), with a linear downhole increase indicating that the gradient is uniform with depth (Fig. **F42**). A linear fit of temperature versus depth gives a geothermal gradient of 140°C/km. This value is higher than was measured at Site U1422 (134°C/km). The bottom water temperature at this site is estimated to be 0.47°C, based on the average mudline temperature in the four APCT-3 measurements. A heat flow of 133 mW/m^2 was obtained from the slope of the linear fit between in situ temperature and calculated in situ thermal resistance (Pribnow et al., 2000). This value is also higher than the one calculated at Site U1422 (120 mW/m^2).

Stratigraphic correlation and sedimentation rates

Real-time tracking of the relative positions of core gaps among the various holes at Site U1423 was accomplished using magnetic susceptibility and GRA data from the WRMSL and STMSL. Data were collected at resolutions of either 2.5 or 5 cm, depending on the capacity to keep up with core recovery rates. Detailed (centimeter scale) compositing and splicing (see **"Stratigraphic correlation and sedimentation rates"** in the "Methods" chapter [Tada et al., 2015b]) are based on the high-resolution RGB (blue) color data recovered from the Section Half Imaging Logger at 0.5 cm resolution. For detailed discussion of these data sets, see **"Physical properties"** in the "Methods" chapter (Tada et al., 2015b).

After all cores were composited, a continuous splice was constructed spanning 0–218.8 m CCSF-D (as defined in the **"Methods"** chapter [Tada et al., 2015b]). All three holes were required to construct the splice; a combination of drilling disturbance and poor recovery within the interval from ~144 to ~184 m CSF-A prevented construction of a complete splice from Holes U1423A and U1423B alone. In addition, at three depths, between-core gaps in Holes U1423A and U1423B were aligned. Finally, a 6.5 m interval was also missing because of 0% recovery of Core 346-

U1423B-18H. Consequently, a detailed drilling plan was constructed to recover these missing intervals in Hole U1423C, as described below. The resulting composite and splice ranges from the top of Core 346-U1423A-1H to the bottom of Core 346-U1423B-24H at 218.8 m CCSF-D (211.2 m CSF-A) (Tables **T18, T19;** Fig. **F43**). Only Hole U1423B extends deeper than this depth, to Core 346-U1423B-28H at 256.9 m CCSF-A (249.3 m CSF-A). The length of the splice (218.8 m CCSF-D) relative to the length of the uncomposited section (211.2 m CSF-A) indicates that expansion at this site is minimal (3.8%).

A CCSF-C scale (as defined in **"Stratigraphic correlation and sedimentation rates"** in the "Methods" chapter [Tada et al., 2015b]) was created for this site, extending to ~90 m CSF-A, covering Subunit IA as defined in **"Lithostratigraphy."** Construction of the CCSF-C scale is based on centimeter-scale correlation of structure in the RGB (blue) data. These CCSF-C depth maps (CSF-A to CCSF-D) are provided for Holes U1423A and U1423B in Table **T20.**

Detailed drilling at Hole U1423C to recover between-core gaps

Hole U1423C was selectively cored to recover sections not recovered in Holes U1423A and U1423B. Hole U1423C was drilled without recovery to ~114 m CSF-A. This 114 m washed interval is designated in the coring sequence as Core 346-U1423C-11, as required by IODP terminology. The suffix "11" refers to Core "1" drilled Interval "1." The wash interval was followed by two APC cores (2H and 3H) to establish the stratigraphic relationship relative to Holes U1423A and U1423B. The next APC core (4H) successfully recovered the first of the three targeted gaps. While the stratigraphic correlation was taking place, the bit was held at the top of the previously cored interval in order to minimize disturbance at the top of the following core. Following stratigraphic correlation, the bit was advanced the length of the previously recovered core (referred to on the rig floor as "cleaning out the rathole") and the hole was washed an additional 7.5 m (Core 52 [drilled Interval 2 in Core 5]) in order to place the APC such that it would recover the missing 6.5 m interval in the middle of the following 9.6 m stroke. Following recovery of this interval, the hole was washed another 2 m (Core 73 [drilled Interval 3 in Core 7]) in order to place the last two gaps in the middle of the next two APC strokes. After successful recovery of these last two remaining gaps, the hole was terminated. The success of this detailed drilling effort was greatly aided by ideal conditions: near zero heave and a sediment lithology conducive to full stroke recovery with little to no expansion. This targeted approach resulted in considerable time savings, compared to coring the entire hole top to bottom.

Age model and sedimentation rates

A preliminary age model (Fig. **F44**) was established on the basis of all available biostratigraphic and paleomagnetic age control points. For details, see **"Biostratigraphy," "Paleomagnetism,"** and **"Lithostratigraphy."** At this site, no datums were excluded from the assessment, although three datums defined as the LOs of *Proboscia curvirostris* and *Actinocyclus oculatus* and the rapid decrease of *Siphocampe arachnea* group could be affected by reworking. Eight linear depth-age segments utilizing all the paleomagnetic events as well as the FO of *Neodenticula koizumii*, and the LO of *Thalassiosira jacksonii* provide a well-constrained preliminary age model (Fig. **F44A**). Sedimentation rate (Fig. **F44B**) ranges from 21 to 121 m/m.y., moderate in the upper Subunit IA, low in the lower Subunit IA and Subunit IIA, and high in Subunits IB and IIB, possibly reflecting the change in siliceous productivity. Estimated ages of subunit boundaries are 1.8, 2.2, and 3.0 Ma for the Subunit IA/IB, IB/IIA, and IIA/IIB boundaries, respectively.

References

Adkins, J.F., McIntyre, K., and Schrag, D.P., 2002. The salinity, temperature, and $\delta^{18}O$ of the glacial deep ocean. *Science,* 298(5599):1769–1773. **doi:10.1126/science.1076252**

Backman, J., Moran, K., McInroy, D.B., Mayer, L.A., and the Expedition 302 Scientists, 2006. *Proc. IODP,* 302: Edinburgh (Integrated Ocean Drilling Program Management International, Inc.). **doi:10.2204/iodp.proc.302.2006**

Berner, R.A., 1980. *Early Diagenesis: A Theoretical Approach:* Princeton, NJ (Princeton Univ. Press).

Berner, R.A., 1981. A new geochemical classification of sedimentary environments. *J. Sediment. Res.,* 51(2):359–365. **doi:10.1306/212F7C7F-2B24-11D7-8648000102C1865D**

Bernhard, J.M., Goldstein, S.T., and Bowser, S.S., 2010. An ectobiont-bearing foraminiferan, *Bolivina pacifica,* that inhabits microxic pore waters: cell-biological and paleoceanographic insights. *Environ. Microbiol.*, 12(8):2107–2119. **doi:10.1111/j.1462-2920.2009.02073.x**

Bernhard, J.M., and Sen Gupta, B.K., 1999. Foraminifera of oxygen-depleted environments. *In* Sen Gupta, B.K., (Ed.), *Modern Foraminifera:* Dordrecht (Kluwer Academic Publishers), 201–216. **doi:10.1007/0-306-48104-9_12**

Blum, P., 1997. Physical properties handbook: a guide to the shipboard measurement of physical properties of deep-sea cores. *ODP Tech. Note,* 26. **doi:10.2973/odp.tn.26.1997**

Brady, G.S., 1880. Report on the Ostracoda dredged by *HMS Challenger* during the years 1873–76. *Rep. Sci.*

Results of the Voyage of HMS Challenger during the years 1873–76, Zoology, 3:1–184.

Brumsack, H.-J., and Zuleger, E., 1992. Boron and boron isotopes in pore waters from ODP Leg 127, Sea of Japan. *Earth Planet. Sci. Lett.,* 113(3):427–433. **doi:10.1016/0012-821X(92)90143-J**

Cha, H.J., Lee, C.B., Kim, B.S., Choi, M.S., and Ruttenberg, K.C., 2005. Early diagenetic redistribution and burial of phosphorus in the sediments of the southwestern East Sea (Japan Sea). *Mar. Geol.,* 216(3):127–143. **doi:10.1016/j.margeo.2005.02.001**

Föllmi, K.B., Cramp, A., Föllmi, K.E., Alexandrovich, J.M., Brunner, C., Burckle, L.H., Casey, M., deMenocal, P., Dunbar, R.B., Grimm, K.A., Holler, P., Ingle, J.C., Jr., Kheradyar, T., McEvoy, J., Nobes, D.C., Stein, R., Tada, R., von Breymann, M.T., and White, L.D., 1992. Dark–light rhythms in the sediments of the Japan Sea: preliminary results from Site 798, with some additional results from Sites 797 and 799. *In* Pisciotto, K.A., Ingle, J.C., Jr., von Breymann, M.T., Barron, J., et al., *Proc. ODP, Sci. Results,* 127/128 (Pt. 1): College Station, TX (Ocean Drilling Program), 559–576. **doi:10.2973/odp.proc.sr.127128-1.159.1992**

Föllmi, K.B., and von Breymann, M., 1992. Phosphates and glauconites of Sites 798 and 799. *In* Pisciotto, K.A., Ingle, J.C., Jr., von Breymann, M.T., Barron, J., et al., *Proc. ODP, Sci. Results,* 127/128 (Pt. 1): College Station, TX (Ocean Drilling Program), 63–74. **doi:10.2973/odp.proc.sr.127128-1.116.1992**

Froelich, P.N., Klinkhammer, G.P., Bender, M.L., Luedtke, N.A., Heath, G.R., Cullen, D., Dauphin, P., Hammond, D., Hartman, B., and Maynard, V., 1979. Early oxidation of organic matter in pelagic sediments of the eastern equatorial Atlantic: suboxic diagenesis. *Geochim. Cosmochim. Acta,* 43(7):1075–1090. **doi:10.1016/0016-7037(79)90095-4**

Gieskes, J.M., and Lawrence, J.R., 1981. Alteration of volcanic matter in deep-sea sediments: evidence from the chemical composition of interstitial waters from deep sea drilling cores. *Geochim. Cosmochim. Acta,* 45(10):1687–1703. **doi:10.1016/0016-7037(81)90004-1**

Hanai, T., Ikeya, N., and Yajima, M., 1980. Deep-sea Ostracoda from Deep Sea Drilling Project Site 435, Japan Trench. *In* Scientific Party, *Init. Repts. DSDP,* 56/57 (Pt. 2): Washington (U.S. Govt. Printing Office), 907–909. **doi:10.2973/dsdp.proc.5657.130.1980**

Ingle, J.C., Jr., Suyehiro, K., von Breymann, M.T., et al., 1990. *Proc. ODP, Init. Repts.,* 128: College Station, TX (Ocean Drilling Program). **doi:10.2973/odp.proc.ir.128.1990**

Kucera, M., and Kennett, J.P., 2000. Biochronology and evolutionary implications of late Neogene California margin planktonic foraminiferal events. *Mar. Micropaleontol.,* 40(1–2):67–81. **doi:10.1016/S0377-8398(00)00029-3**

Machida, H., and Arai, F., 2003. *Atlas of Tephras in and around Japan* (revised ed.)*:* Tokyo (Univ. Tokyo Press).

Maiya, S., 1978. Late Cenozoic planktonic foraminiferal biostratigraphy of the oil-field region of northeast Japan. In *Cenozoic Geology of Japan:* Osaka, 35–60. (in Japanese, with abstract in English)

Malone, M.J., Claypool, G., Martin, J.B., and Dickens, G.R., 2002. Variable methane fluxes in shallow marine systems over geologic time: the composition and origin of pore waters and authigenic carbonates on the New Jersey shelf. *Mar. Geol.,* 189(3–4):175–196. **doi:10.1016/S0025-3227(02)00474-7**

Masuzawa, T., and Kitano, Y., 1983. Interstitial water chemistry in deep-sea sediments from the Japan Sea. *J. Oceanogr. Soc. Jpn.,* 39(4):171–184. **doi:10.1007/BF02070261**

Masuzawa, T., and Kitano, Y., 1984. Appearance of H_2S-bearing bottom waters during the last glacial period in the Japan Sea. *Geochem. J.,* 18(4):167–172. **doi:10.2343/geochemj.18.167**

Matsumoto, R., 1992. Diagenetic dolomite, calcite, rhodochrosite, magnesite, and lansfordite from Site 799, Japan Sea—implications for depositional environments and the diagenesis of organic-rich sediments. *In* Pisciotto, K.A., Ingle, J.C., Jr., von Breymann, M.T., Barron, J., et al., *Proc. ODP, Sci. Results,* 127/128 (Pt. 1): College Station, TX (Ocean Drilling Program), 75–98. **doi:10.2973/odp.proc.sr.127128-1.119.1992**

Middelburg, J.J., de Lange, G.J., and van der Weijden, C.H., 1987. Manganese solubility control in marine pore waters. *Geochim. Cosmochim. Acta,* 51(3):759–763. **doi:10.1016/0016-7037(87)90086-X**

Miwa, M., 2014. Foraminifera. In *Sekiyu Kogyo Binran (Petroleum Technology Handbook) 2013:* Tokyo (Jpn. Assoc. Pet. Technol.), 223–227 (in Japanese).

Murray, R.W., Brumsack, H.J., von Breymann, M.T., Sturz, A.A., Dunbar, R.B., and Gieskes, J.M., 1992. Diagenetic reactions in deeply buried sediments of the Japan Sea: a synthesis of interstitial-water chemistry results from Legs 127 and 128. *In* Tamaki, K., Suyehiro, K., Allan, J., McWilliams, M., et al., *Proc. ODP, Sci. Results,* 127/128 (Pt. 2): College Station, TX (Ocean Drilling Program), 1261–1274. **doi:10.2973/odp.proc.sr.127128-2.177.1992**

Oba, T., Kato, M., Kitazato, H., Koizumi, I., Omura, A., Sakai, T., and Takayama, T., 1991. Paleoenvironmental changes in the Japan Sea during the last 85,000 years. *Paleoceanography,* 6(4):499–518. **doi:10.1029/91PA00560**

Pribnow, D., Kinoshita, M., and Stein, C., 2000. *Thermal Data Collection and Heat Flow Recalculations for Ocean Drilling Program Legs 101–180:* Hanover, Germany (Inst. Joint Geosci. Res., Inst. Geowiss. Gemeinschaftsauf. [GGA]). **http://www-odp.tamu.edu/publications/heatflow/ODPReprt.pdf**

Satoguchi, Y., and Nagahashi, Y., 2012. Tephrostratigraphy of the Pliocene to middle Pleistocene series in Honshu and Kyushu Islands, Japan. *Isl. Arc,* 21(3):149–169. **doi:10.1111/j.1440-1738.2012.00816.x**

Schrag, D.P., Hampt, G., and Murray, D.W., 1996. Pore fluid constraints on the temperature and oxygen isotopic composition of the glacial ocean. *Science,* 272(5270):1930–1932. **doi:10.1126/science.272.5270.1930**

Shumway, G., 1958. Sound velocity vs. temperature in water-saturated sediments. *Geophysics,* 23(3):494–505. **doi:10.1190/1.1438495**

Sudo, H., 1986. A note on the Japan Sea Proper Water. *Prog. Oceanogr.,* 17(3–4):313–336. **doi:10.1016/0079-6611(86)90052-2**

Tada, R., 1994. Paleoceanographic evolution of the Japan Sea. *Palaeogeogr., Palaeoclimatol., Palaeoecol.,* 108(3–4):487–508. **doi:10.1016/0031-0182(94)90248-8**

Tada, R., and Iijima, A., 1992. Lithostratigraphy and compositional variation of Neogene hemipelagic sediments in the Japan Sea. *In* Tamaki, K., Suyehiro, K., Allan, J., McWilliams, M., et al., *Proc. ODP, Sci. Results,* 127/128 (Pt. 2): College Station, TX (Ocean Drilling Program), 1229–1260. **doi:10.2973/odp.proc.sr.127128-2.188.1992**

Tada, R., Koizumi, I., Cramp, A., and Rahman, A., 1992. Correlation of dark and light layers, and the origin of their cyclicity in the Quaternary sediments from the Japan Sea. *In* Pisciotto, K.A., Ingle, J.C., Jr., von Breymann, M.T., Barron, J., et al., *Proc. ODP, Sci. Results,* 127/128 (Pt. 1): College Station, TX (Ocean Drilling Program), 577–601. **doi:10.2973/odp.proc.sr.127128-1.160.1992**

Tada, R., Murray, R.W., Alvarez Zarikian, C.A., Anderson, W.T., Jr., Bassetti, M.-A., Brace, B.J., Clemens, S.C., da Costa Gurgel, M.H., Dickens, G.R., Dunlea, A.G., Gallagher, S.J., Giosan, L., Henderson, A.C.G., Holbourn, A.E., Ikehara, K., Irino, T., Itaki, T., Karasuda, A., Kinsley, C.W., Kubota, Y., Lee, G.S., Lee, K.E., Lofi, J., Lopes, C.I.C.D., Peterson, L.C., Saavedra-Pellitero, M., Sagawa, T., Singh, R.K., Sugisaki, S., Toucanne, S., Wan, S., Xuan, C., Zheng, H., and Ziegler, M., 2015a. Expedition 346 summary. *In* Tada, R., Murray, R.W., Alvarez Zarikian, C.A., and the Expedition 346 Scientists, *Proc. IODP,* 346: College Station, TX (Integrated Ocean Drilling Program). **doi:10.2204/iodp.proc.346.101.2015**

Tada, R., Murray, R.W., Alvarez Zarikian, C.A., Anderson, W.T., Jr, Bassetti, M.-A., Brace, B.J., Clemens, S.C., Dickens, G.R., Dunlea, A.G., Gallagher, S.J., Giosan, L., da Costa Gurgel, M.H., Henderson, A.C.G., Holbourn, A.E., Ikehara, K., Irino, T., Itaki, T., Karasuda, A., Kinsley, C.W., Kubota, Y., Lee, G.S., Lee, K.E., Lofi, J., Lopes, C.I.C.D., Peterson, L.C., Saavedra-Pellitero, M., Sagawa, T., Singh, R.K., Sugisaki, S., Toucanne, S., Wan, S., Xuan, C., Zheng, H., and Ziegler, M., 2015b. Methods. *In* Tada, R., Murray, R.W., Alvarez Zarikian, C.A., and the Expedition 346 Scientists, *Proc. IODP,* 346: College Station, TX (Integrated Ocean Drilling Program). **doi:10.2204/iodp.proc.346.102.2015**

Tada, R., Murray, R.W., Alvarez Zarikian, C.A., Anderson, W.T., Jr., Bassetti, M.-A., Brace, B.J., Clemens, S.C., da Costa Gurgel, M.H., Dickens, G.R., Dunlea, A.G., Gallagher, S.J., Giosan, L., Henderson, A.C.G., Holbourn, A.E., Ikehara, K., Irino, T., Itaki, T., Karasuda, A., Kinsley, C.W., Kubota, Y., Lee, G.S., Lee, K.E., Lofi, J., Lopes, C.I.C.D., Peterson, L.C., Saavedra-Pellitero, M., Sagawa, T., Singh, R.K., Sugisaki, S., Toucanne, S., Wan, S., Xuan, C., Zheng, H., and Ziegler, M., 2015c. Site U1422. *In* Tada, R., Murray, R.W., Alvarez Zarikian, C.A., and the Expedition 346 Scientists, *Proc. IODP,* 346: College Station, TX (Integrated Ocean Drilling Program). **doi:10.2204/iodp.proc.346.103.2015**

Talley, L.D., Lobanov, V., Ponomarev, V., Salyuk, A., Tishchenko, P., Zhabin, I., and Riser, S., 2003. Deep convection and brine rejection in the Japan Sea. *Geophys. Res. Lett.,* 30(4):1159. **doi:10.1029/2002GL016451**

Tamaki, K., Pisciotto, K., Allan, J., et al., 1990. *Proc. ODP, Init. Repts.,* 127: College Station, TX (Ocean Drilling Program). **doi:10.2973/odp.proc.ir.127.1990**

Tamaki, K., Suyehiro, K., Allan, J., Ingle, J.C., Jr., and Pisciotto, K.A., 1992. Tectonic synthesis and implications of Japan Sea ODP drilling. *In* Tamaki, K., Suyehiro, K., Allan, J., McWilliams, M., et al., *Proc. ODP, Sci. Results,* 127/128 (Pt. 2): College Station, TX (Ocean Drilling Program), 1333–1348. **doi:10.2973/odp.proc.sr.127128-2.240.1992**

van Geldern, R., Hayashi, T., Böttcher, M.E., Mottl, M.J., Barth, J.A.C., and Stadler, S., 2013. Stable isotope geochemistry of pore waters and marine sediments from the New Jersey shelf: methane formation and fluid origin. *Geosphere,* 9(1):96–112. **doi:10.1130/GES00859.1**

Wilkin, R.T., and Arthur, M.A., 2001. Variations in pyrite texture, sulphur isotope composition, and iron systematics in the Black Sea: evidence for the late Pleistocene to Holocene excursions of the O_2-H_2S redox transition. *Geochim. Cosmochim. Acta,* 65(9):1399–1416. **doi:10.1016/S0016-7037(01)00552-X**

Wilkin, R.T., Arthur, M.A., and Dean, W.E., 1997. History of water-column anoxia in the Black Sea indicated by pyrite framboid size distributions. *Earth Planet. Sci. Lett.,* 148(3–4):517–525. **doi:10.1016/S0012-821X(97)00053-8**

Wilkin, R.T., Barnes, H.L., and Brantley, S.L., 1996. The size distribution of framboidal pyrite in modern sediments: an indicator of redox conditions. *Geochim. Cosmochim. Acta,* 60(20):3897–3912. **doi:10.1016/0016-7037(96)00209-8**

Xuan, C., and Channell, J.E.T., 2009. UPmag: MATLAB software for viewing and processing U channel or other pass-through paleomagnetic data. *Geochem., Geophys., Geosyst.,* 10(10):Q10Y07. **doi:10.1029/2009GC002584**

Yoon, J.-H., and Kim, Y.-J., 2009. Review on the seasonal variation of the surface circulation in the Japan/East Sea. *J. Mar. Syst.,* 78(2):226–236. **doi:10.1016/j.jmarsys.2009.03.003**

Publication: 28 March 2015
MS 346-104

Figure F1. Bathymetric map of Expedition 346 sites (red circles) in the marginal sea surrounded by the Japanese Islands, the Korean Peninsula, and the Eurasian continent and the East China Sea. Sites previously drilled by the Deep Sea Drilling Project (DSDP) and Ocean Drilling Program (ODP) (white circles) are also shown. Also illustrated are surface current systems within and surrounding this marginal sea.

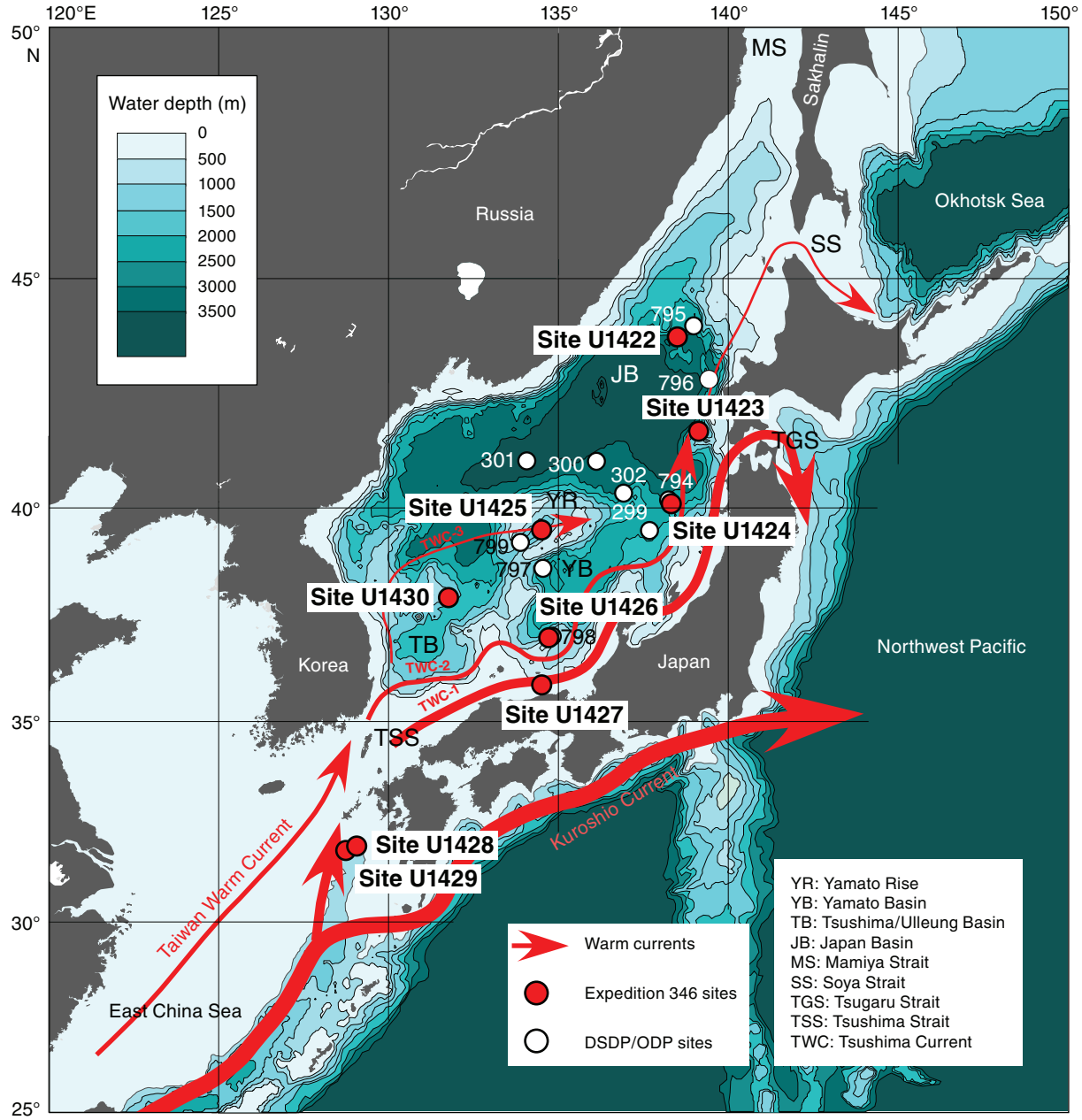

Figure F2. Lithologic summary, Hole U1423A. GRA = gamma ray attenuation.

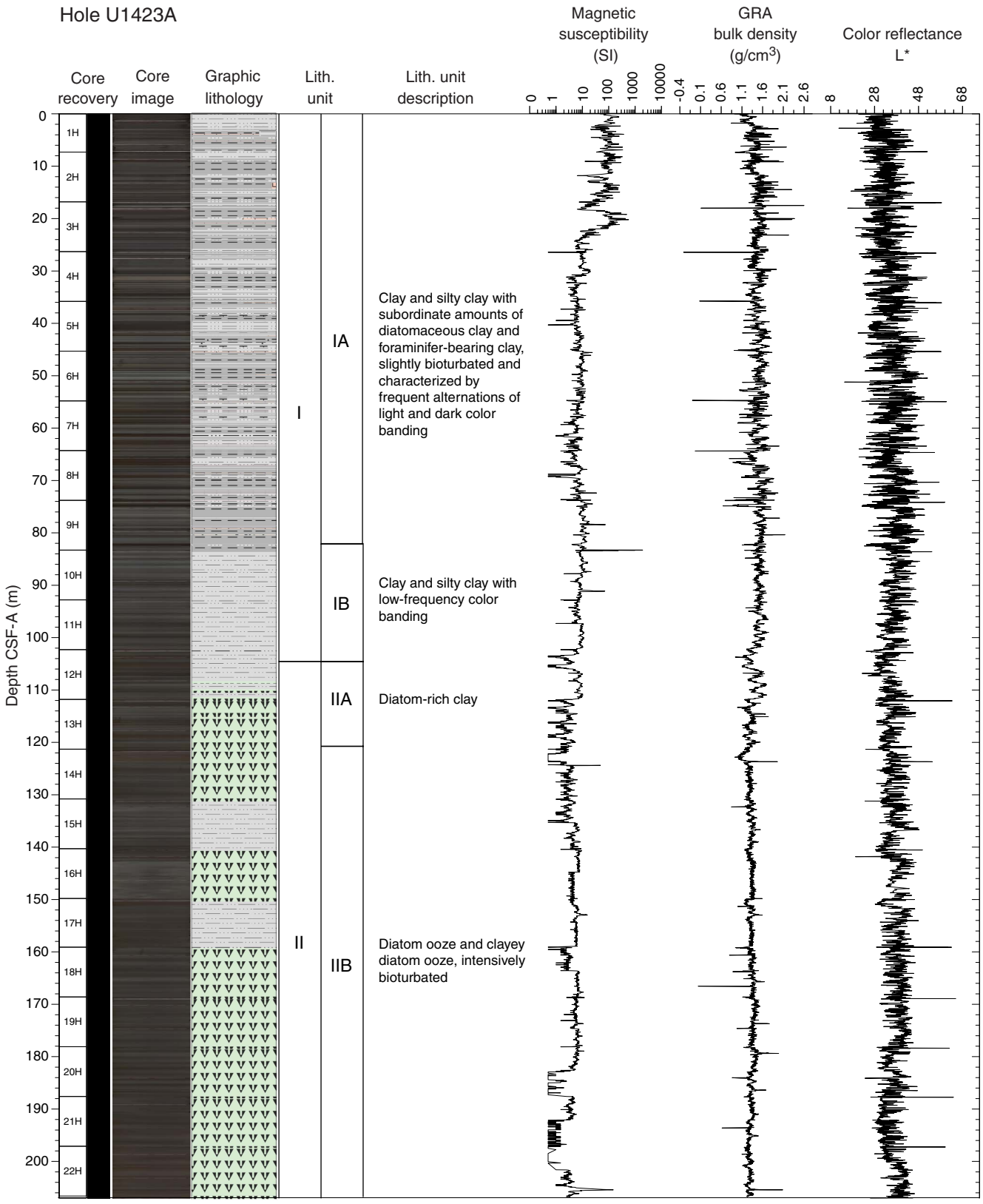

Figure F3. Lithologic summary, Hole U1423B. GRA = gamma ray attenuation.

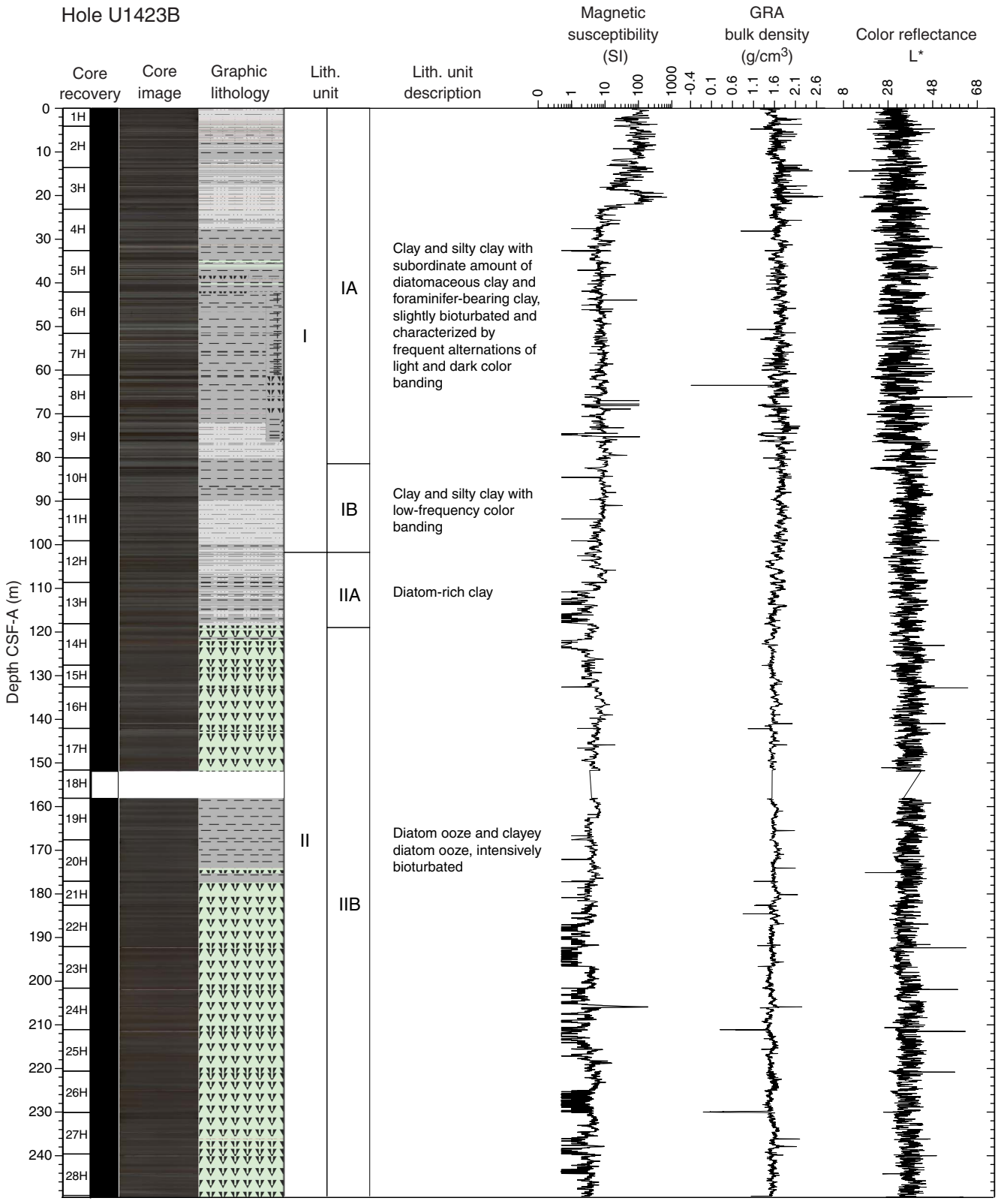

Figure F4. Lithologic summary, Hole U1423C. GRA = gamma ray attenuation.

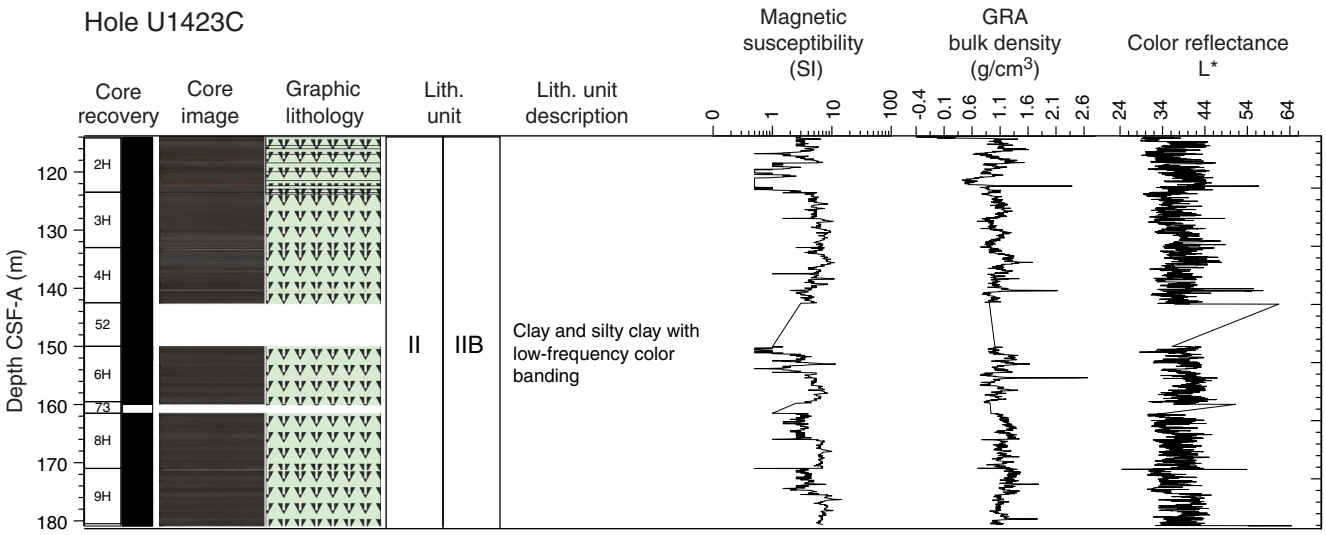

Figure F5. Hole-to-hole lithostratigraphic correlation, Site U1423.

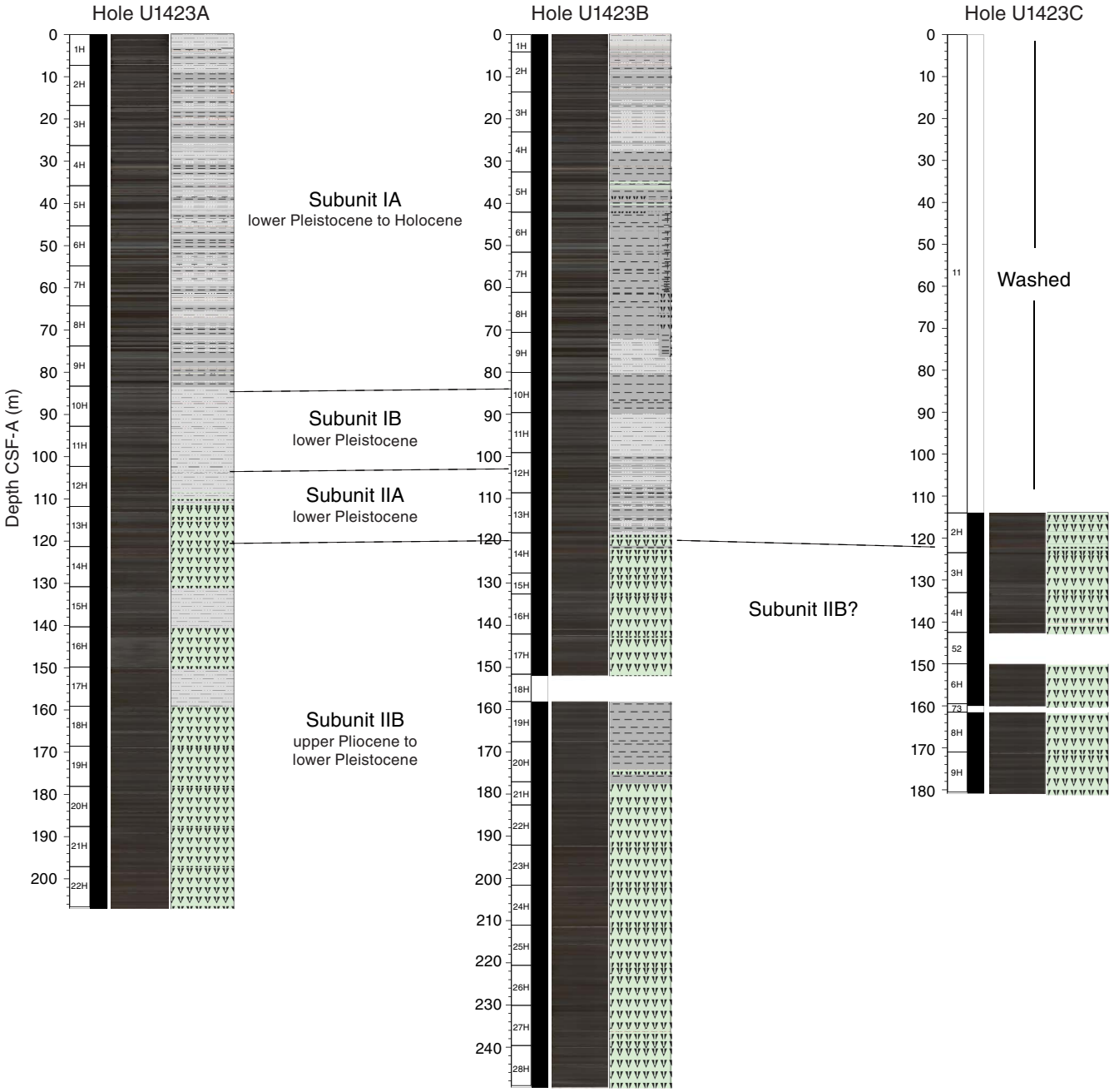

Figure F6. Number of visible tephra layers (>0.5 cm thick) and their total thickness in each core, in Hole U1423A.

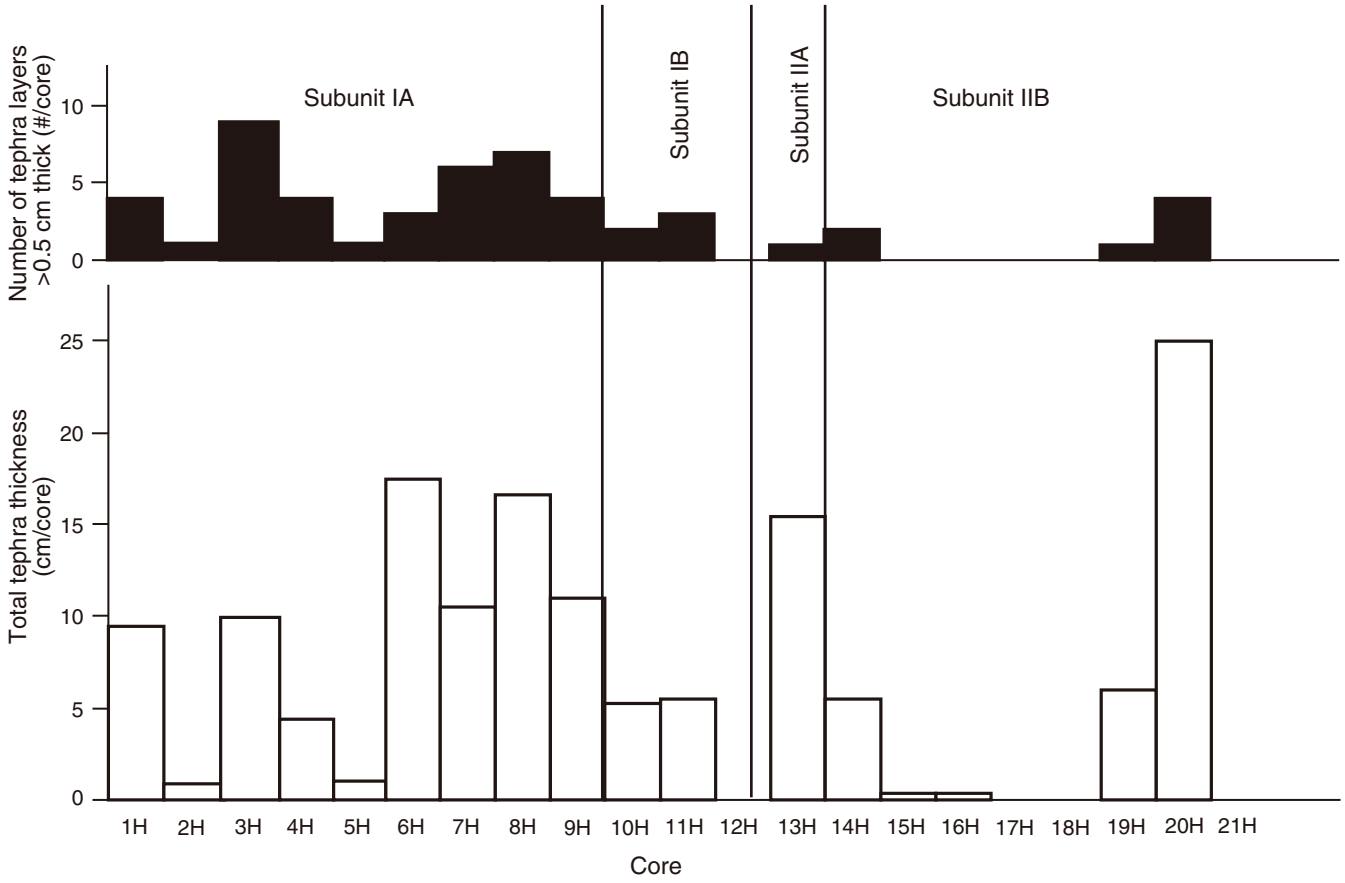

Figure F7. Variation of XRD peak intensities of identified minerals with depth, Hole U1423A.

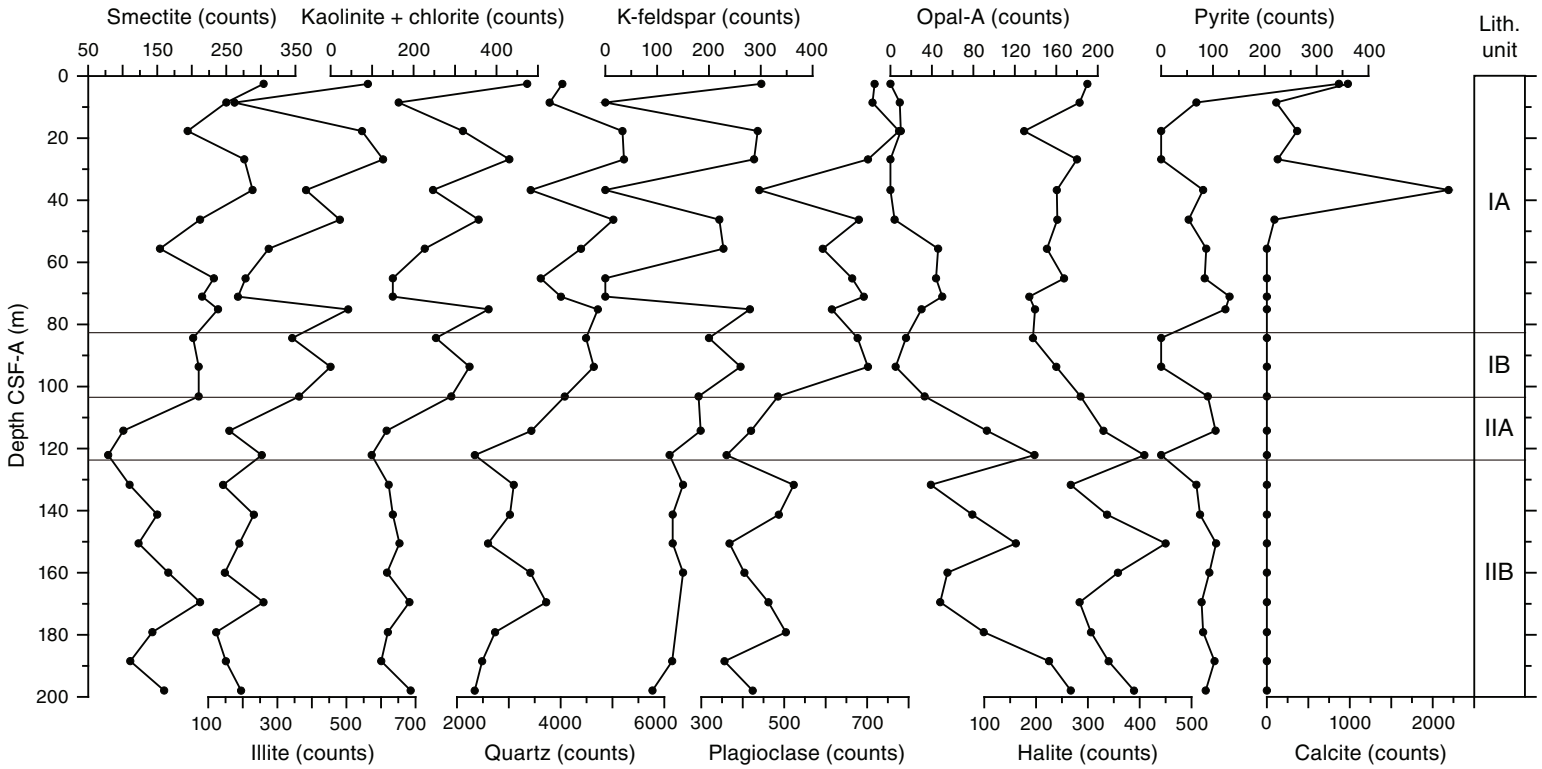

Figure F8. Photographs representative of Subunit IA in Holes U1423A and U1423B. Note enhanced color contrast to highlight sedimentary structures.

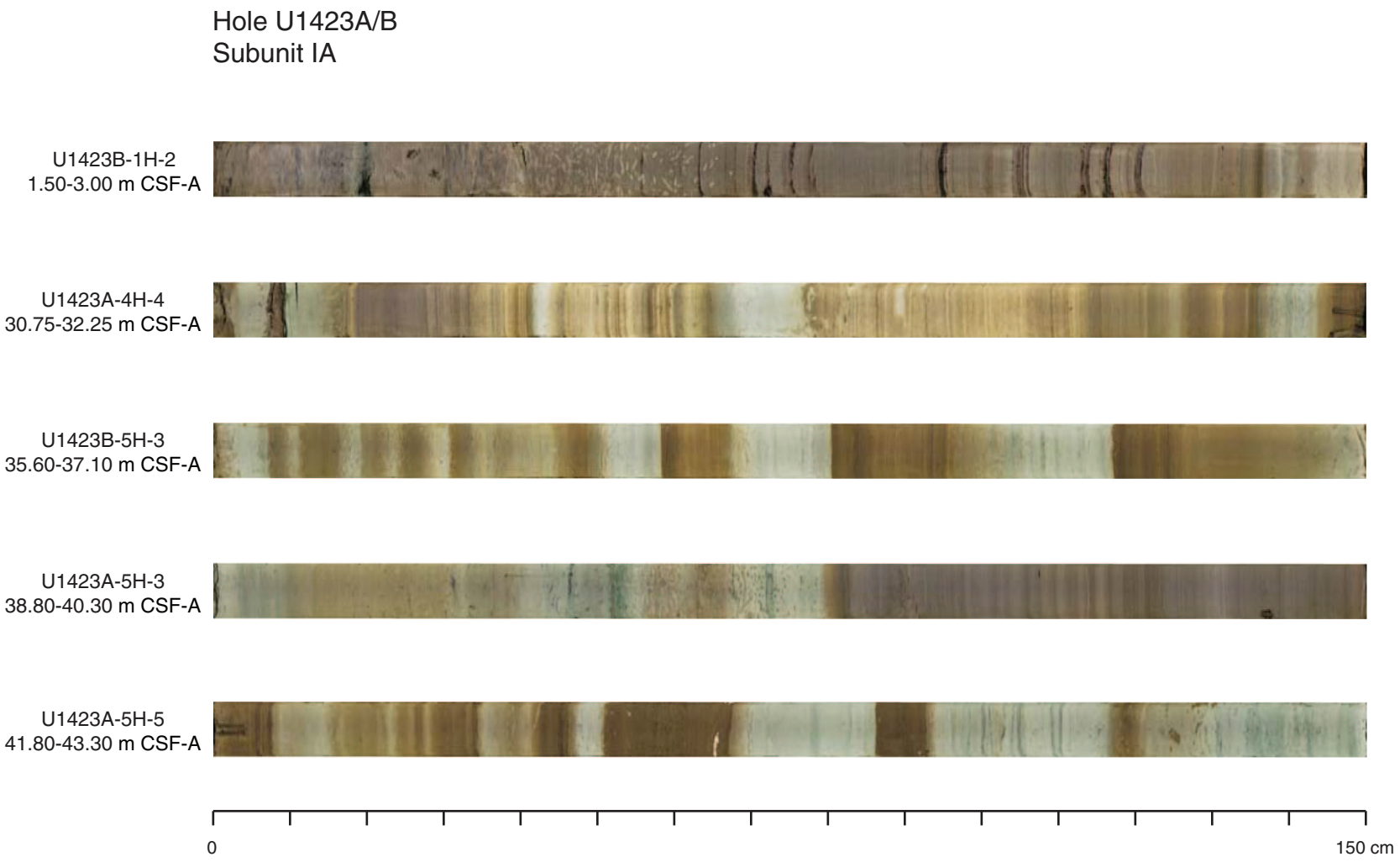

Figure F9. Foraminifer-rich nannofossil clay at 93 cm in laminated dark brown interval (346-U1423A-4H-4, 85–105 cm).

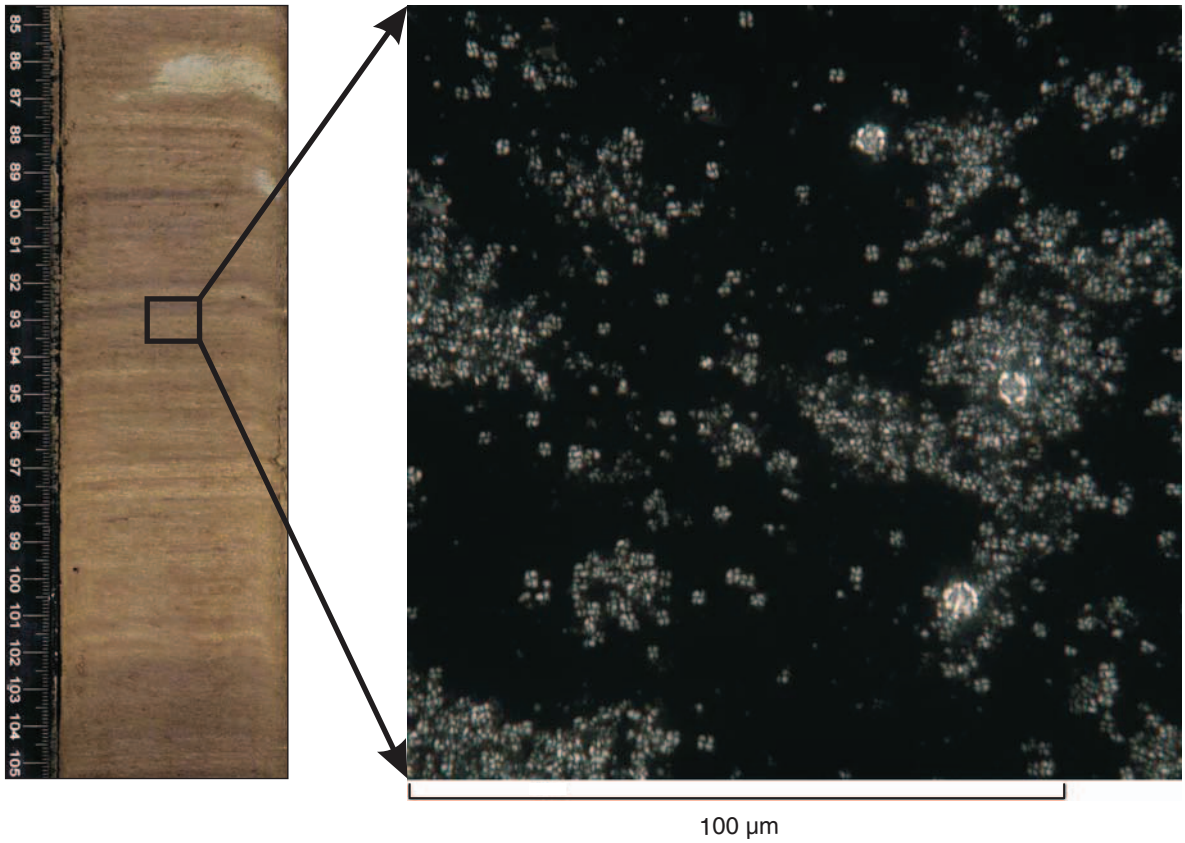

Figure F10. Photographs representative of Subunit IB in Holes U1423A and U1423B. Note enhanced color contrast to highlight sedimentary structures.

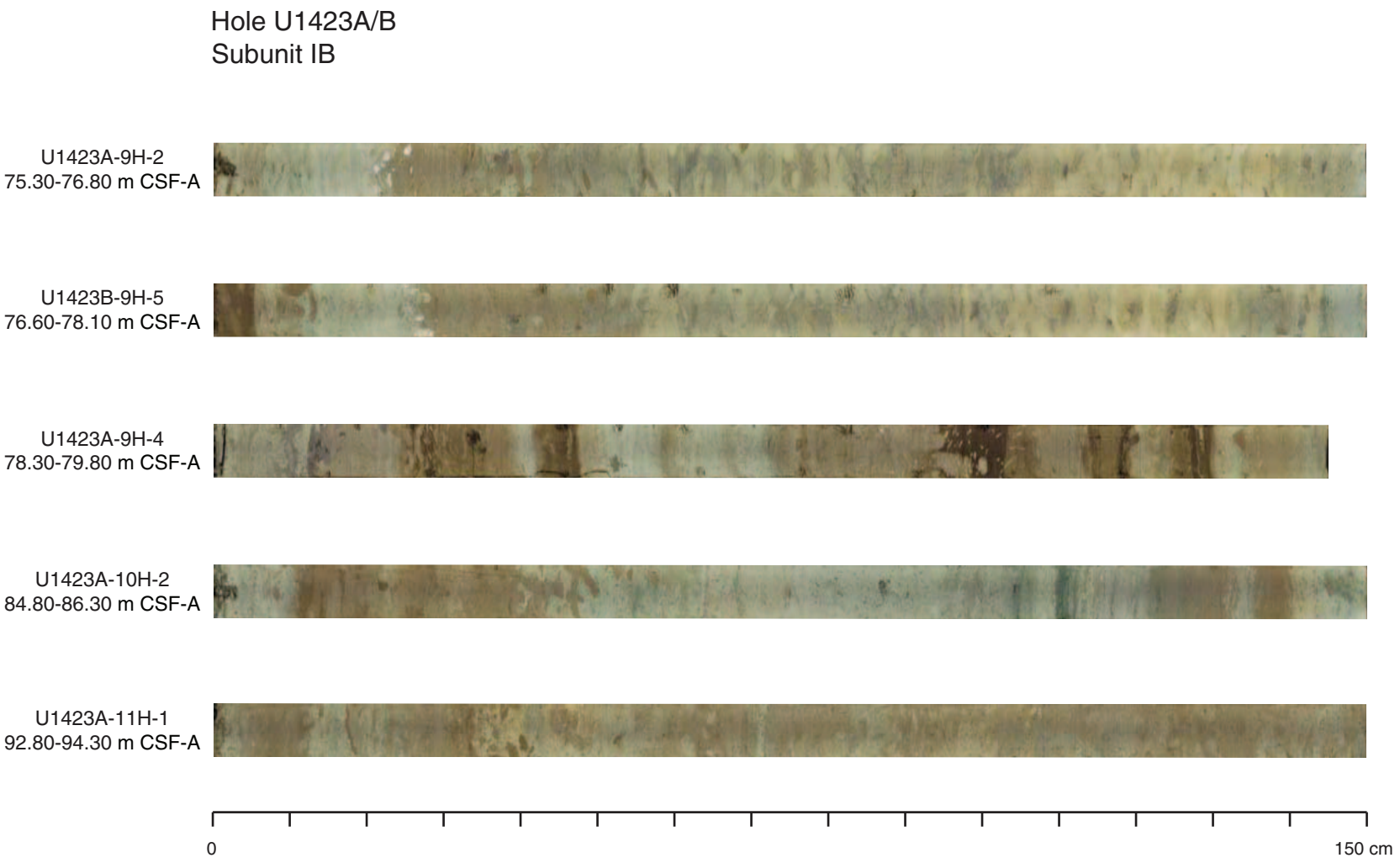

Figure F11. Photographs representative of Subunit IIA in Hole U1423A. Note enhanced color contrast to highlight sedimentary structures.

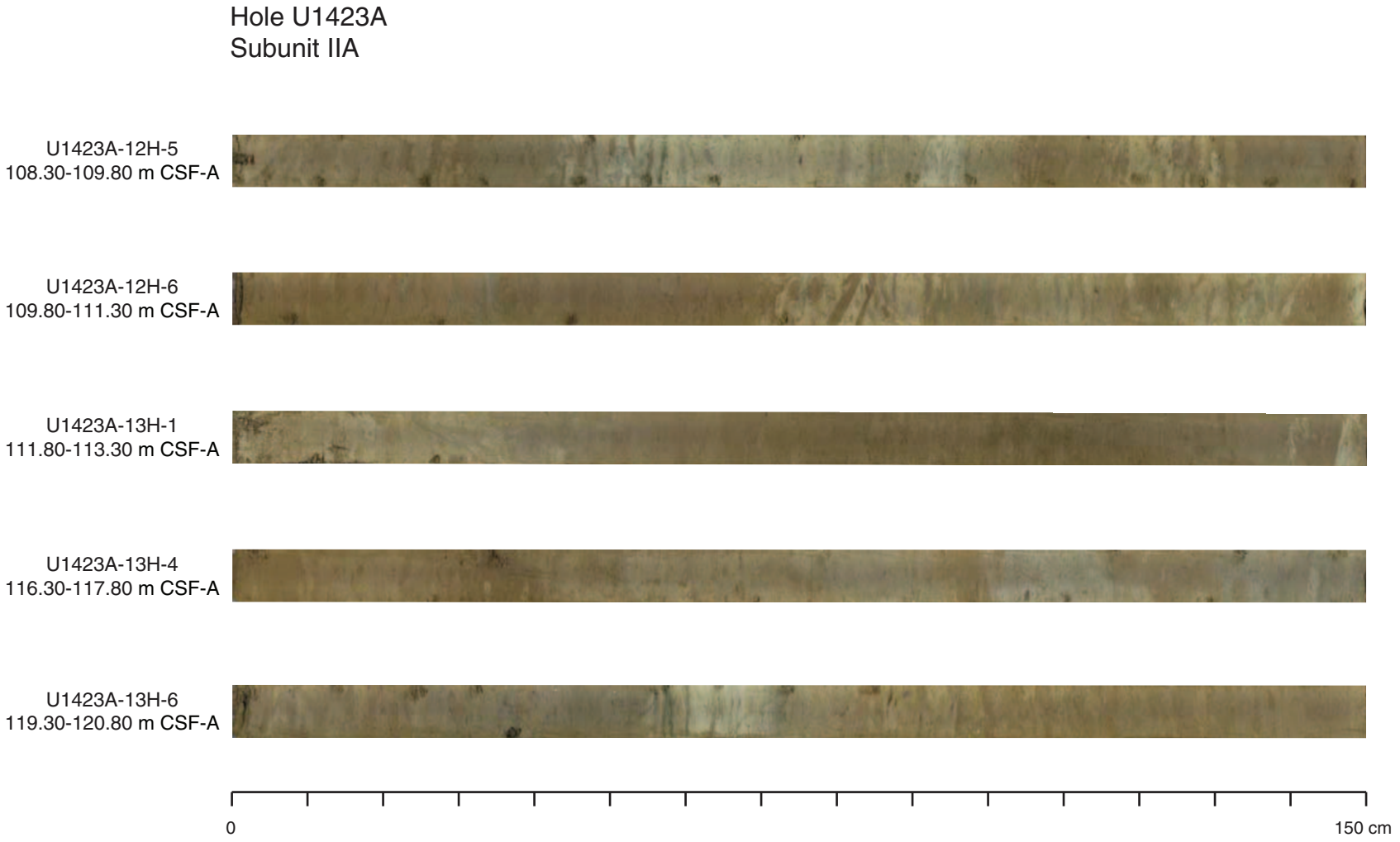

Figure F12. Photographs representative of Subunit IIB in Hole U1423A. Note enhanced color contrast to highlight sedimentary structures.

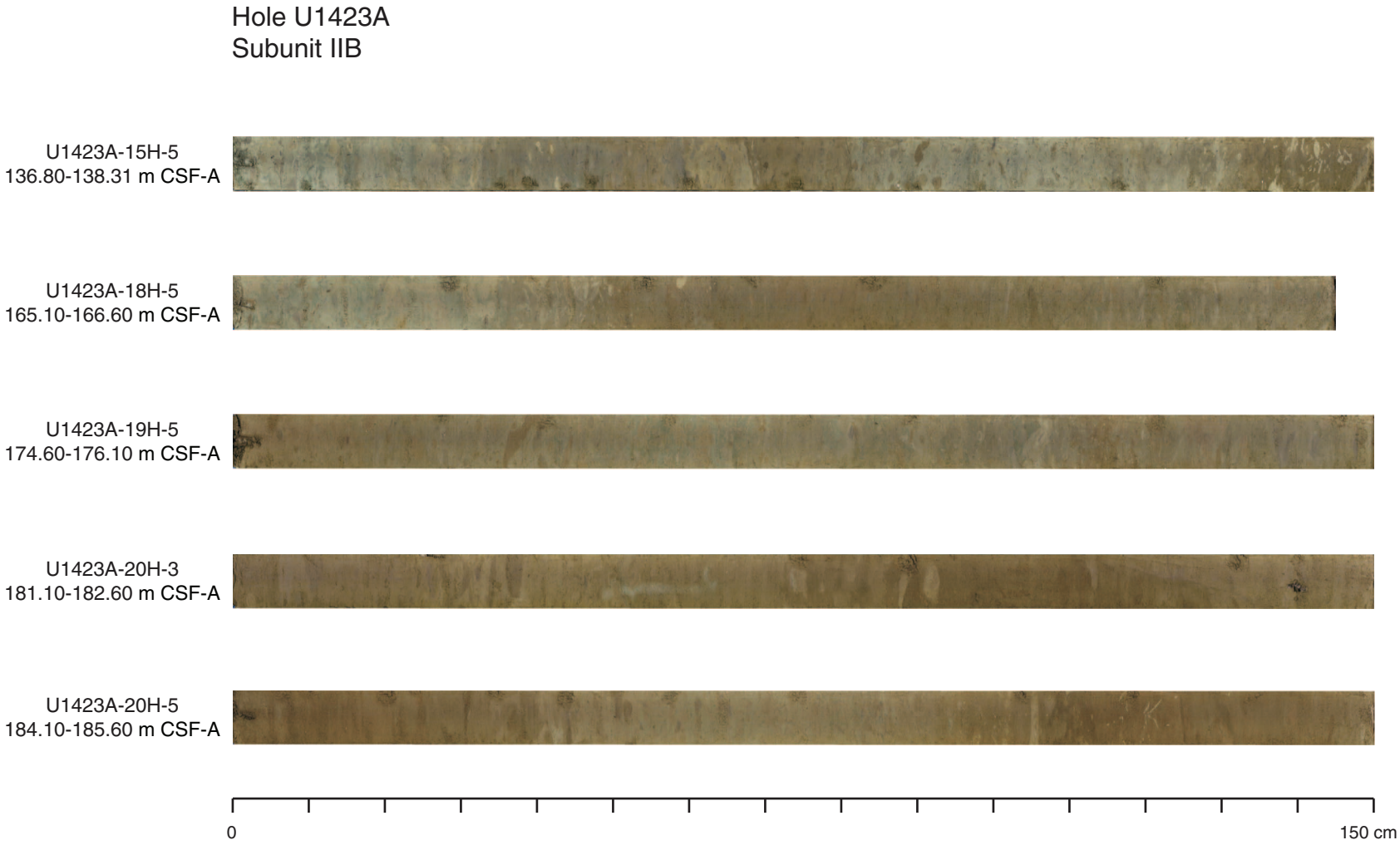

Figure F13. Normal graded tephra layer observed in hemipelagic diatom ooze composed by bubble-junction type glass shards (interval 346-U1423A-20H-6, 70–98 cm). v.f.s. = very fine sand, f.s. = fine sand.

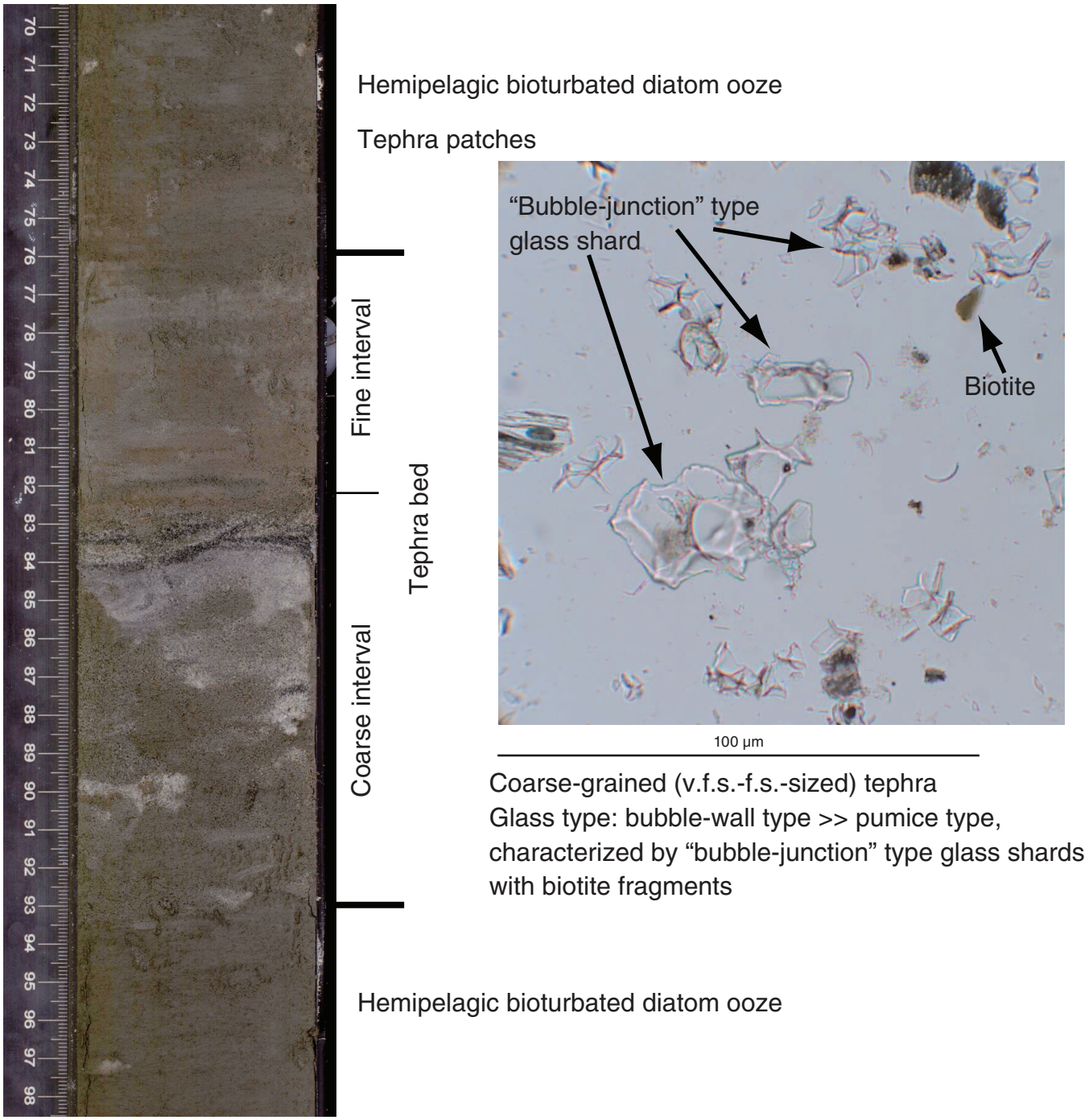

Figure F14. Downhole plots of measured total organic carbon (TOC), opal-A from XRD, and natural gamma radiation (NGR), Holes U1423A and U1423B. The corresponding lithologic units are identified.

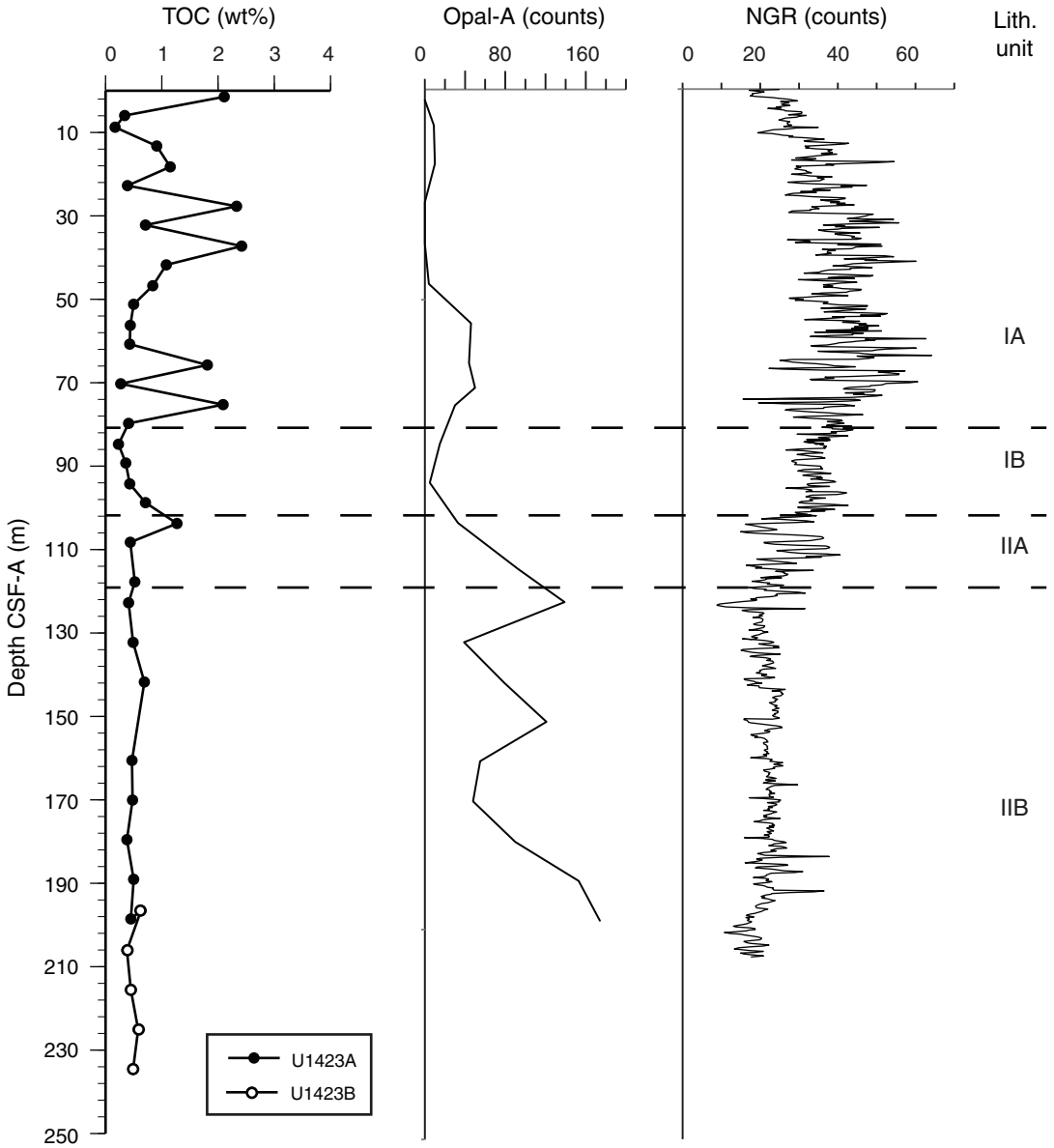

Figure F15. Integrated calcareous and siliceous microfossil biozonation, Site U1423.

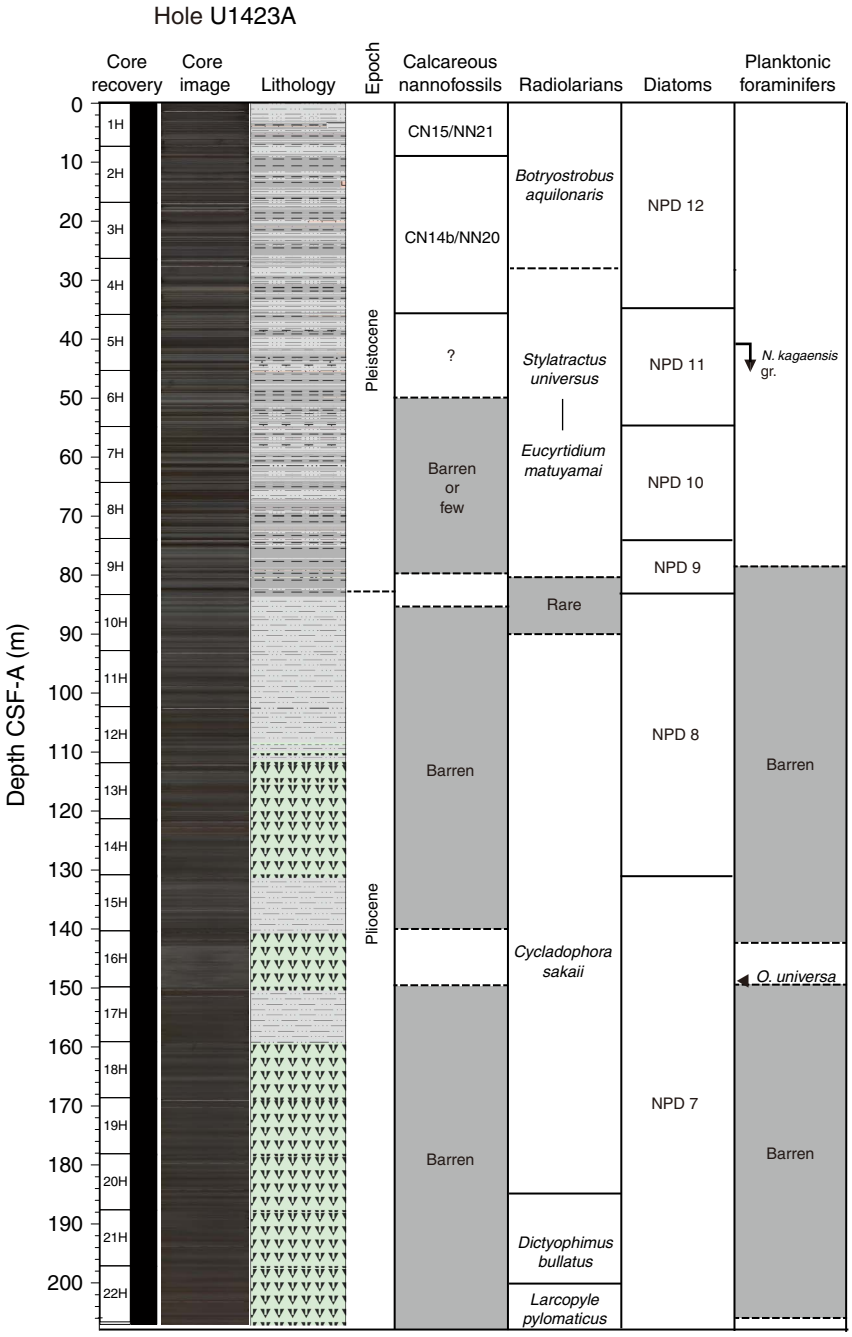

Figure F16. Preliminary age-depth profile and estimated sedimentation rates, Site U1423. LO = last occurrence, FO = first occurrence, RD = rapid decrease, Br = base reentrance.

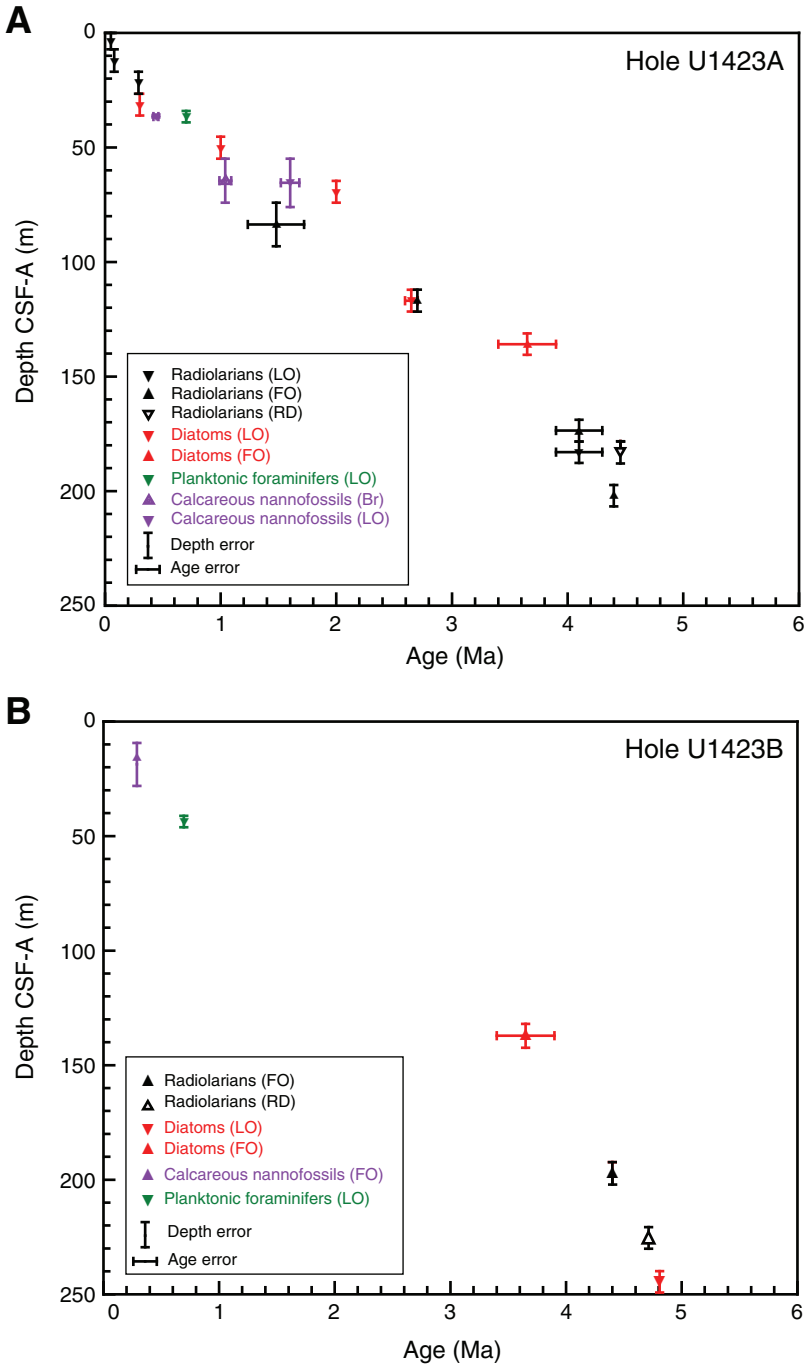

Figure F17. Total radiolarian, calcareous nannofossil, and diatom abundance, as well as relative abundance of *Chaetoceros* spores, Holes U1423A and U1423B. B = barren, R = rare, F = few, C = common, A = abundant, D = dominant.

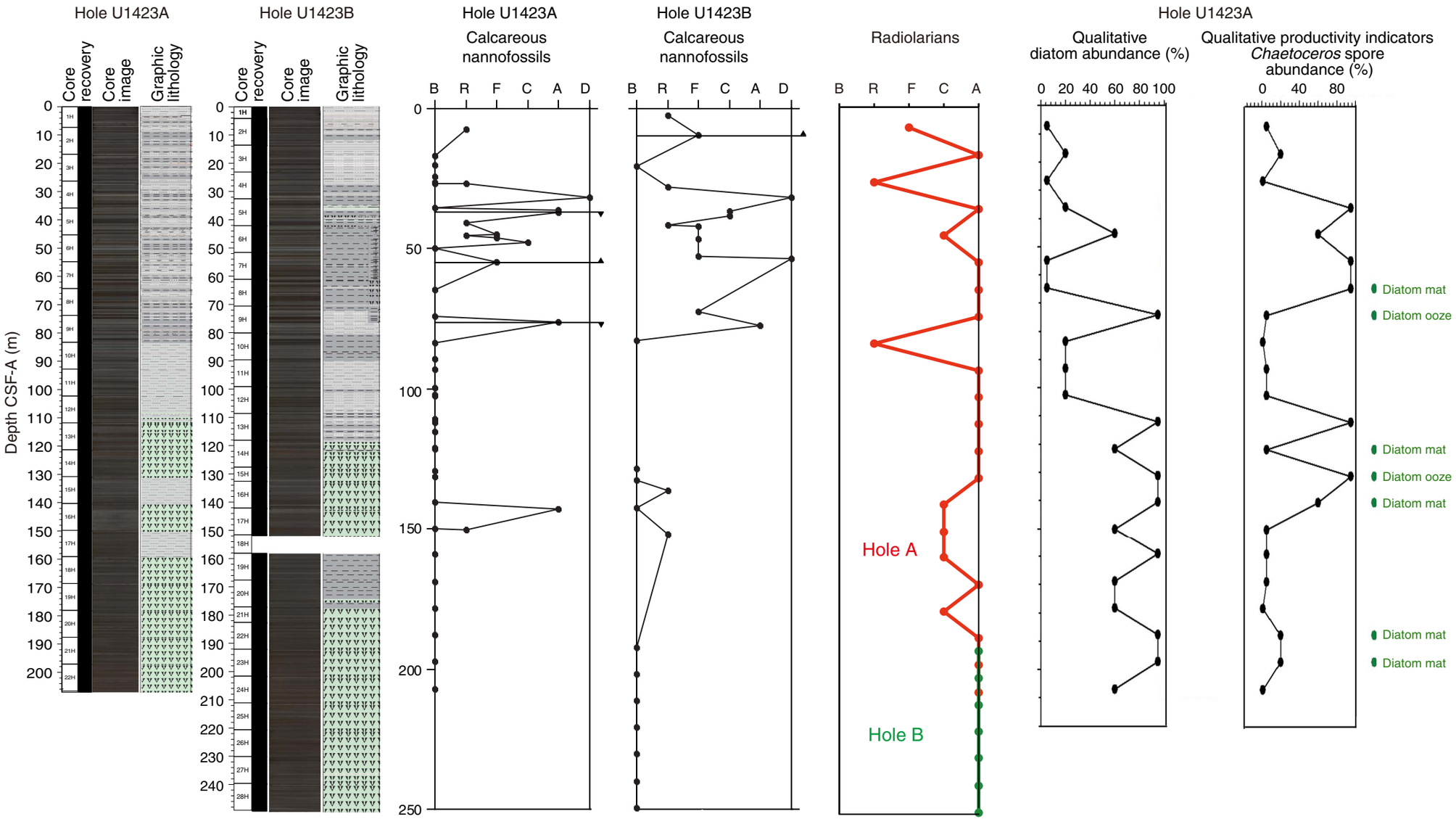

Figure F18. Percentage abundance of planktonic (blue) and benthic (yellow) foraminifers and barren intervals (black), Site U1423. Orange arrows mark horizons with diverse (oxic) benthic assemblages, green arrows mark horizons with abundant *Bolivina pacifica* (dysoxia).

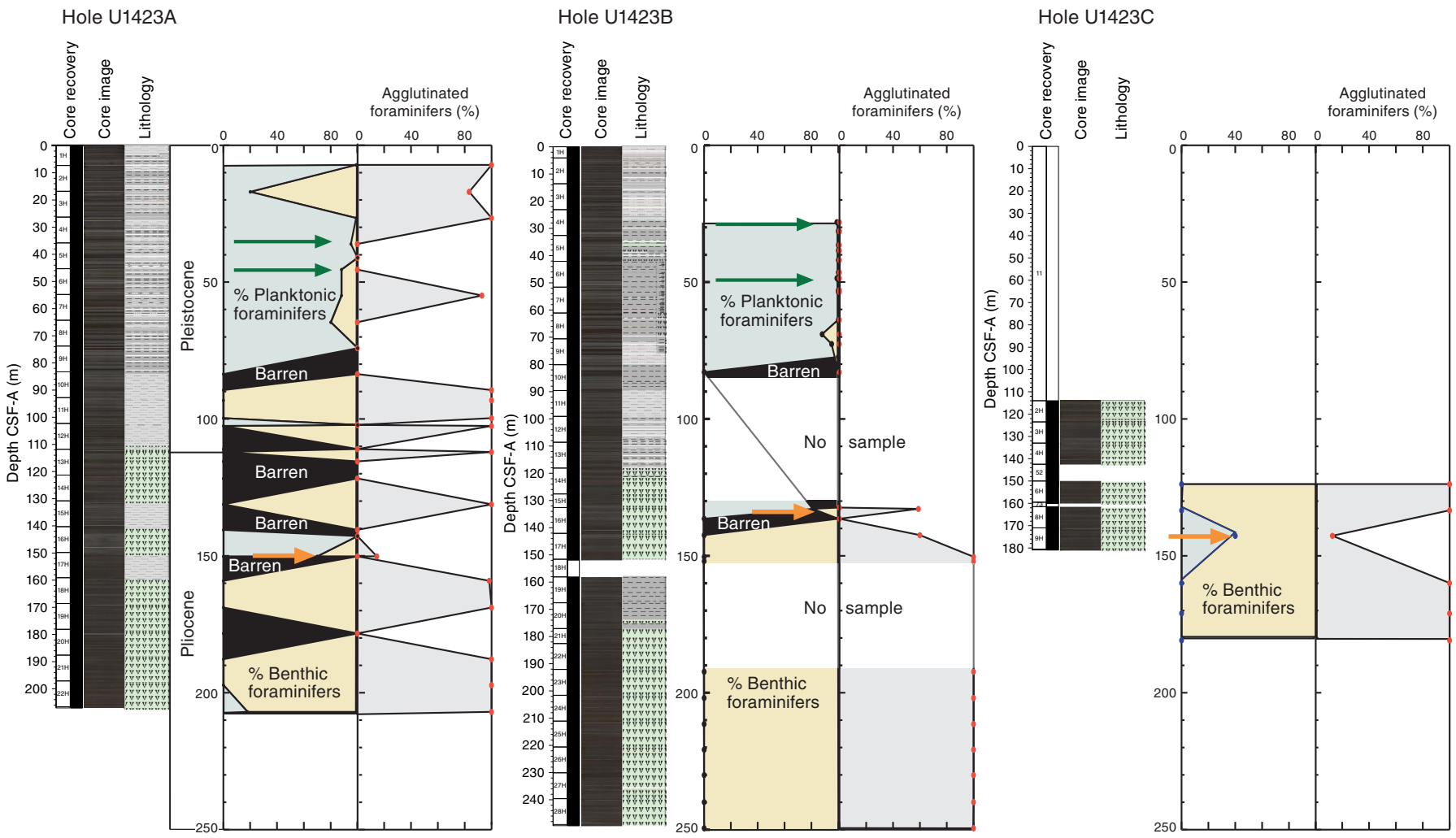

Figure F19. Benthic foraminifers from diverse assemblages indicative of more oxic conditions at the seafloor. Scale bars = 50 µm. **1.** *Lenticulina* sp. (Sample 346-U1423A-16H-CC). **2, 3.** *Bulimina mexicana* (Sample 346-U1423A-16H-CC). **4.** *Hoeglundina elegans* (Sample 346-U1423A-16H-CC). **5.** *Martinotiella communis* (Sample 346-U1423B-15H-CC). **6, 7.** *Oridorsalis umbonatus* (Sample 346-U1423A-16H-CC); (6) spiral view; (7) umbilical view. **8, 9.** *Melonis pompilioides* (Sample 346-U1423A-16H-CC); (8) umbilical view (9) side view. **10.** *Melonis barleeanum* (side view) (Sample 346-U1423A-16H-CC). **11.** *Karreriella* sp. (Sample 346-U1423A-16H-CC). **12.** *Eggerella bradyi* (umbilical view) (Sample 346-U1423A-16H-CC). **13.** *Globobulimina pupoides* (Sample 346-U1423A-16H-CC). **14.** *Globobulimina pacifica* (Sample 346-U1423A-16H-CC). **15.** *Pyrgo murrhina* (umbilical view) (Sample 346-U1423B-15H-CC). **16.** *Gyroidina orbicularis* (Sample 346-U1423A-16H-CC). **17.** *Gyroidella* sp. (Sample 346-U1423A-16H-CC). **18, 19.** *Bolivina quadrilatera;* (18) umbilical view (Sample 346-U1423B-15H-CC); (19) Sample 346-U1423A-16H-CC.

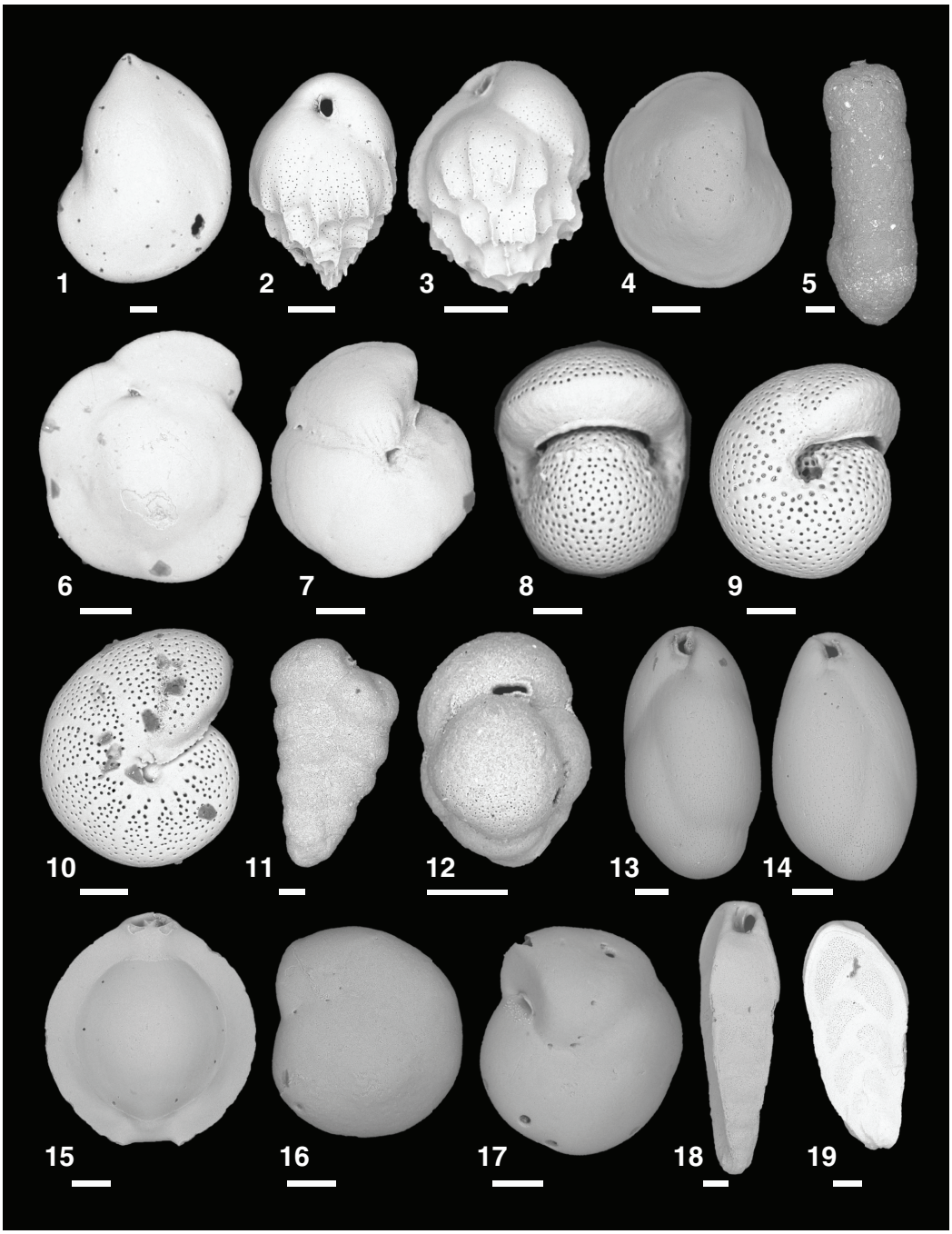

Figure F20. Organically cemented agglutinated foraminifers from Hole U1423A mudline sample. Scale bars = 50 µm. **1, 2, 5.** *Haplophragmoides sphaeriloculum*. **3, 4.** *Paratrochammina challengeri* (spiral view) with detail of wall structure. **6, 7.** *Cribrostomoides subglobosus* with detail of aperture. **8–10.** *Miliammina echigoensis;* (9) stained specimen, which exhibits much better preservation than unstained specimens (8) and (10). **11, 12.** *Jacullela* cf. *acuta* with detail of wall structure. **13, 14.** *Hyperammina elongata* with detail of initial portion. **15, 16.** *Rhabdammina* sp. with detail of wall structure. **17.** *Paratrochammina challengeri* (umbilical view). **18.** *Haplophragmoides sphaeriloculum*. **19.** *Cribrostomoides subglobosus*.

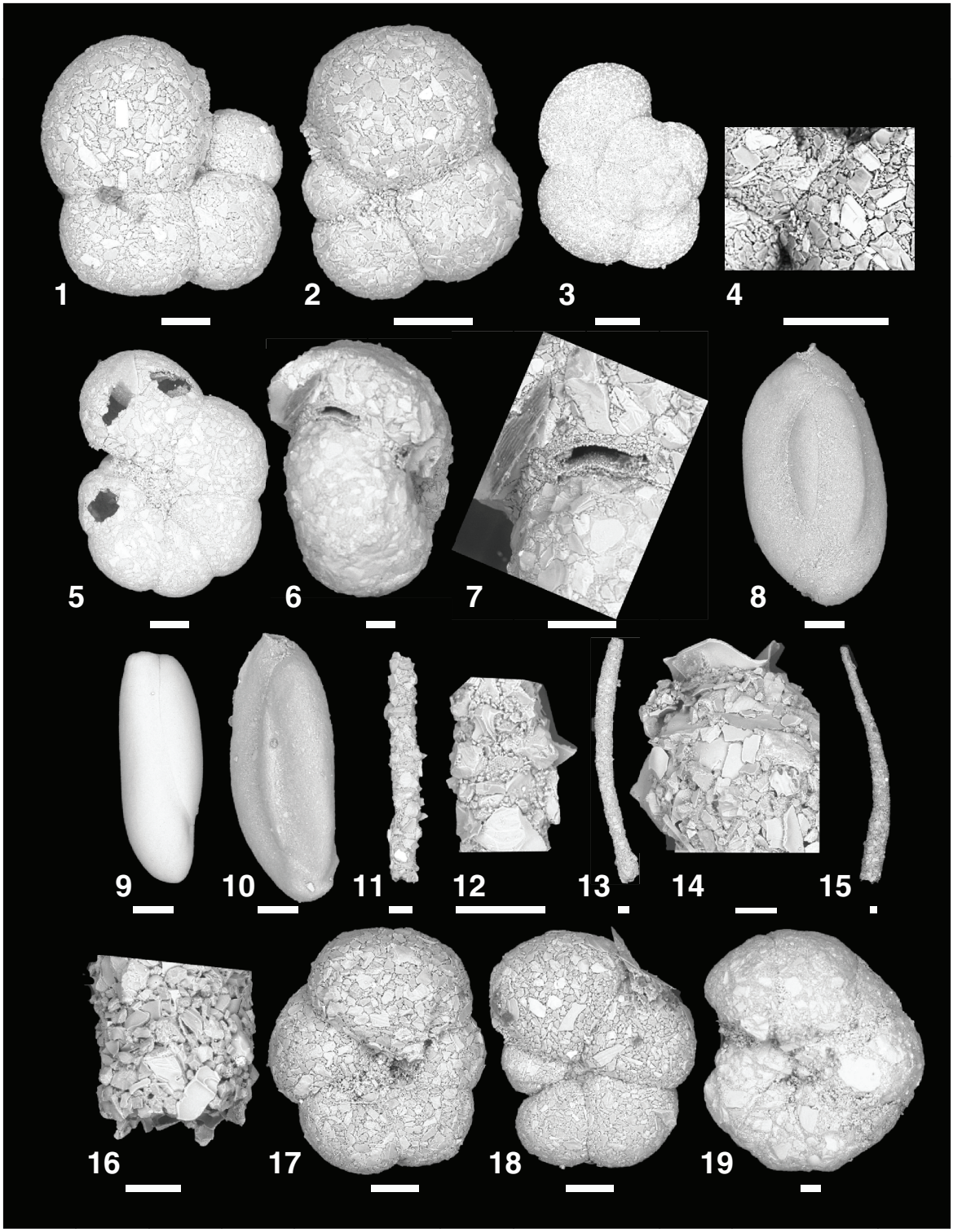

Figure F21. Ostracods (Sample 346-U1423A-16H-CC). **A, B.** *Henryhowella* cf. *H. circumdentata* (Brady, 1880). **C.** *Krithe* sp. 1. **D, E.** *Krithe* sp. 2; (E) detail of a sieve pore. **F.** *Legitimocythere* sp.

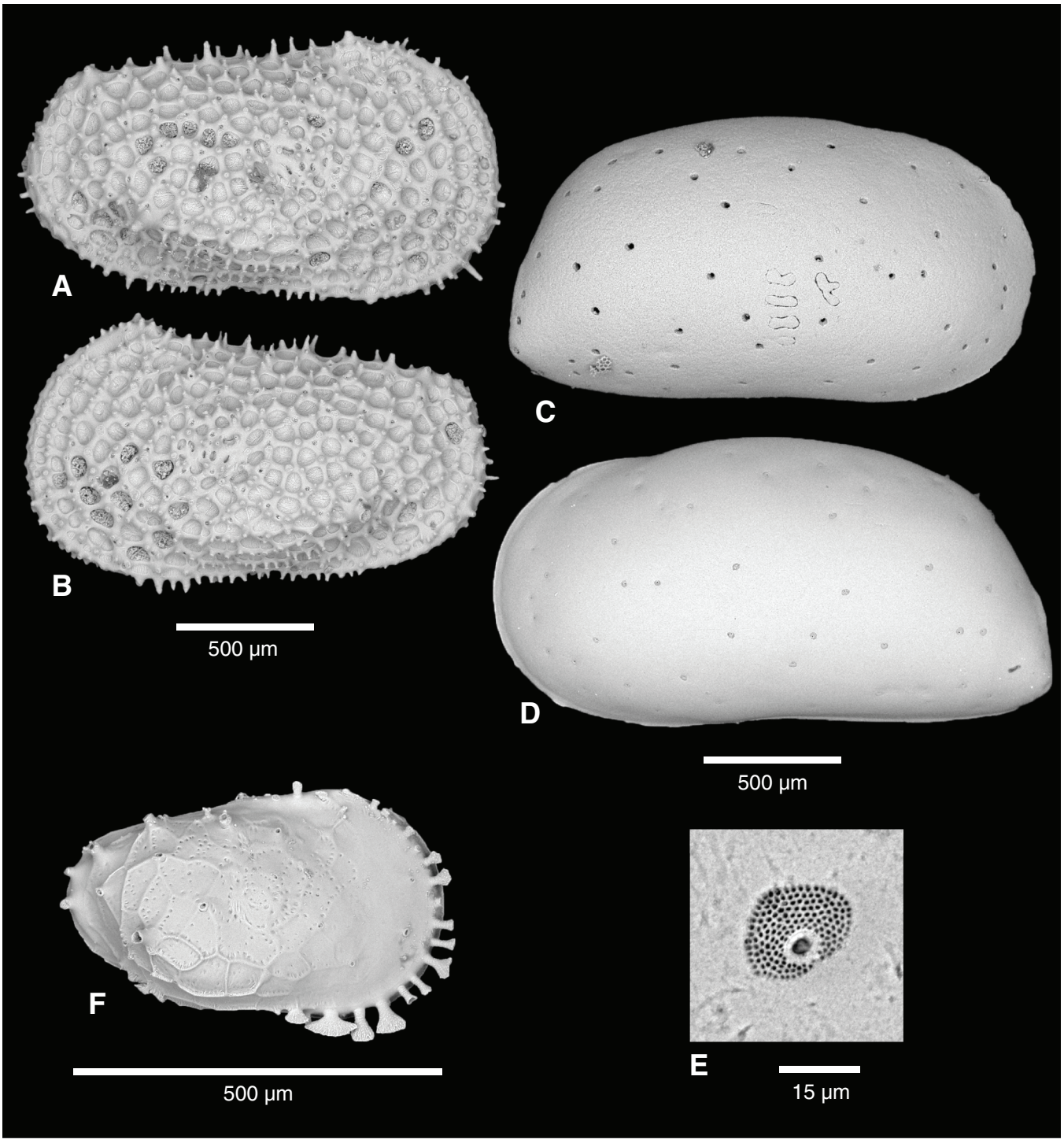

Figure F22. Solid-phase contents of discrete sediment samples, Site U1423. TC = total carbon, TOC = total organic carbon, TN = total nitrogen.

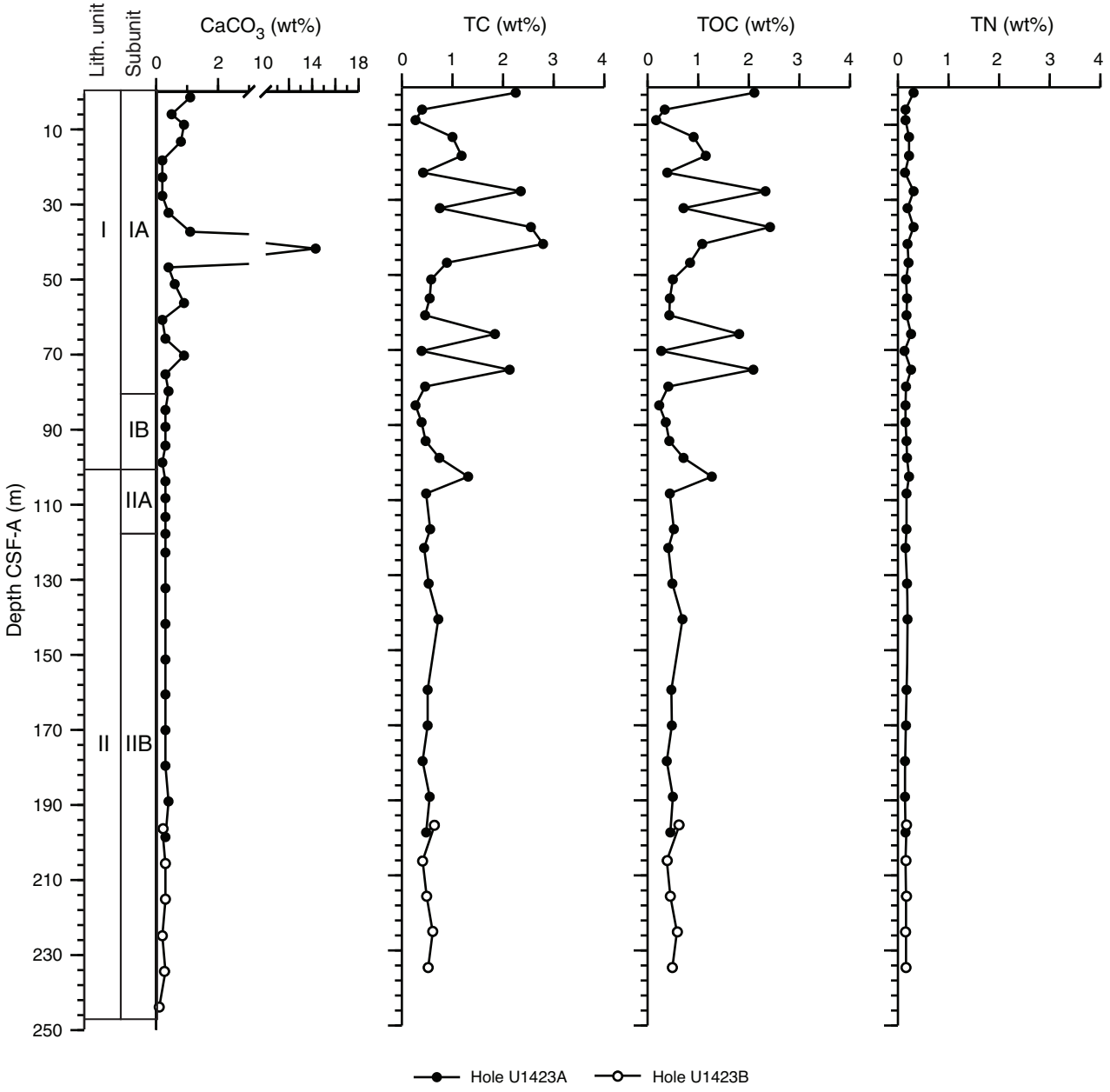

Figure F23. Dissolved iron and manganese profiles, Site U1423.

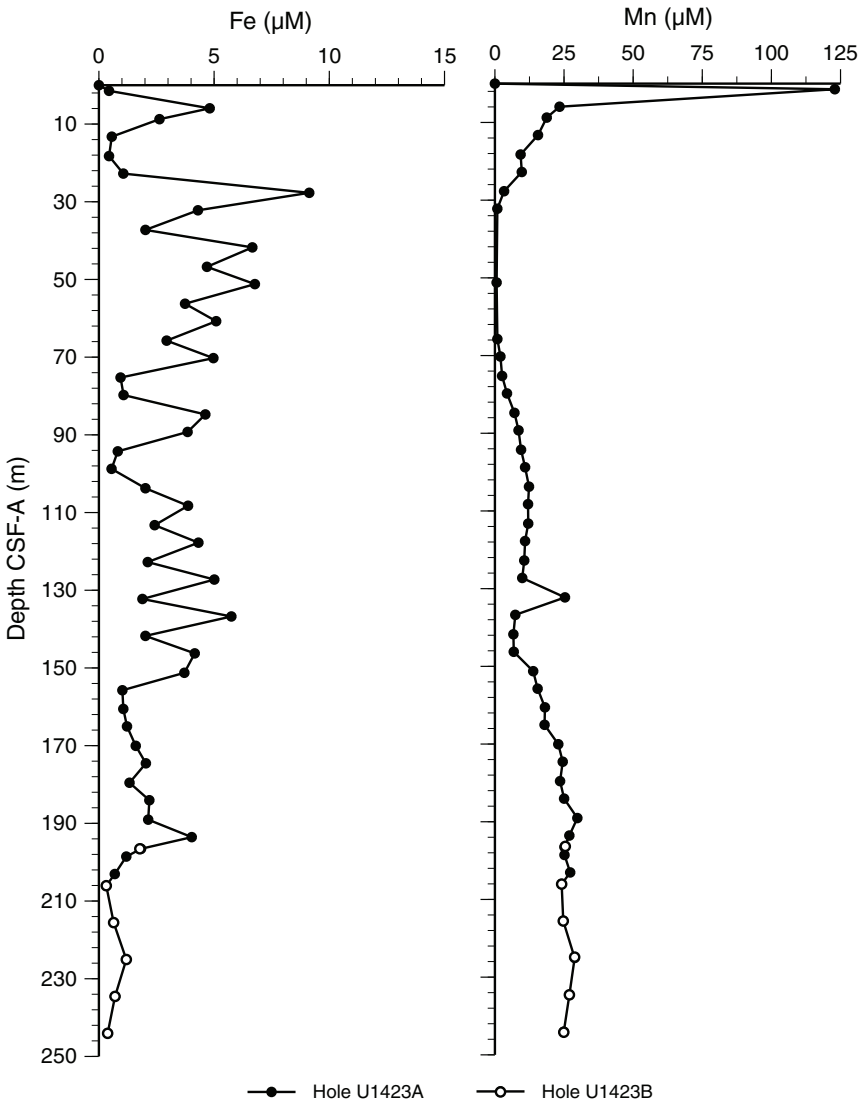

Figure F24. Dissolved alkalinity, ammonium, and phosphate profiles, Site U1423.

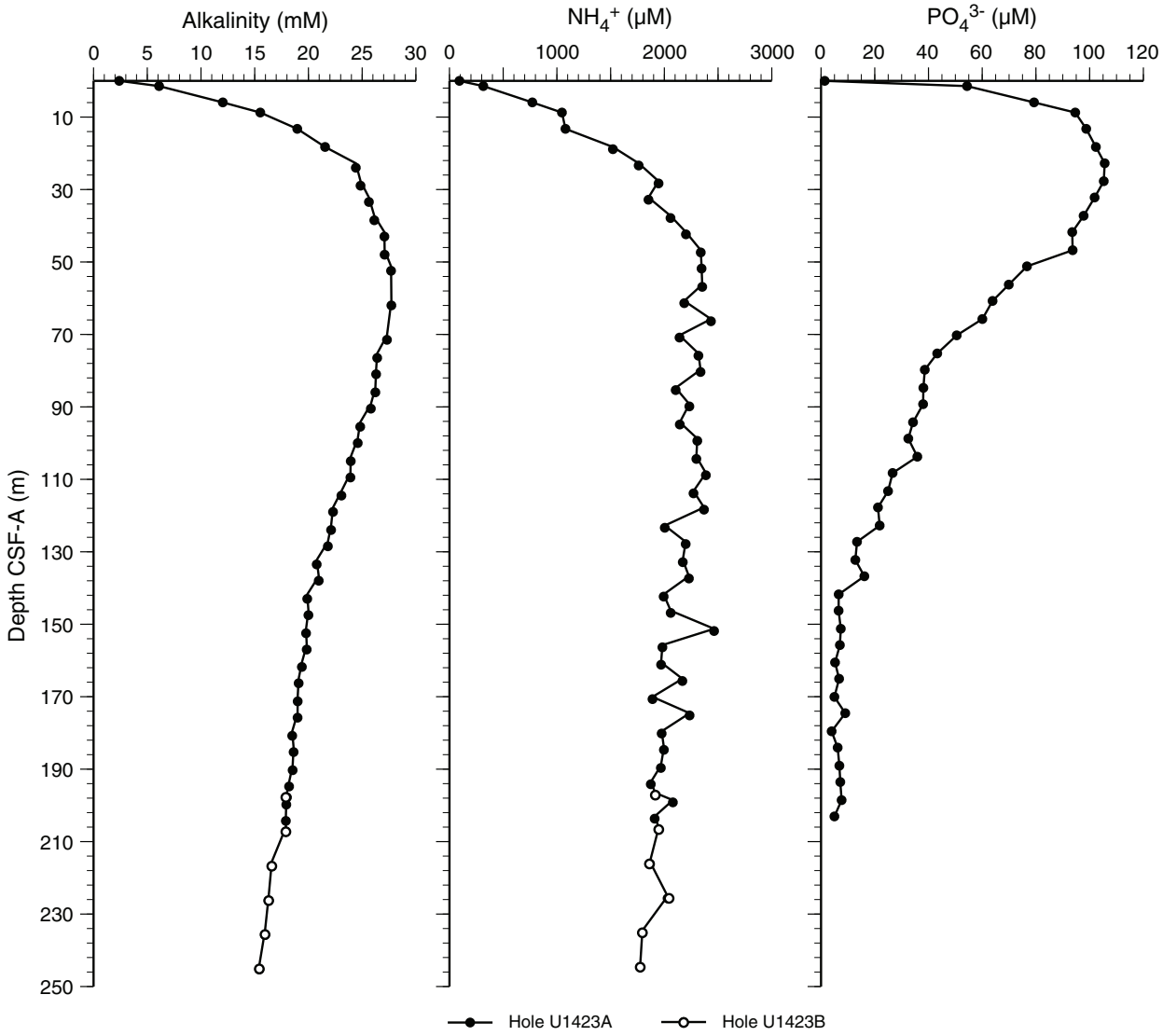

Figure F25. Headspace CH_4 concentrations with depth at Site U1423 with Site U1422 for comparison. Note that values are not meaningful at depths where CH_4 surpasses saturation at 1 atm pressure (~40 m CSF-A).

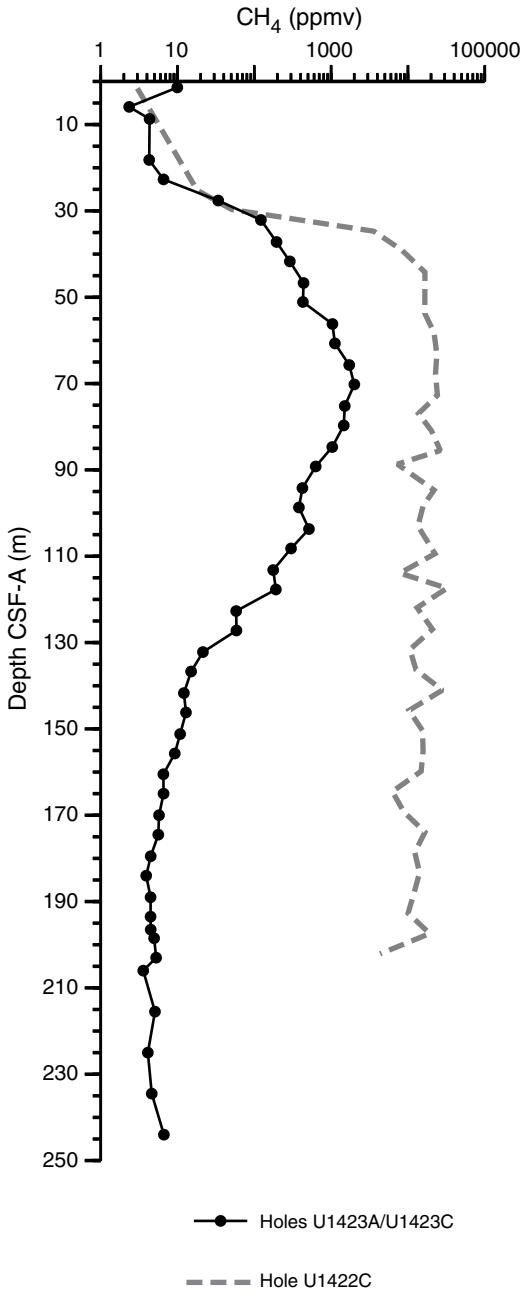

Figure F26. Headspace CH_4 and dissolved SO_4^{2-} concentrations with depth, Site U1423.

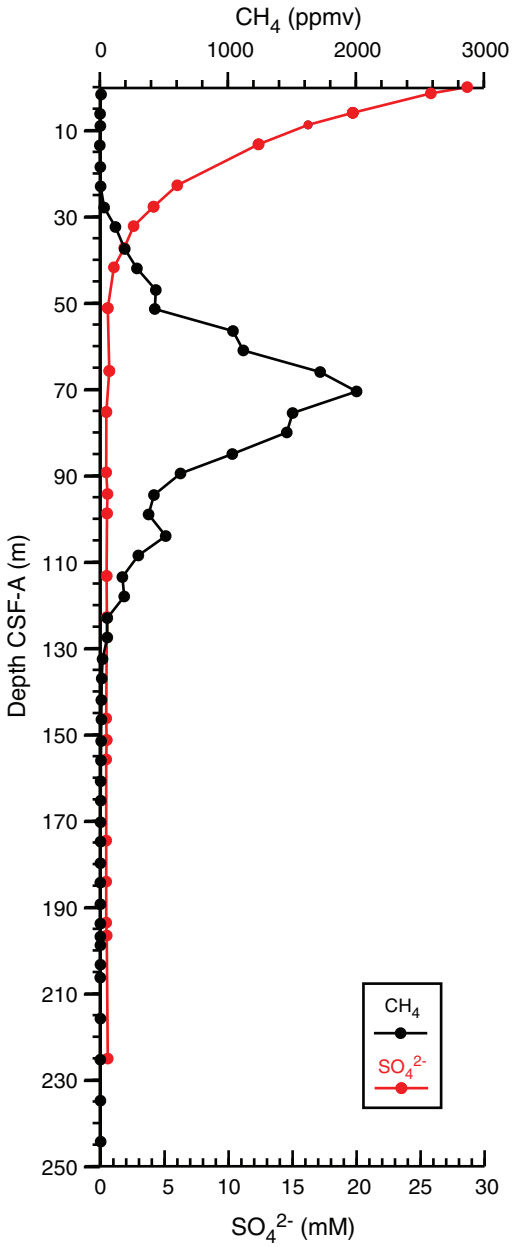

Figure F27. Dissolved SO_4^{2-} and barium profiles, Site U1423.

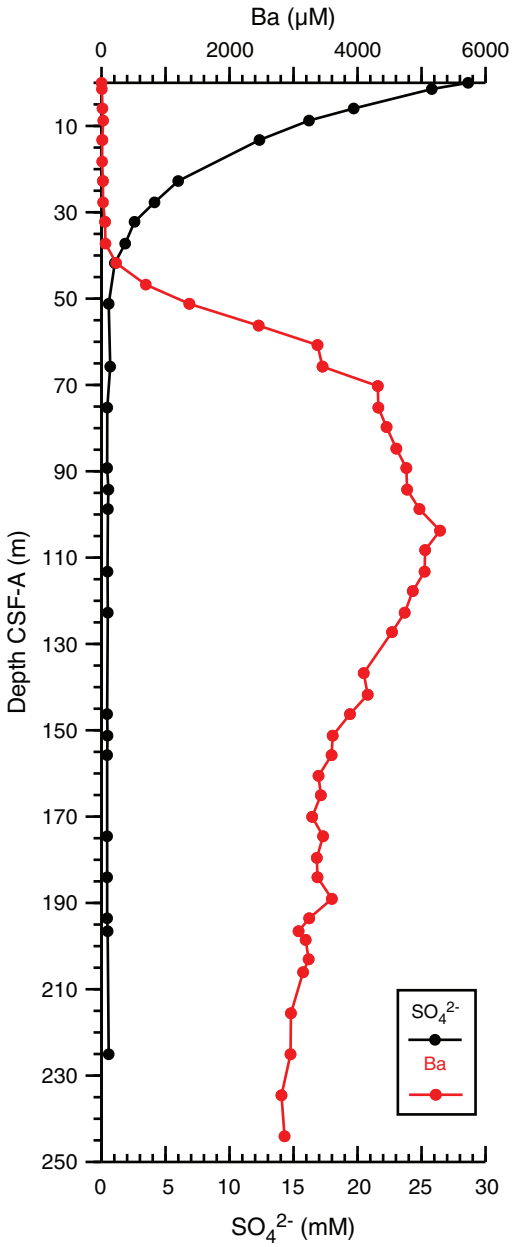

Figure F28. Dissolved calcium, magnesium, and strontium profiles, Site U1423.

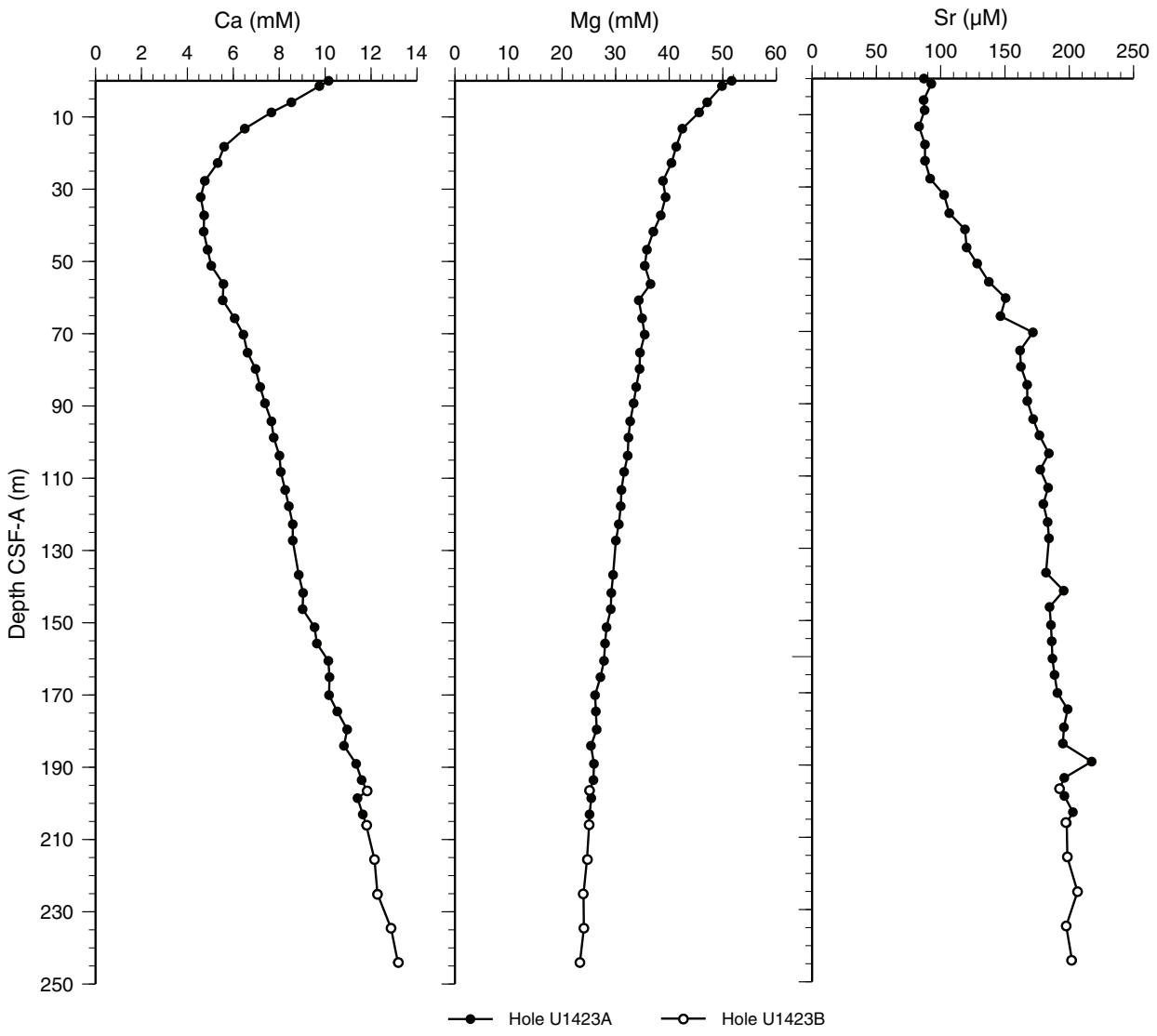

Figure F29. Dissolved Cl^-, Na, and K profiles, Site U1423.

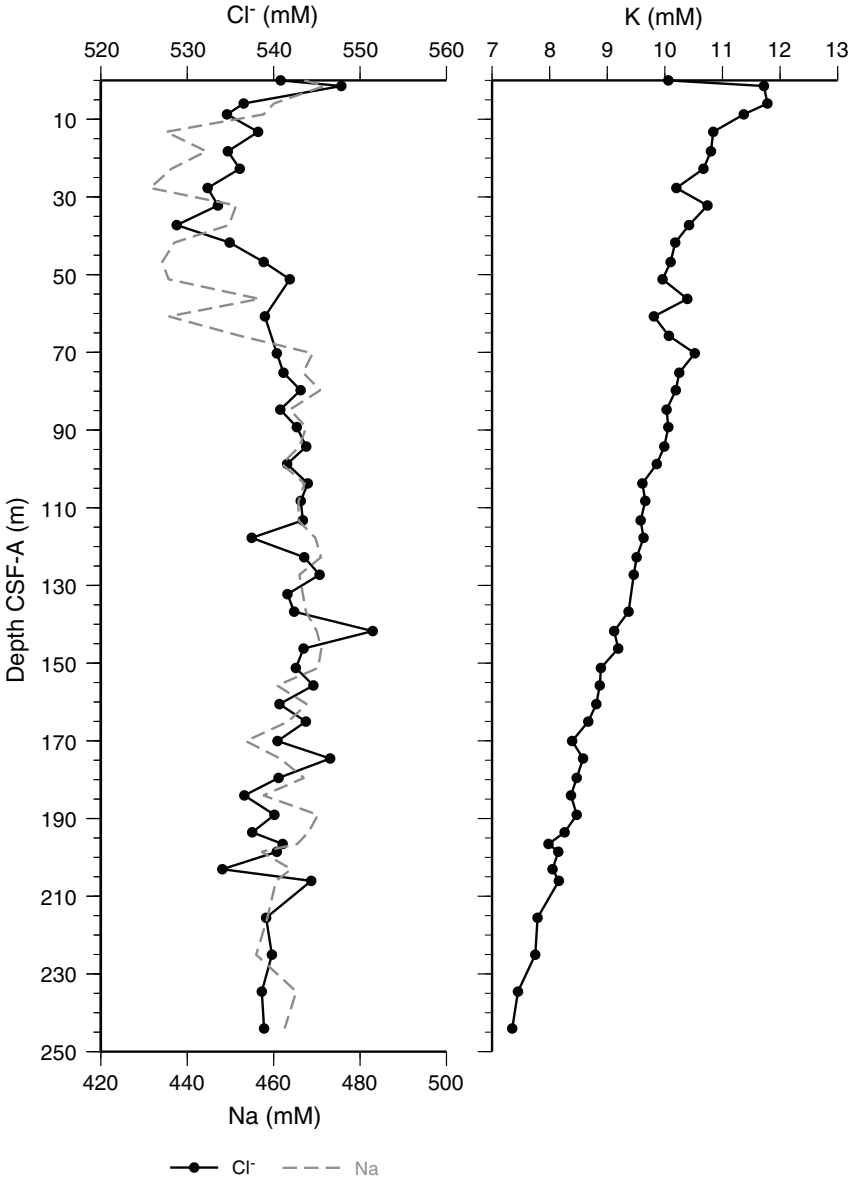

Figure F30. Dissolved B, Li, and silica concentrations with depth, Site U1423. The silica values determined by spectrophotometer (spec) agree favorably with the values determined on the inductively coupled plasma (ICP) –atomic emission spectroscopy. Solid circles indicate samples from Hole U1423A and open circles indicate samples from Hole U1423B.

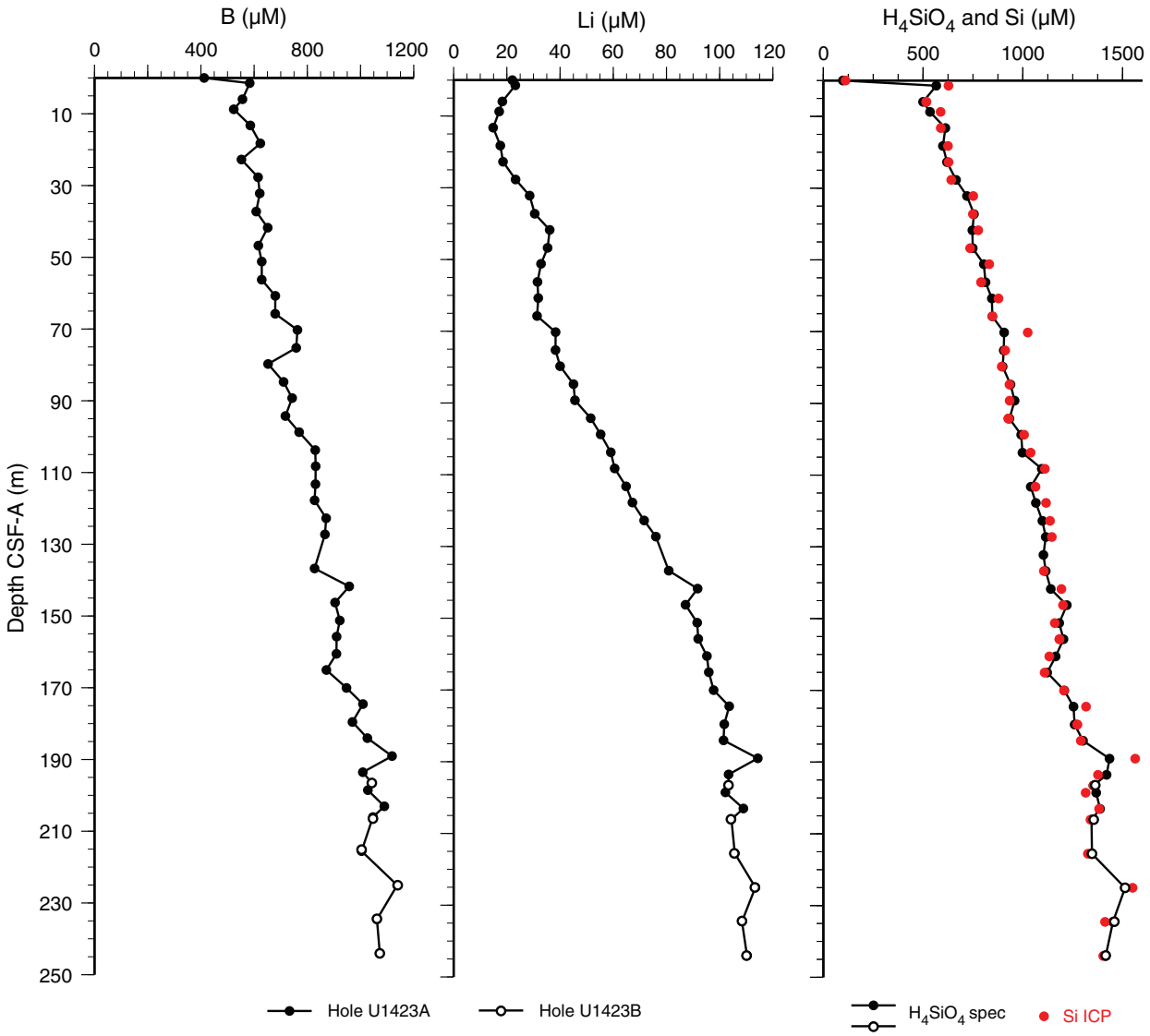

Figure F31. Paleomagnetism after 20 mT AF demagnetization, Site U1423. Chron column: black = normal polarity, white = reversed polarity, gray = zones or polarity boundaries without clear magnetostratigraphic interpretation. Inclination column: thin black dashed lines = expected geocentric axial dipole) inclinations at the site latitude during reversed (left) and normal (right) polarities, triangles along the left side mark depths where discrete paleomagnetic cube samples were collected (orange = discrete samples measured during the expedition). Declination column: gray dots = measured declination values, green dots = declination values corrected using core orientation data collected by the FlexIT tool. Susceptibility column: SHMSL and WRMSL measured values are shown in magenta and gray dots, respectively. **A.** Hole U1423A. (Continued on next two pages.)

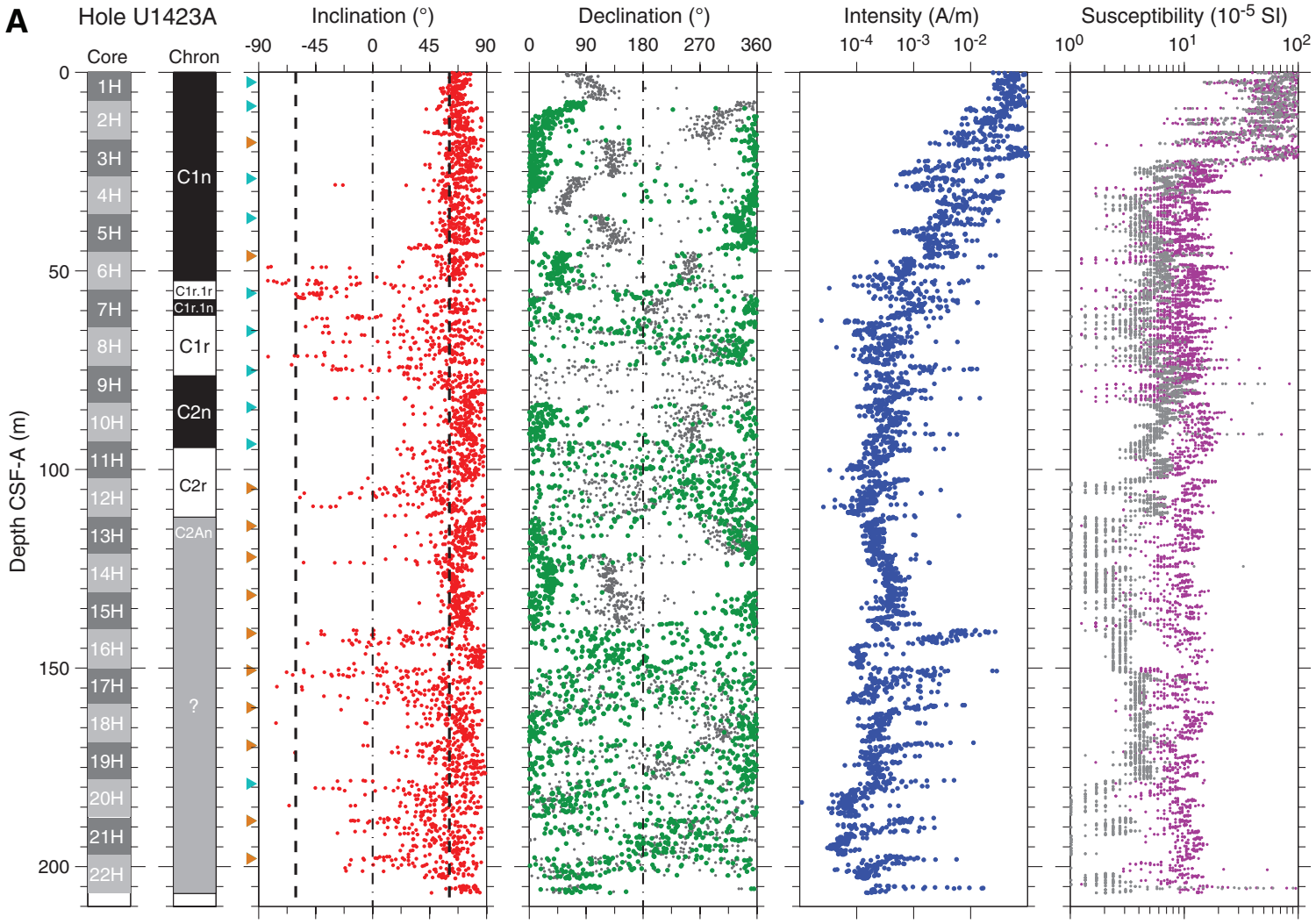

Figure F31 (continued). B. Hole U1423B. (Continued on next page.)

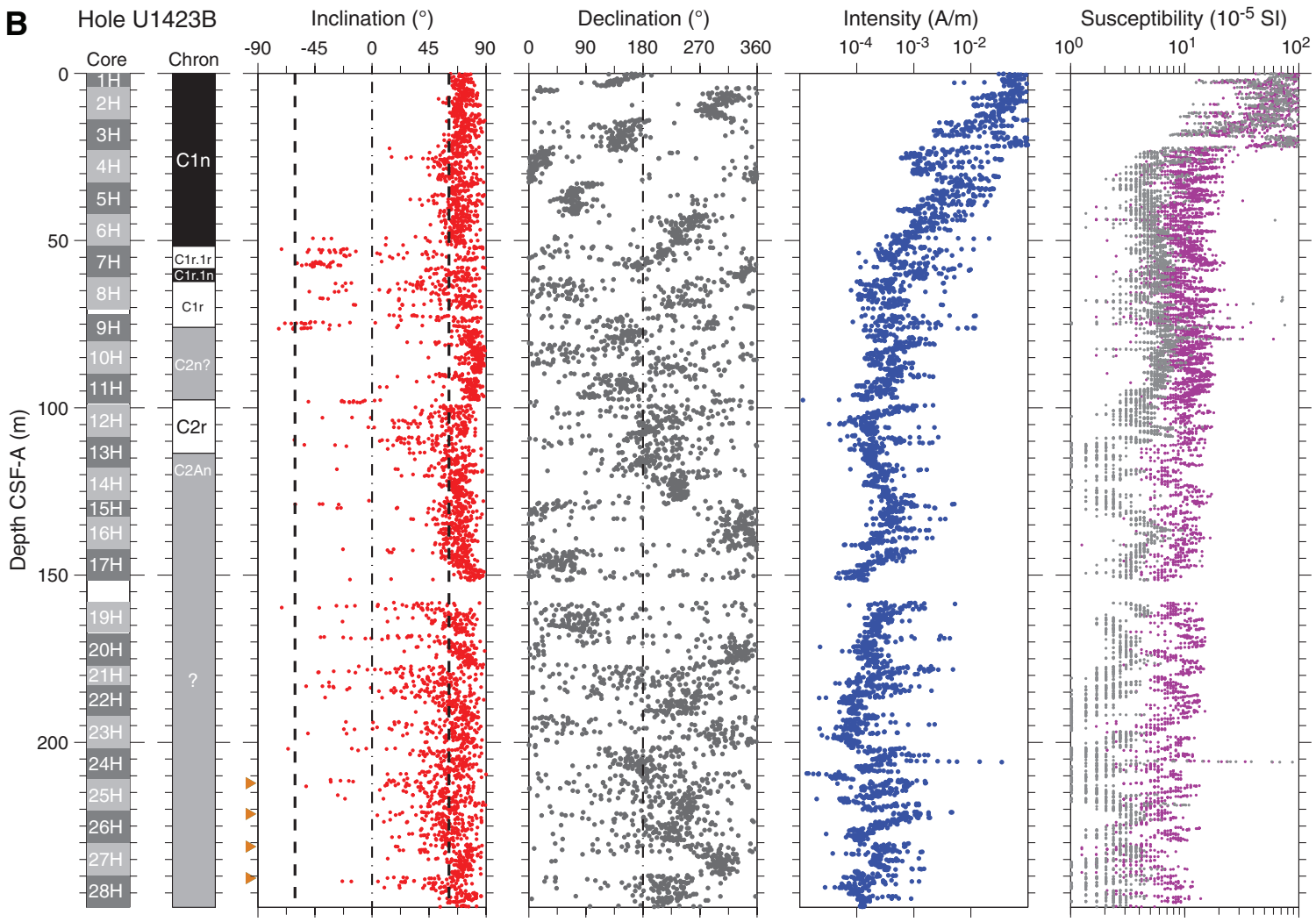

Figure F31 (continued). C. Hole U1423C.

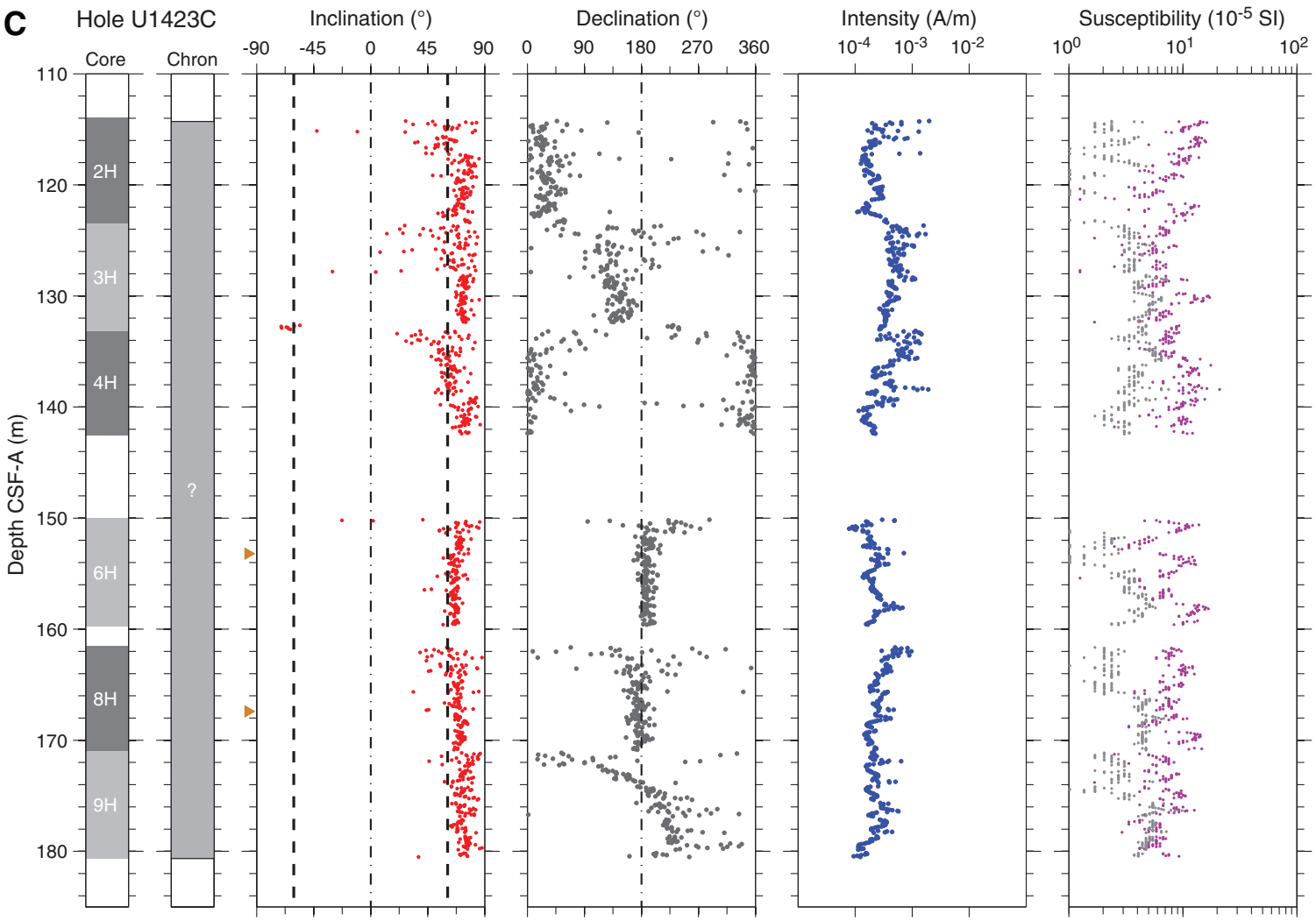

Figure F32. A–H. AF demagnetization results for eight discrete samples, Site U1423. For each sample, the left plot shows the intensity variation with progressive demagnetization. The middle and right plots show the NRM vector measured after each demagnetization treatment on an orthogonal projection (Zijderveld) and on an equal area projection, respectively. In the orthogonal projection plot, squares = horizontal projections, circles = vertical projections. In the equal area projection plot, solid circles = projection data with positive inclinations, open circles = projection data with negative inclinations. Note that on the orthogonal projection (Zijderveld) plot, NRM data before demagnetization have been removed to better display the demagnetized data.

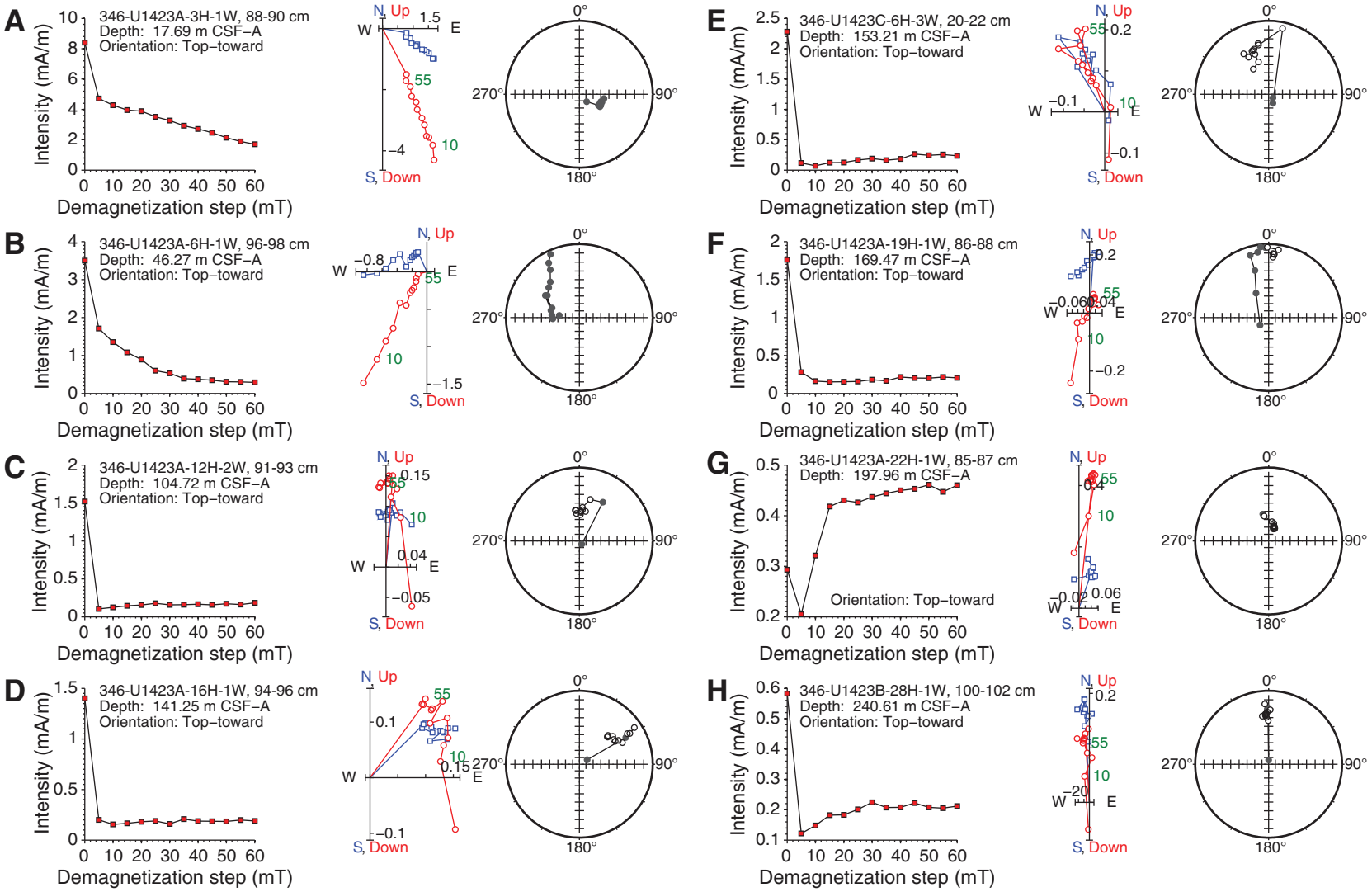

Figure F33. Suite of physical properties measured in Holes U1423A and U1423B. The first magnetic susceptibility panel shows WRMSL data of Holes U1423A (red) and U1423B (black), whereas the second panel shows WRSML data of Hole U1423B (black) and point SHMSL susceptibility data of Holes U1423A (blue) and U1423B (green). WRMSL gamma ray attenuation (GRA) bulk density is from Holes U1423A (red) and U1423B (black). Natural gamma radiation (NGR) is from in Holes U1423A (light blue) and U1423B (black). *P*-wave velocity panel shows combined WRMSL data of Holes U1423A and U1423B. Dashed horizontal lines = lithologic subunit boundaries, solid horizontal line = lithologic Unit I/II boundary.

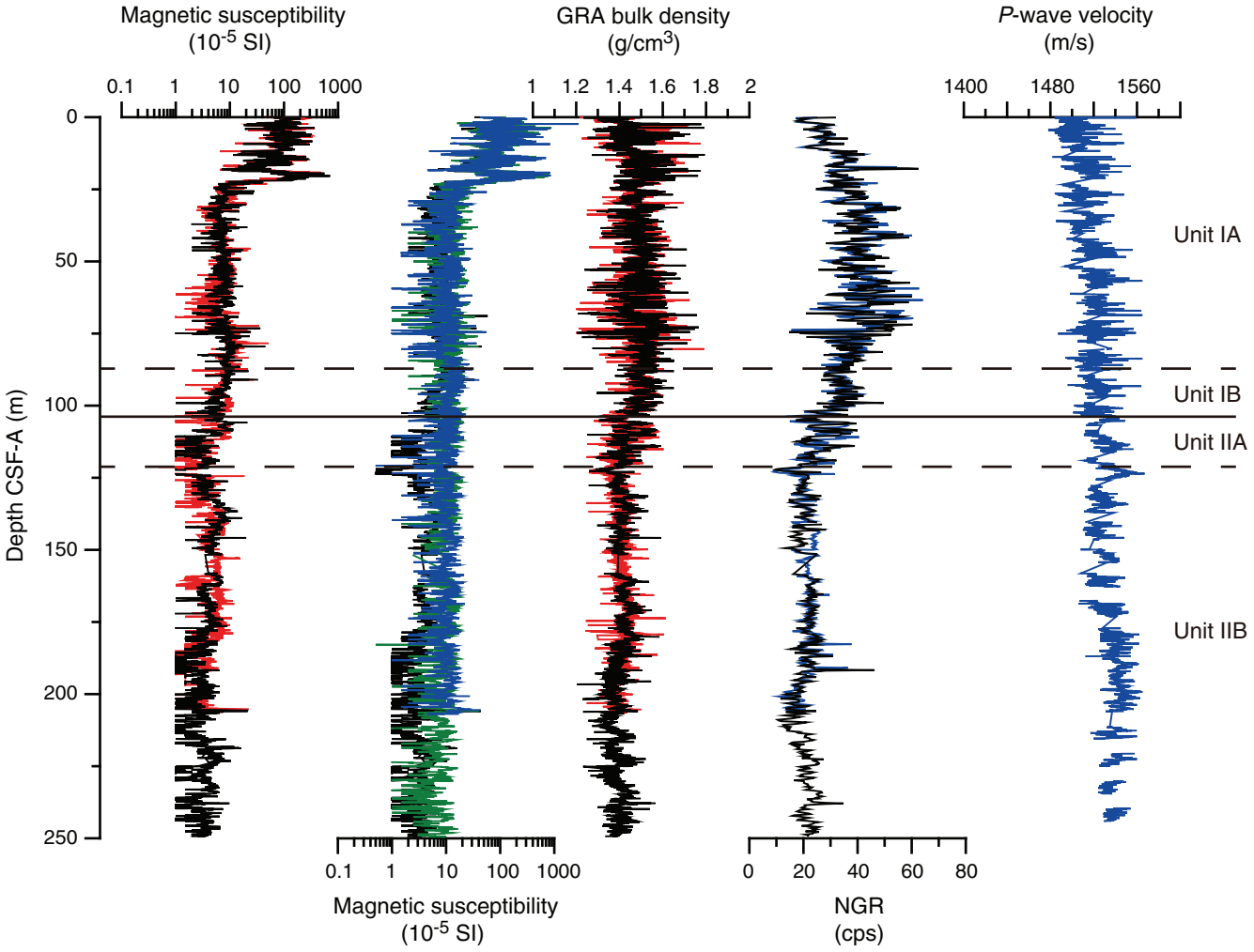

Figure F34. *P*-wave velocity measured with the WRMSL before (~12°C; black) and after (~20°C; blue) temperature equilibrium in Cores 346-U1423B-3H, 7H, and 16H.

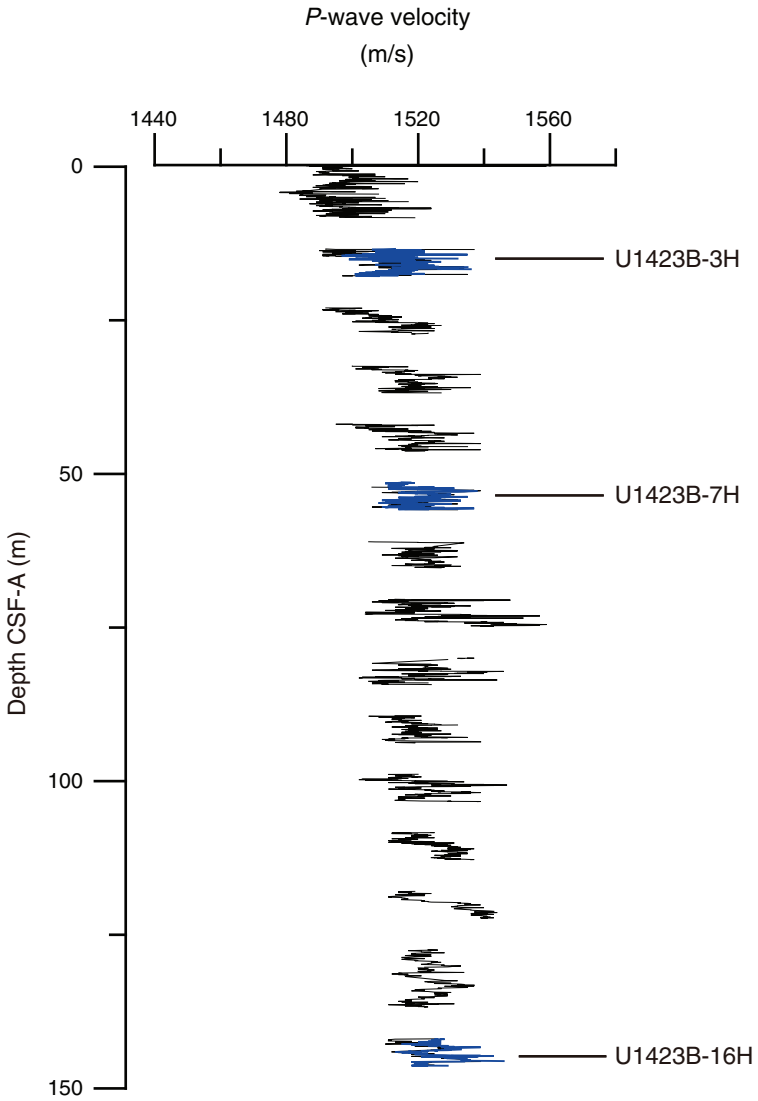

Figure F35. Discrete bulk density, grain density, porosity, water content, and shear strength, Site U1423. Dashed horizontal lines = lithologic subunit boundaries, solid horizontal line = lithologic Unit I/II boundary.

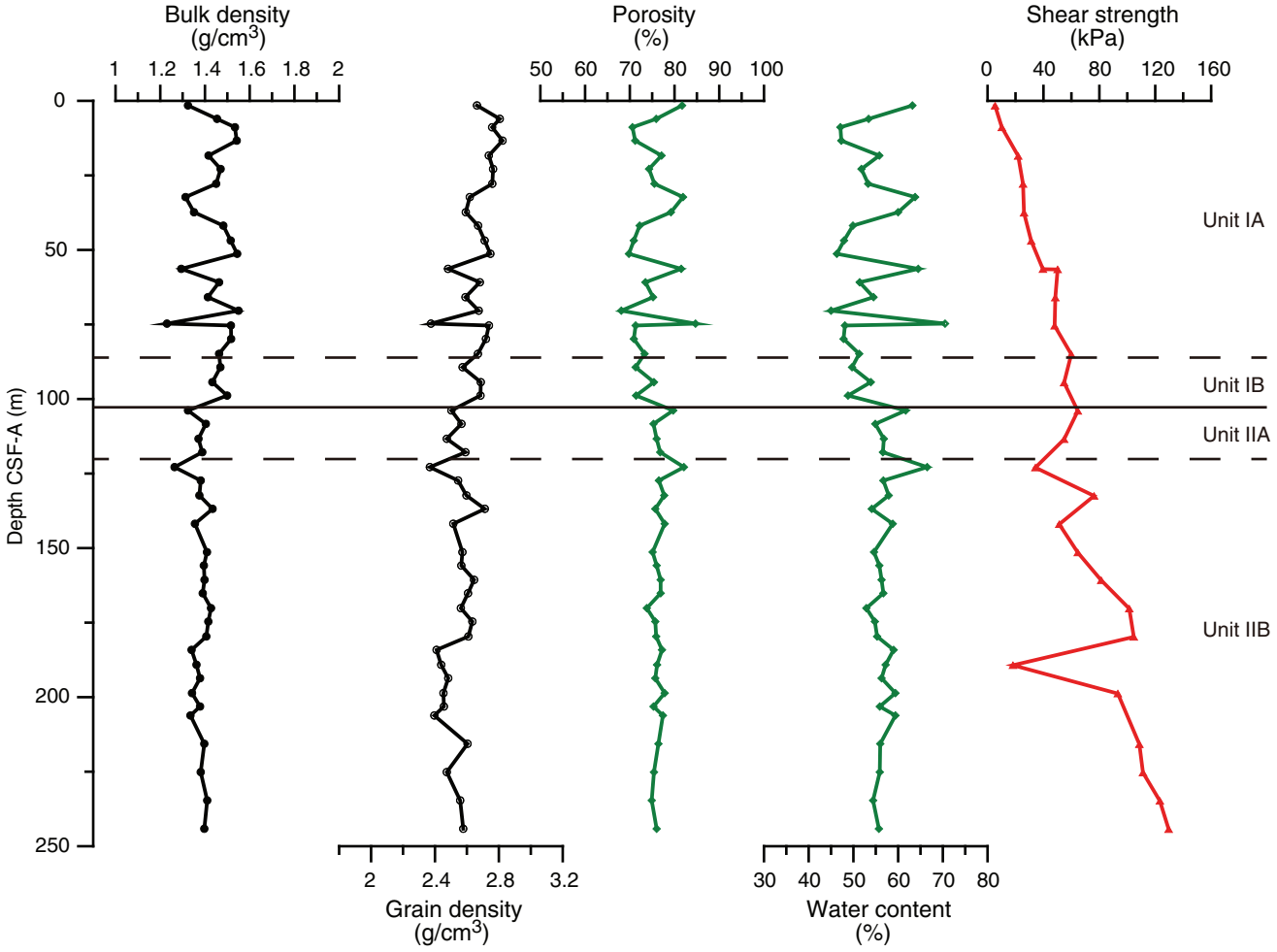

Figure F36. Color reflectance (L*, a*, and b*) in Holes U1423A (black, red, and dark blue lines) and U1423B (gray, orange, and light blue lines). Dashed horizontal lines = lithologic subunit boundaries, solid horizontal line = lithologic Unit I/II boundary.

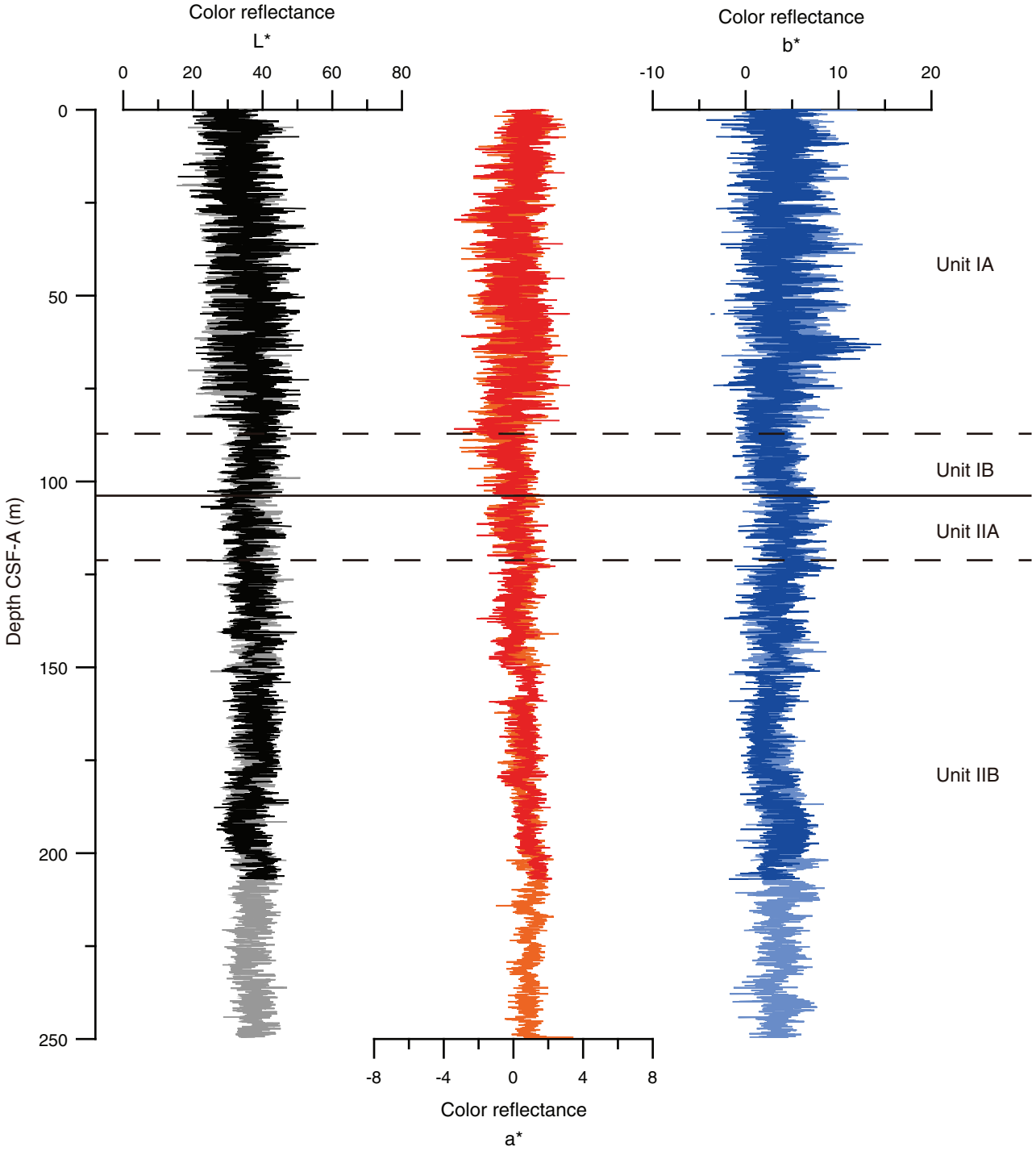

Figure F37. Downhole logs and logging units, Hole U1423B. HSGR = standard (total) gamma radiation, NGR = natural gamma radiation, RLA1 = shallow apparent resistivity, RLA5 = deep apparent resistivity, MS = magnetic susceptibility.

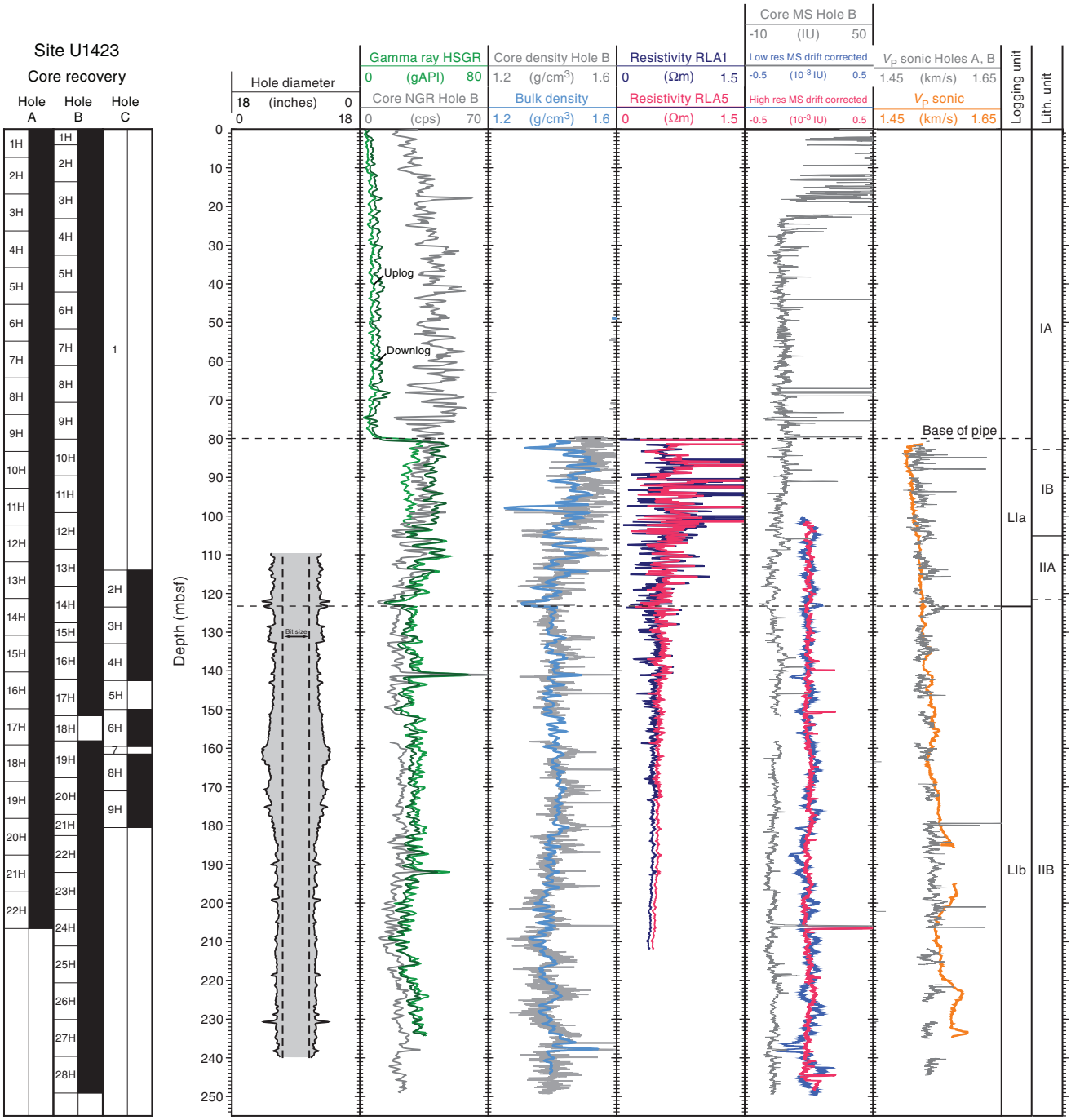

Figure F38. Natural gamma radiation downlogs (not corrected for variations in hole diameter), straight (non-oriented) Formation MicroScanner (FMS) images, and logging units, Hole U1423B. HSGR = standard (total) gamma radiation, HCGR = computed gamma radiation.

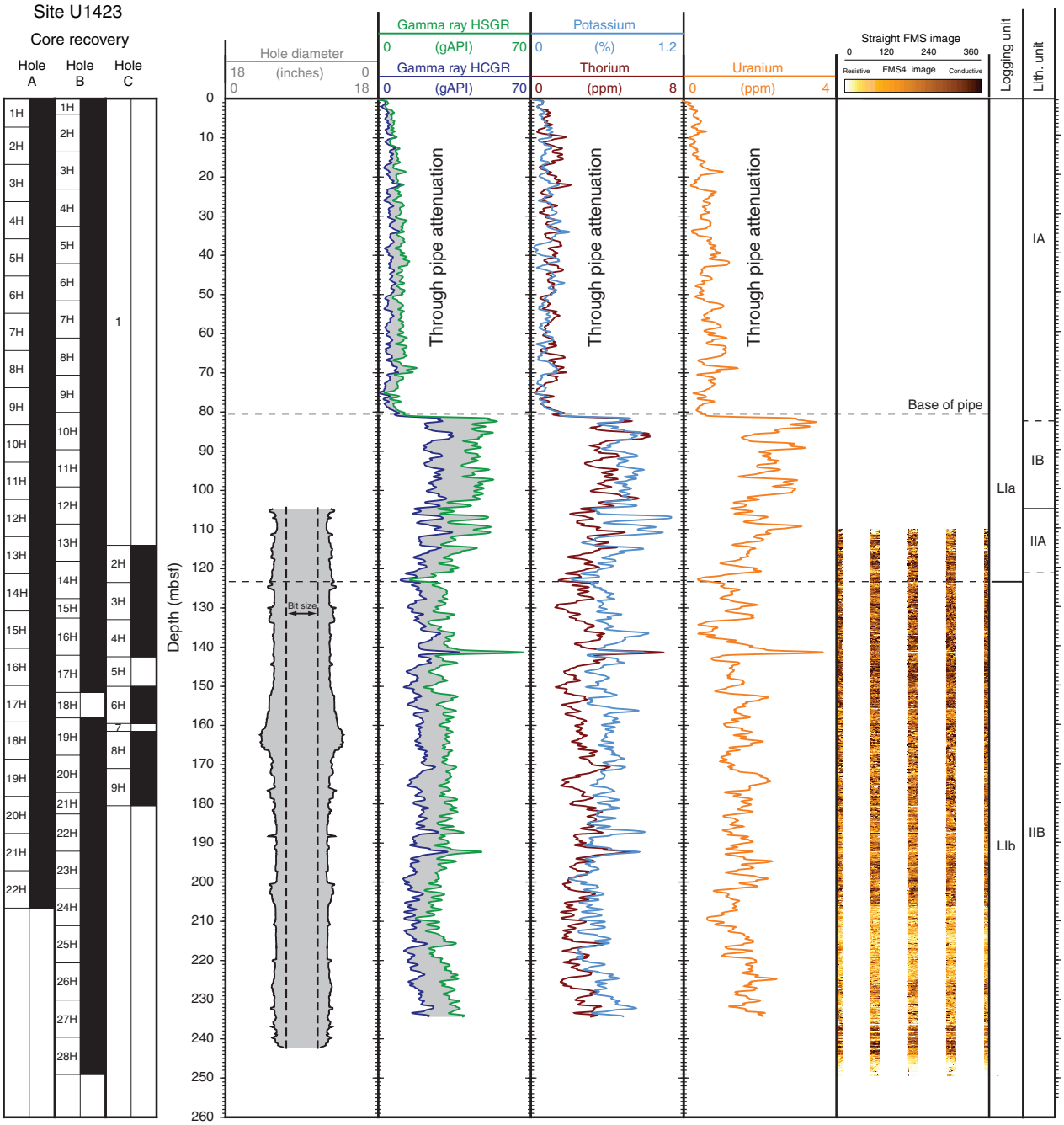

Figure F39. Logging operations summary diagram, Site U1423. FMS = Formation MicroScanner.

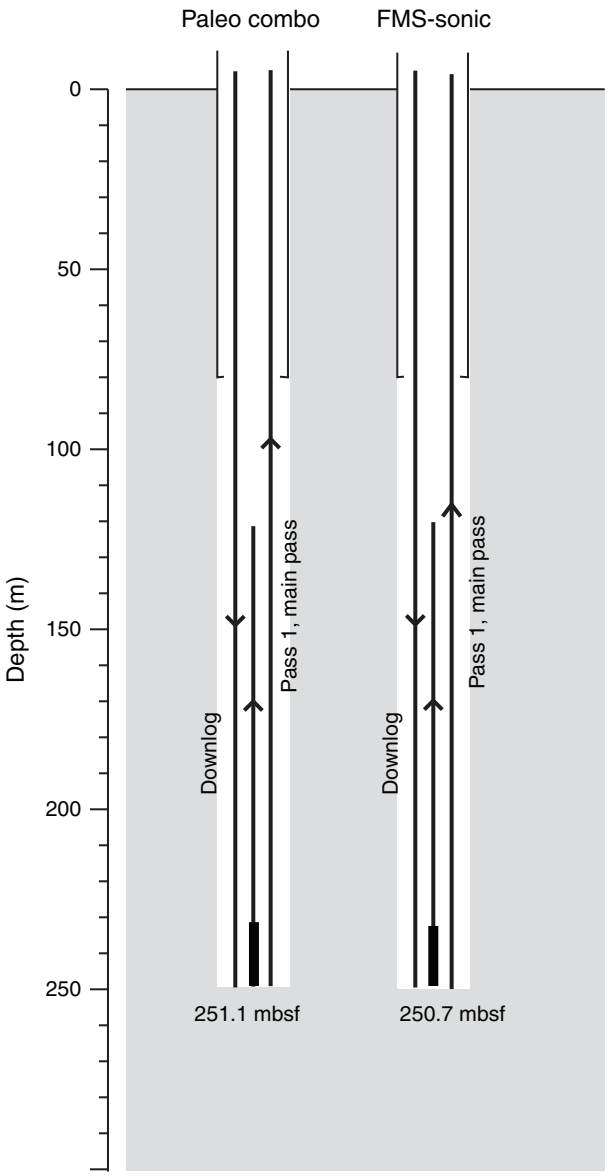

Figure F40. Correlation of downhole logs and lithology (110–126 mbsf) in Hole U1423B. The good hole condition allowed the Formation MicroScanner (FMS) pads to have good contact with the borehole wall and gave good images. NGR = natural gamma radiation, RHOM = high-resolution bulk density log, HSGR = standard (total) gamma radiation, RA5 = deep apparent resistivity.

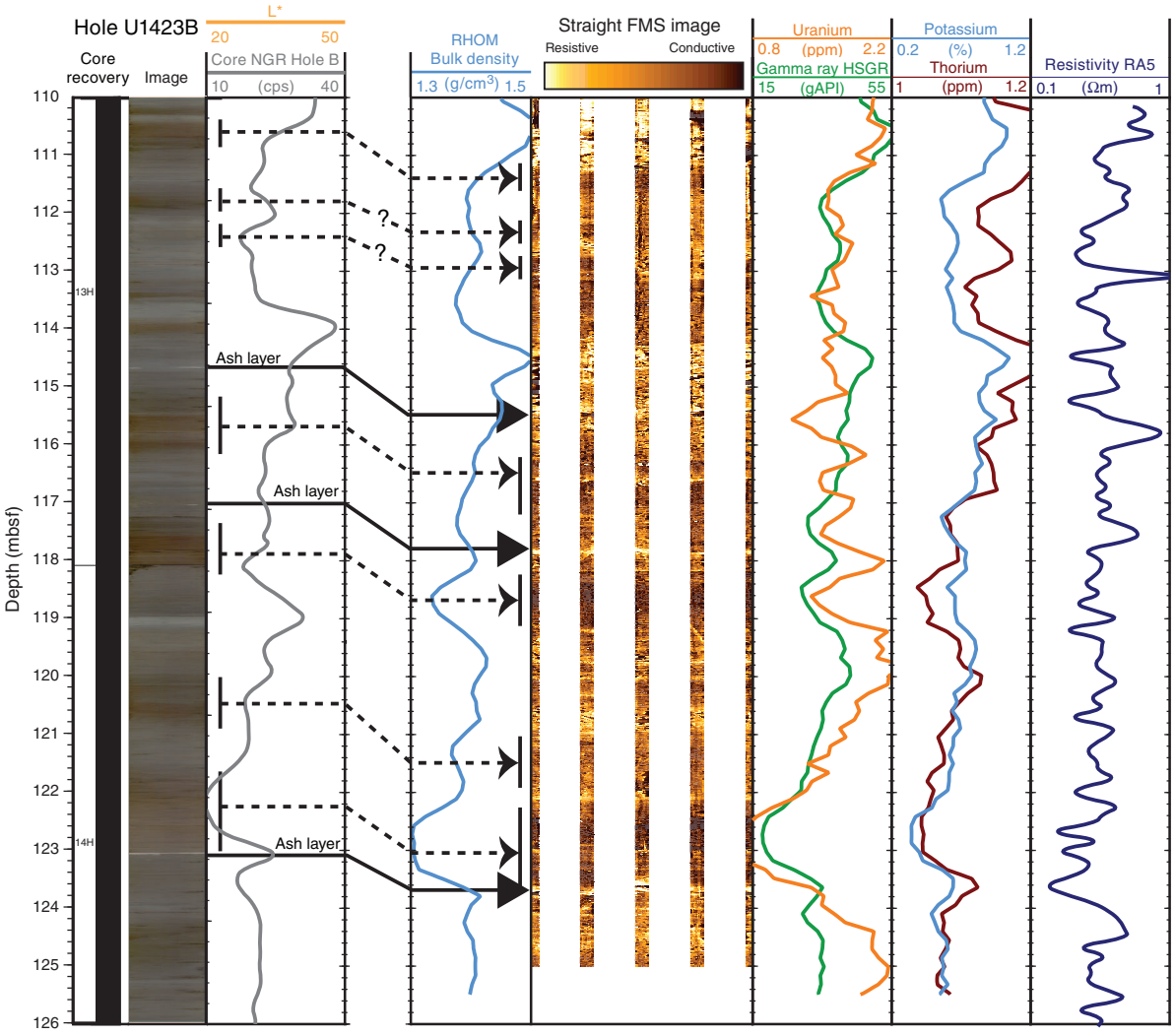

Figure F41. Correlation of downhole logs and lithology (230–243 mbsf) in Hole U1423B indicates that ash layers are more resistive than neighboring beds. RHOM = high-resolution bulk density log, FMS = Formation MicroScanner.

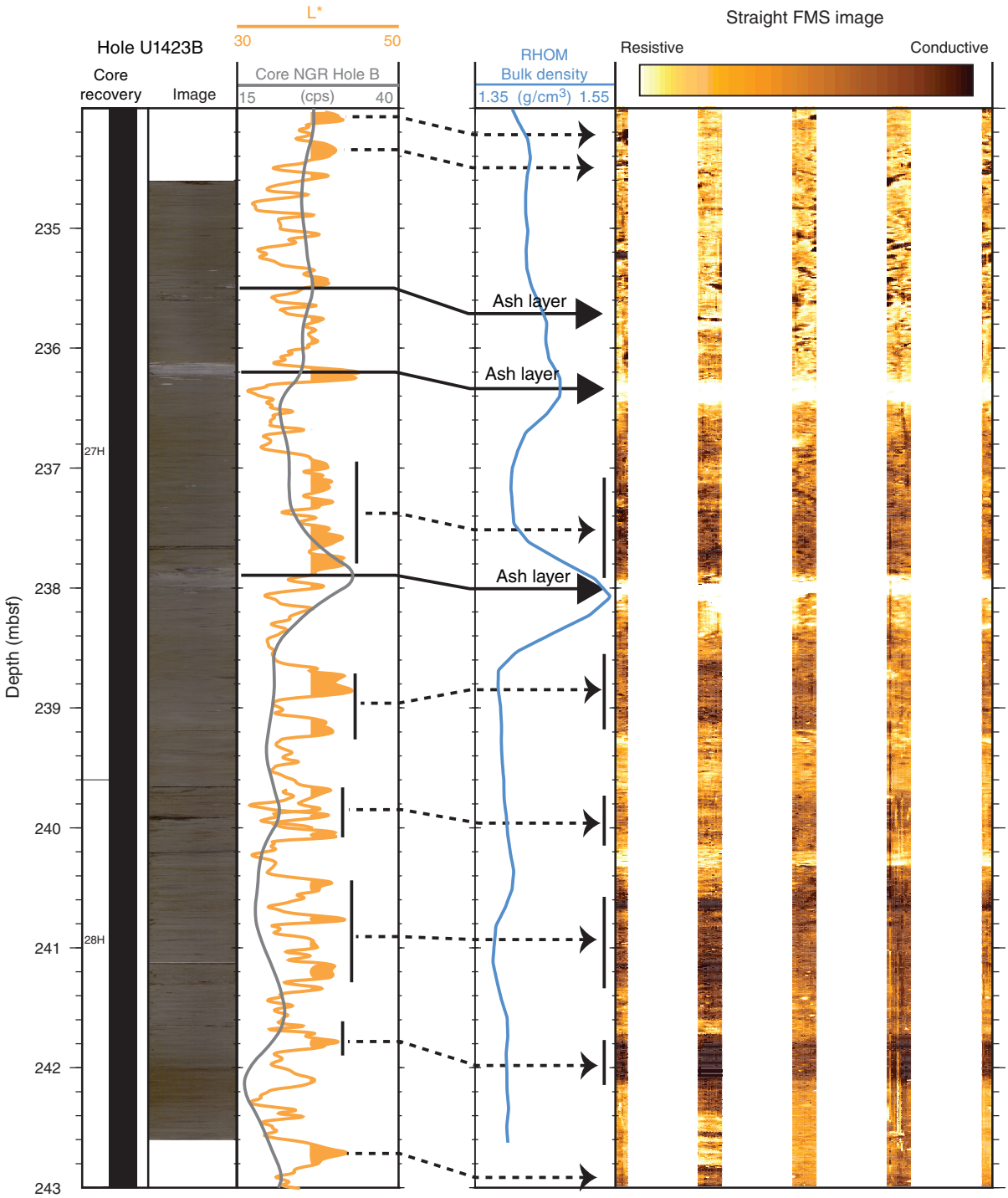

Figure F42. Plots of heat flow calculations, Hole U1423A. **A.** In situ sediment temperatures from advanced piston corer temperature tool (APCT-3) measurements with average values for Cores 346-U1423A-4H, 7H, 10H, and 13H (circles) and linear fit. **B.** In situ thermal conductivity data (squares) with calculated thermal resistance (solid line). **C.** Bullard plot of heat flow calculated from a linear fit of temperature vs. thermal resistance data.

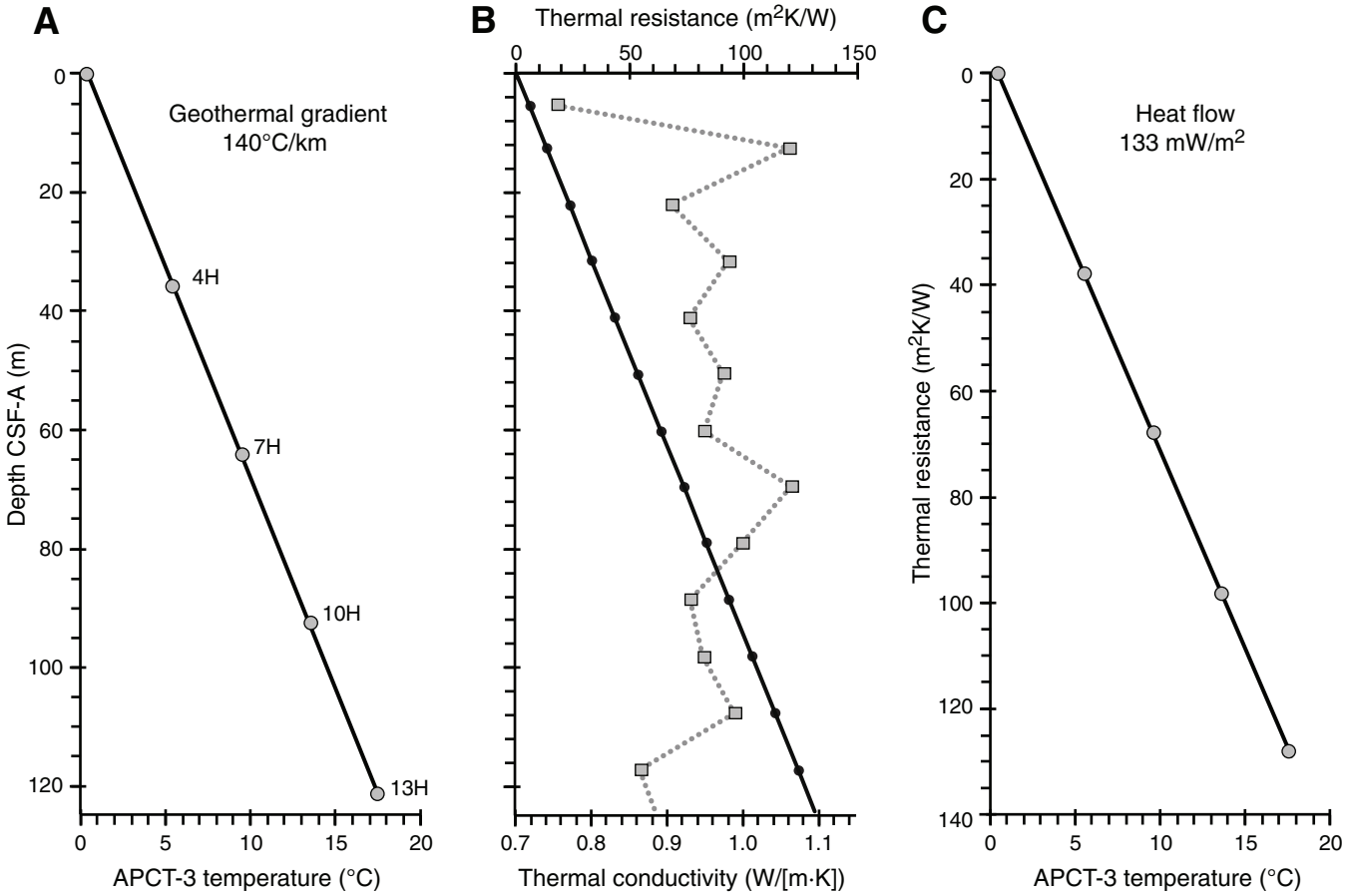

Figure F43. Composited cores and splice for Site U1423. Each core is adjusted (in depth) by a constant amount to align it with adjacent cores at a chosen tie point (typically a distinctive feature in all of the data sets). Other features may or may not align among adjacent cores because of differential squeezing and stretching during the coring process or to variable expansion characteristics. The splice is constructed from the composited cores by selecting intervals from different holes such that coring gaps are avoided and drilling disturbance is minimized. Data included in the splice are plotted on the CCSF-D scale, whereas data not included in the splice are plotted on the CCSF-A scale. Horizontal light blue lines indicate tie points where the splice changes from one hole to another. Only the splice is plotted on the correct *y*-axis scale; data from Holes U1423A, U1423B, and U1423C are offset by 40, 80, or 120 units, respectively, for illustrative purposes. One and two point spikes are artifacts generated when the track sensor measures beyond the end of the ~150 cm sections. The gap in the splice data at 90 m results from missing image data; it does not reflect a gap in the lithologic section. **A.** 0–50 m CCSF-A. (Continued on next two pages.)

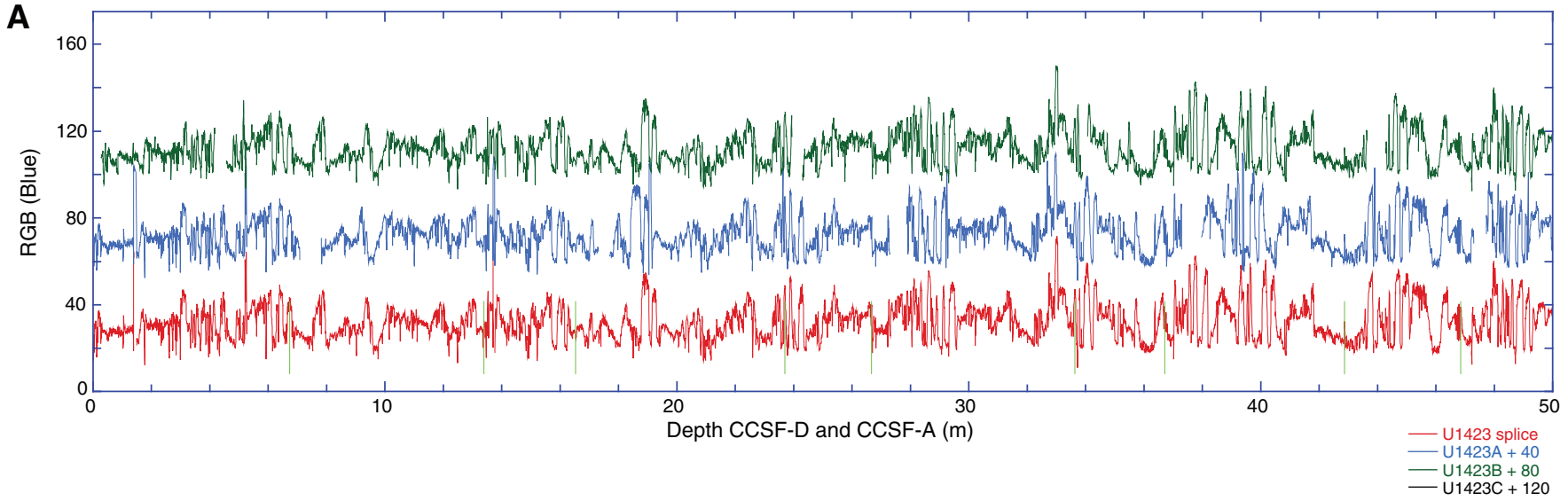

Figure F43 (continued). B. 50–150 m CCSF-A. (Continued on next page.)

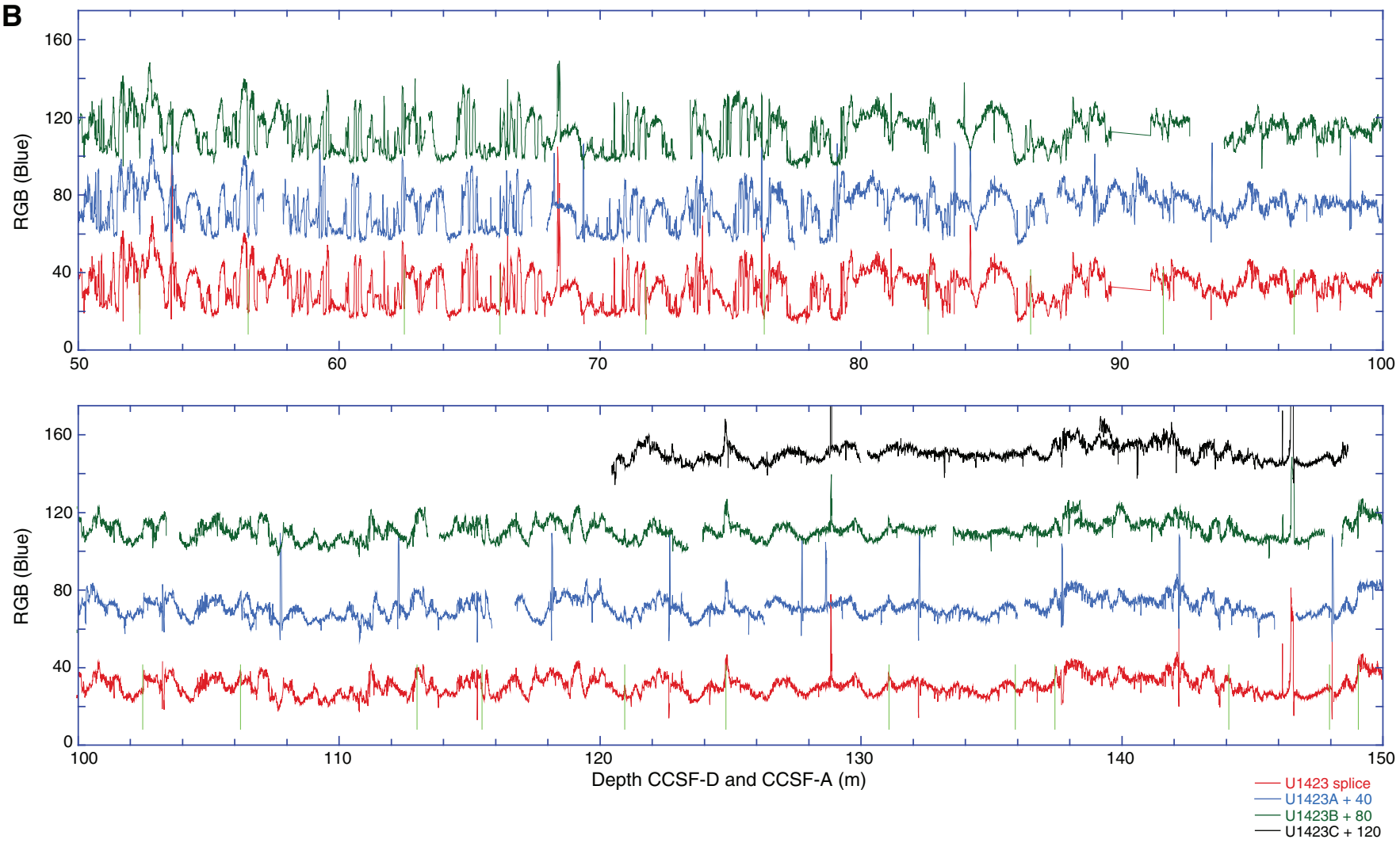

Figure F43 (continued). C. 150–225 m CCSF-A.

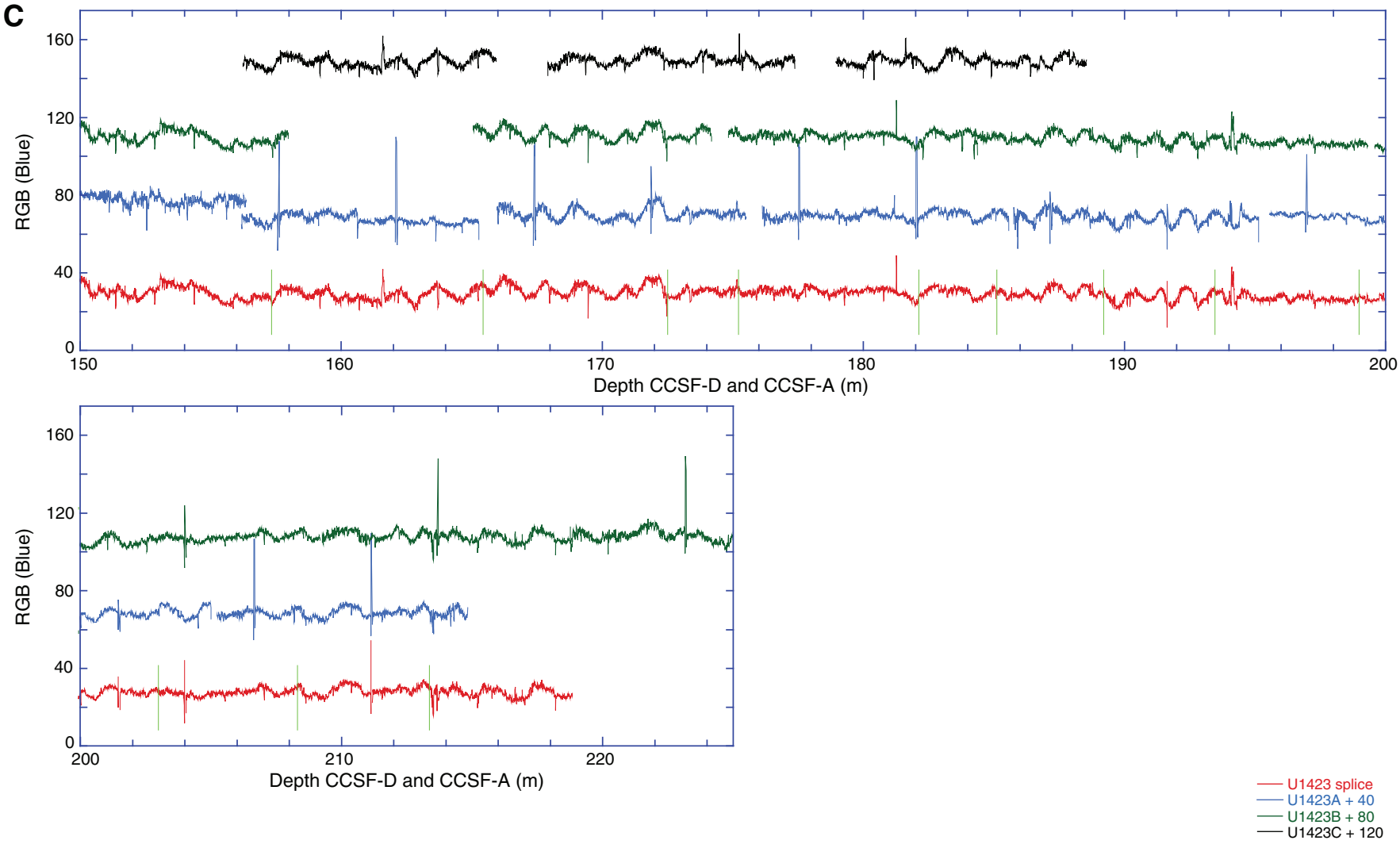

Figure F44. Age model and sedimentation rates, Site U1423. **A.** Synthesis of biostratigraphic and paleomagnetic age control points to establish a preliminary age model. **B.** Average sedimentation rates calculated between age control points.

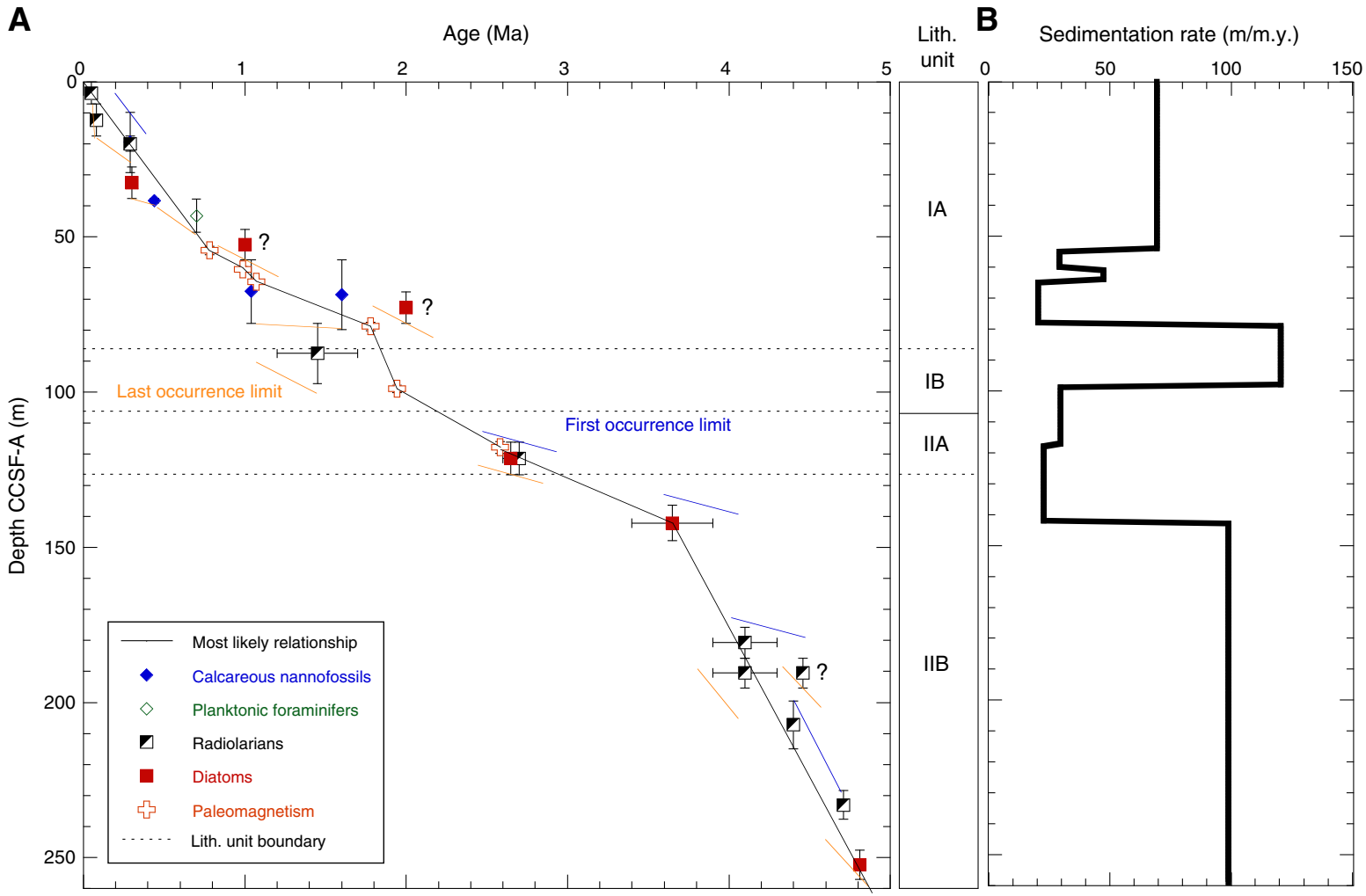

Table T1. Coring summary, Site U1423. (Continued on next page.)

Hole U1423A
Latitude: 41°41.9494′N
Longitude: 139°04.9805′E
Water depth (m): 1785.25
Date started (UTC): 1442 h 21 August 2013
Date finished (UTC): 1455 h 22 August 2013
Time on hole (days): 1.01
Seafloor depth (drill pipe measurement below rig floor, m DRF): 1796.6
Distance between rig floor and sea level (m): 11.35
Penetration DSF (m): 206.6
Cored interval (m): 206.6
Recovered length (m): 212.89
Recovery (%): 103
Drilled interval (m): NA
Drilled interval: 0
Total cores: 22
APC cores: 22
XCB cores: 0
RCB cores: 0
Other cores: 0

Hole U1423B
Latitude: 41°41.9575′N
Longitude: 139°04.9800′E
Water depth (m): 1785.44
Date started (UTC): 1455 h 22 August 2013
Date finished (UTC): 2015 h 23 August 2013
Time on hole (days): 1.22
Seafloor depth (drill pipe measurement below rig floor, m DRF): 1796.8
Distance between rig floor and sea level (m): 11.36
Penetration DSF (m): 249.1
Cored interval (m): 249.1
Recovered length (m): 250
Recovery (%): 100
Drilled interval (m): NA
Drilled interval: 0
Total cores: 28
APC cores: 28
XCB cores: 0
RCB cores: 0
Other cores: 0

Hole U1423C
Latitude: 41°41.9511′N
Longitude: 139°04.9804′E
Water depth (m): 1785.22
Date started (UTC): 2015 h 23 August 2013
Date finished (UTC): 1236 h 24 August 2013
Time on hole (days): 0.68
Seafloor depth (drill pipe measurement below rig floor, m DRF): 1796.6
Distance between rig floor and sea level (m): 11.38
Penetration DSF (m): 180.5
Cored interval (m): 57
Recovered length (m): 59.07
Recovery (%): 104
Drilled interval (m): 123.5
Drilled interval: 3
Total cores: 6
APC cores: 6
XCB cores: 0
RCB cores: 0
Other cores: 0

Site U1423 totals
Number of cores: 56
Penetration (m): 636.2
Cored (m): 512.7
Recovered (m): 521.96 (101.8%)

Table T1 (continued).

Core	Date (Aug 2013)	Time (h)	Top depth of cored interval DSF (m)	Bottom depth of cored interval DSF (m)	Interval advanced (m)	Top depth of recovered core CSF (m)	Bottom depth of recovered core CSF (m)	Length of core recovered (m)	Curated length (m)	Recovery (%)
346-U1423A-										
1H	21	2150	0.0	7.3	7.3	0.0	7.26	7.26	7.26	99
2H	21	2250	7.3	16.8	9.5	7.3	17.02	9.72	9.72	102
3H	21	2325	16.8	26.3	9.5	16.8	26.63	9.83	9.83	103
4H	22	0020	26.3	35.8	9.5	26.3	36.12	9.82	9.82	103
5H	22	0050	35.8	45.3	9.5	35.8	45.43	9.63	9.63	101
6H	22	0125	45.3	54.8	9.5	45.3	54.96	9.66	9.66	102
7H	22	0205	54.8	64.3	9.5	54.8	64.69	9.89	9.89	104
8H	22	0245	64.3	73.8	9.5	64.3	74.19	9.89	9.89	104
9H	22	0320	73.8	83.3	9.5	73.8	83.64	9.84	9.84	104
10H	22	0405	83.3	92.8	9.5	83.3	93.21	9.91	9.91	104
11H	22	0440	92.8	102.3	9.5	92.8	102.60	9.80	9.80	103
12H	22	0510	102.3	111.8	9.5	102.3	112.11	9.81	9.81	103
13H	22	0600	111.8	121.3	9.5	111.8	121.74	9.94	9.94	105
14H	22	0635	121.3	130.8	9.5	121.3	131.24	9.94	9.94	105
15H	22	0725	130.8	140.3	9.5	130.8	140.56	9.76	9.76	103
16H	22	0840	140.3	149.8	9.5	140.3	150.24	9.94	9.94	105
17H	22	0940	149.8	159.1	9.3	149.8	159.17	9.37	9.37	101
18H	22	1030	159.1	168.6	9.5	159.1	168.93	9.83	9.83	103
19H	22	1105	168.6	178.1	9.5	168.6	178.39	9.79	9.79	103
20H	22	1140	178.1	187.6	9.5	178.1	187.77	9.67	9.67	102
21H	22	1215	187.6	197.1	9.5	187.6	197.27	9.67	9.67	102
22H	22	1300	197.1	206.6	9.5	197.1	207.02	9.92	9.92	104
				Total advanced (m):	206.6		Total recovered (m):	212.89		
346-U1423B-										
1H	22	1555	0.0	4.1	4.1	0.0	4.09	4.09	4.09	100
2H	22	1630	4.1	13.6	9.5	4.1	13.90	9.80	9.80	103
3H	22	1700	13.6	23.1	9.5	13.6	23.39	9.79	9.79	103
4H	22	1735	23.1	32.6	9.5	23.1	32.95	9.85	9.85	104
5H	22	1800	32.6	42.1	9.5	32.6	42.34	9.74	9.74	103
6H	22	1830	42.1	51.6	9.5	42.1	51.74	9.64	9.64	101
7H	22	1900	51.6	61.1	9.5	51.6	61.41	9.81	9.81	103
8H	22	1930	61.1	70.6	9.5	61.1	70.84	9.74	9.74	103
9H	22	2005	70.6	80.1	9.5	70.6	80.47	9.87	9.87	104
10H	22	2035	80.1	89.6	9.5	80.1	89.84	9.74	9.74	103
11H	22	2105	89.6	99.1	9.5	89.6	99.34	9.74	9.74	103
12H	22	2130	99.1	108.6	9.5	99.1	108.87	9.77	9.77	103
13H	22	2200	108.6	118.1	9.5	108.6	118.46	9.86	9.86	104
14H	22	2230	118.1	127.6	9.5	118.1	127.88	9.78	9.78	103
15H	22	2300	127.6	132.6	5.0	127.6	132.85	5.25	5.25	105
16H	22	2345	132.6	142.1	9.5	132.6	142.46	9.86	9.86	104
17H	23	0010	142.1	151.6	9.5	142.1	151.95	9.85	9.85	104
18H	23	0045	151.6	158.1	6.5	151.6	151.60	0.00	0.00	0
19H	23	0115	158.1	167.6	9.5	158.1	167.56	9.46	9.46	100
20H	23	0145	167.6	177.1	9.5	167.6	177.39	9.79	9.79	103
21H	23	0215	177.1	182.6	5.5	177.1	183.07	5.97	5.97	109
22H	23	0340	182.6	192.1	9.5	182.6	192.38	9.78	9.78	103
23H	23	0400	192.1	201.6	9.5	192.1	201.95	9.85	9.85	104
24H	23	0435	201.6	211.1	9.5	201.6	211.47	9.87	9.87	104
25H	23	0500	211.1	220.6	9.5	211.1	220.83	9.73	9.73	102
				Total advanced (m):	220.6		Total recovered (m):	220.63		
346-U1423C-										
11	20	0440			*****Drilled from 0.0 to 114.0 mbsf*****					
2H	20	0535	114.0	123.5	9.5	114.0	123.84	9.84	9.84	104
3H	20	0650	123.5	133.0	9.5	123.5	133.42	9.92	9.92	104
4H	20	0740	133.0	142.5	9.5	133.0	142.70	9.70	9.70	102
52	20	0830			*****Drilled from 142.5 to 150.0 mbsf*****					
6H	20	0925	150.0	159.5	9.5	150.0	160.00	10.00	10.00	105
73	20	1015			*****Drilled from 159.5 to 161.5 mbsf*****					
8H	20	1105	161.5	171.0	9.5	161.5	171.20	9.70	9.70	102
9H	20	1200	171.0	180.5	9.5	171.0	180.91	9.91	9.91	104
				Total advanced (m):	180.5		Total recovered (m):	59.07		

DRF = drilling depth below rig floor, DSF = drilling depth below seafloor, CSF = core depth below seafloor. APC = advanced piston corer, XCB = extended core barrel, RCB = rotary core barrel. H = APC system, numeric core type = drilled interval. NA = not applicable.

Table T2. Visible tephra layers thicker than 0.5 cm, Hole U1423A.

Core, section, interval (cm)	Thickness (cm)	Color	Occurrence
346-U1423A-			
1H-2, 112–113	1.0	Dark gray	Layered
1H-3, 95–104	2.0	Light gray	Layered
1H-4, 72–77	5.0	White	Layered
1H-5, 26–30	1.3	White	Patched
2H-4, 126–127	1.0	White	Layered
3H-1, 52–52.5	0.5	Black	Layered
3H-2, 89–90	1.0	Dark gray	Layered
3H-3, 19–20	1.0	Gray	Layered
3H-3, 38–45	2.0	Gray	Layered
3H-3, 112–113.5	1.5	Light gray–gray	Layered
3H-4, 44–45	1.0	Dark gray	Layered
3H-5, 14–15	1.0	Gray	Layered
3H-5, 34–35	1.0	Gray	Layered
3H-7, 15–16	1.0	Light gray	Layered
4H-3, 44–45	1.0	Gray	Layered
4H-3, 109.5–110.5	1.0	Gray	Layered
4H-4, 10–12	2.0	Gray	Layered
4H-5, 8–8.5	0.5	Light gray	Layered
5H-3, 90–91	1.0	Gray	Layered
6H-1, 11–27	16.0	Light gray	Layered
6H-5, 19–20	1.0	Light gray	Layered
6H-6, 100.5–101	0.5	Light gray	Layered
7H-1, 14–18	4.0	Light gray–gray	Layered
7H-1, 37–37.5	0.5	Gray	Layered
7H-3, 88–91	3.0	Light gray–gray	Layered
7H-6, 51–52	1.0	Light gray	Layered
7H-6, 88–89	1.0	Light gray	Layered
7H-6, 112–113	1.0	Light gray	Layered
8H-1, 34–38	4.0	White	Layered
8H-2, 131–133	0.7	Light gray	Patched
8H-5, 3–5	2.0	Light gray	Layered
8H-6, 18–20	2.0	Light gray	Layered
8H-6, 23.5–25	1.5	Light gray	Layered
8H-6, 56–59	1.0	Light gray	Patched
8H-6, 80–82	2.0	White	Layered
8H-7, 46–49	3.0	Light gray	Layered
9H-1, 124–126	2.0	Gray	Layered
9H-3, 39–41	2.0	Light gray	Layered
9H-5, 56–62	6.0	Light gray	Layered
9H-6, 85–86	1.0	Gray	Layered
10H-1, 43.5–47	1.2	Light gray	Patched
10H-3, 106–109.5	3.5	Light gray	Layered
11H-1, 42–46	1.3	Light gray–gray	Patched
11H-6, 91–94.5	1.2	Gray	Patched
11H-6, 112–115	3.0	White	Patched
13H-3, 29.5–31	0.5	White	Patched
13H-5, 7–22	15.0	White	Layered
14H-2, 86.5–91.5	5.0	Light gray	Layered
14H-2, 99.5–101	0.5	Light gray	Patched
19H-4, 55–61	6.0	Light gray	Layered
20H-1, 81–84	3.0	Light gray	Layered
20H-1, 127–130	3.0	Gray	Layered
20H-3, 93–95	2.0	Gray	Layered
20H-6, 77–94	17.0	White–light gray	Layered

Table T3. XRD analysis of bulk samples, Site U1423.

Core section, interval (cm)	Top depth CSF-A (m)	Smectite (counts)	Illite (counts)	Kaolinite + chlorite (counts)	Opal-A (counts)	Quartz (counts)	K-feldspar (counts)	Plagioclase (counts)	Calcite (counts)	Halite (counts)	Pyrite (counts)
346-U1423A-											
1H-2, 100.0–101.0	2.5	304	562	474	0	4033	301	718	977	299	343
2H-1, 122.0–123.0	8.52	250	176	164	9	3787	0	713	113	284	68
3H-1, 90.0–91.0	17.7	194	545	319	10	5193	294	777	365	177	0
4H-1, 52.0–53.0	26.82	276	606	431	0	5222	287	702	130	279	0
5H-1, 91.0–92.0	36.71	288	383	247	0	3422	0	440	2191	240	81
6H-1, 95.0–96.0	46.25	212	481	357	4	5017	220	680	91	241	53
7H-1, 81.0–82.0	55.61	154	275	227	46	4393	228	593	0	221	87
8H-1, 86.0–87.0	65.16	232	208	150	44	3616	0	664	0	254	84
8H-5, 74.5–75.5	71.045	215	186	150	50	4006	0	692	0	187	132
9H-1, 133.0–134.0	75.13	238	505	381	30	4718	279	615	0	198	124
10H-1, 108.0–109.0	84.38	202	343	254	15	4490	200	677	0	194	0
11H-1, 83.0–84.0	93.63	210	454	335	5	4640	261	702	0	239	0
12H-1, 90.0–91.0	103.2	210	363	291	33	4079	180	485	0	286	90
13H-2, 93.0–94.0	114.23	101	161	135	93	3435	184	420	0	330	105
14H-1, 78.0–79.0	122.08	79	255	99	139	2344	124	361	0	409	0
15H-1, 86.0–87.0	131.66	110	143	140	39	3095	150	523	0	267	68
16H-1, 96.0–97.0	141.26	150	232	150	79	3021	130	487	0	337	75
17H-1, 74.0–75.0	150.54	123	190	166	121	2599	130	368	0	450	106
18H-1, 86.0–87.0	159.96	166	148	136	55	3416	150	404	0	358	93
19H-1, 88.0–89.0	169.48	212	260	190	48	3721		462	0	284	78
20H-1, 104.0–105.0	179.14	143	123	138	90	2735		504	0	306	81
21H-1, 87.0–88.0	188.47	111	151	122	153	2485	129	356	0	340	103
22H-1, 84.0–85.0	197.94	160	195	193	174	2342	91	424	0	389	86

Table T4. Datum table, Site U1423.

Core, section, interval (cm)		Event		Age	Depth CSF-A (m)				Depth CCSF-A (m)			
Top	Bottom	type	Bioevents and epoch boundaries	(Ma)	Top	Bottom	Midpoint	±	Top	Bottom	Midpoint	±
346-U1423A-	346-U1423A-											
NA	1H-CC	R	LO *Lychnocanoma sakaii*	0.05	0	7.22	3.61	3.61	0	7.22	3.61	3.61
1H-CC	2H-CC	R	LO *Amphimelissa setosa*	0.08	7.22	16.97	12.10	4.88	7.22	17.44	12.33	5.11
2H-CC	3H-CC	R	LO *Spongodiscus* sp.	0.29	16.97	26.58	21.78	4.81	17.44	27.44	22.44	5.00
3H-CC	4H-CC	D	LO *Proboscia curvirostris*	0.3	26.58	36.07	31.33	4.75	27.44	37.61	32.52	5.08
4H-CC	5H-1W, 113–114	CN	LO *Pseudoemiliania lacunosa*	0.44	36.07	36.93	36.50	0.43	37.61	39.07	38.34	0.73
4H-CC	5H-4W, 77–78	PF	LO *Neogloboquadrina kagaensis* group	0.70	36.07	41.07	38.57	2.50	37.61	43.21	40.41	2.80
5H-CC	6H-CC	D	LO *Actinocyclus oculatus*	1.0	45.38	54.91	50.15	4.77	47.52	57.30	52.41	4.89
6H-CC	8H-CC	CN	Br *Gephyrocapsa* >4 µm	1.04	54.91	74.14	64.53	9.61	57.30	77.74	67.52	10.22
6H-CC	9H-2W, 75–76	CN	LO *Calcidiscus macintyrei*	1.6	54.91	76.05	65.48	10.57	57.30	79.89	68.59	11.29
7H-CC	8H-CC	D	LO *Neodenticula koizumii*	2.0	64.64	74.14	69.39	4.75	67.64	77.74	72.69	5.05
8H-CC	10H-CC	R	LO *Axoprunum acquilonium*	1.2–1.7	74.14	93.17	83.66	9.52	77.74	97.36	87.55	9.81
Pliocene/Pleistocene boundary				2.59								
12H-CC	13H-CC	D	LO *Neodenticula kamtschatica*	2.6–2.7	112.06	121.70	116.88	4.82	116.07	126.60	121.33	5.27
12H-CC	13H-CC	R	FO *Cycladophora davisiana*	2.7	112.06	121.70	116.88	4.82	116.07	126.60	121.33	5.27
14H-CC	15H-CC	D	FO *Neodenticula koizumii*	3.4–3.9	131.19	140.51	135.85	4.66	136.17	145.95	141.06	4.89
18H-CC	19H-CC	R	FO *Hexacontium parviakitaensis*	3.9–4.3	168.88	178.34	173.61	4.73	175.71	185.82	180.77	5.06
19H-CC	20H-CC	R	LO *Dictyophimus bullatus*	3.9–4.3	178.34	187.73	183.04	4.69	185.82	195.35	190.58	4.76
19H-CC	20H-CC	R	RD *Siphocampe arachnea* group	4.46	178.34	187.73	183.04	4.69	185.82	195.35	190.59	4.76
21H-CC	22H-CC	R	FO *Dictyophimus bullatus*	4.4	197.22	206.97	202.10	4.88	205.13	215.06	210.10	4.96
346-U1423B-	346-U1423B-											
2H-4W, 69–70	4H-4W, 53–54	CN	FO *Emiliania huxleyi*	0.29	9.29	28.10	18.70	9.41	9.73	29.26	19.49	9.77
5H-7W, 32–33	6H-3W, 132–133	PF	LO *Neogloboquadrina kagaensis* group	0.70	41.92	46.42	44.17	2.25	43.35	48.56	45.95	2.60
15H-CC	16H-CC	D	FO *Neodenticula koizumii*	3.4–3.9	132.8	142.40	137.60	4.80	138.69	147.96	143.32	4.63
22H-CC	23H-CC	R	FO *Dictyophimus bullatus*	4.4	192.33	201.90	197.12	4.79	199.54	209.35	204.44	4.90
25H-CC	26H-CC	R	RI *Siphocampe arachnea* group	4.71	220.78	230.10	225.44	4.66	228.40	237.72	233.06	4.66
27H-CC	28H-CC	D	LO *Thalassiosira jacksonii*	4.81	239.95	249.47	244.71	4.76	247.57	257.09	252.33	4.76

NA = not applicable. R = radiolarian, PF = planktonic foraminifer, CN = calcareous nannofossil, D = diatom. LO = last occurrence, FO = first occurrence, Br = base reentrance, RD = rapid decrease, RI = rapid increase.

Table T5. Preservation and estimated abundance of calcareous nannofossils, Site U1423. (Continued on next page.)

Core, section, interval (cm)	Top depth CSF-A (m)	Bottom depth CSF-A (m)	Preservation	Abundance	*Braarudosphaera bigelowii*	*Calcidiscus leptoporus*	*Calcidiscus macintyrei*	*Coccolithus pelagicus*	*Cyclicargolithus floridanus*	*Emiliania huxleyi*	*Gephyrocapsa caribbeanica*	*Gephyrocapsa muellerae*	*Gephyrocapsa oceanica* s.s.	*Gephyrocapsa* spp. (>4 µm)	*Gephyrocapsa* spp. (<4 µm)	*Helicosphaera carteri*	*Helicosphaera sellii*	*Helicosphaera* spp.	*Pontosphaera japonica*	*Pontosphaera multipora*	*Pontosphaera* spp.	*Pseudoemiliania lacunosa*	*Reticulofenestra minuta*	*Reticulofenestra minutula*	*Reticulofenestra* spp.	*Syracosphaera* spp.
346-U1423A-																										
1H-CC	7.22	7.26	P	R											R											
2H-CC	16.97	17.02		B																						
3H-3, 48–49	20.28	20.29		B																						
3H-5, 140–141	24.20	24.21		B																						
3H-7, 59–60	26.39	26.40		B																						
3H-CC	26.58	26.63		B																						
4H-1, 50–51	26.80	26.81	M	R				R				R	R		R											
4H-4, 92–93	31.67	31.68	G	D				R							D											
4H-7, 27–28	35.52	35.53		B																						
4H-CC	36.07	36.12	G	A	R			C			A		F		A								C			F
5H-1, 113–114	36.93	36.94	G	A	R			R					F	F	D							R	C			
5H-4, 53–54	40.83	40.84	P	R	R			R			R				R											
5H-7, 39–40	45.00	45.01	M	F				F					F	F	R											
5H-CC	45.38	45.43	M	R				R			R		R													
6H-1, 70–71	46.00	46.01	M	F	R			F			F		R	F	F											
6H-2, 94–95	47.74	47.75	M	C	R			F	*			R	F		A								D		F	
6H-4, 22–23	49.97	49.98		B																						
6H-CC	54.91	54.96	M	F		R		F	*				R	R	F			R								
7H-CC	64.64	64.69		B																						
8H-CC	74.14	74.19		B																						
9H-2, 75–76	76.05	76.06	M	A		C	R	A			F				C					R			F		F	
9H-CC	83.60	83.64		B																						
10H-5, 18–19	89.48	89.49		B																						
10H-CC	93.17	93.21		B																						
11H-5, 91–92	99.71	99.72		B																						
11H-7, 36–37	102.16	102.17		B																						
11H-CC	102.55	102.60		B																						
12H-6, 119–120	110.99	111.00		B																						
12H-CC	112.06	112.11		B																						
13H-3, 70–71	115.50	115.51		B																						
13H-7, 40–41	121.20	121.21		B																						
13H-CC	121.70	121.74		B																						
14H-6, 59–60	129.39	129.40		B																						
14H-CC	131.19	131.24		B																						
15H-CC	140.51	140.56		B																						
16H-2, 98–99	142.78	142.79	M	A	R	R		C						C	A		*		R				F	F		
16H-CC	150.20	150.24	M	R				R							R								R	R		
17H-1, 12–13	149.92	149.93		B																						
17H-CC	159.12	159.17		B																						
18H-CC	168.88	168.93		B																						
19H-CC	178.34	178.39		B																						
20H-CC	187.73	187.77		B																						
21H-CC	197.22	197.27		B																						
22H-CC	206.97	207.02		B																						
346-U1423B-																										
1H-2, 80–81	2.30	2.31	M	R	R						R				R											
2H-4, 69–70	9.29	9.30	M	F	R			F		F			R		F											
3H-5, 80–81	20.40	20.41		B																						
4H-4, 53–54	28.10	28.11	M	R				R			R				R											
4H-6, 98–99	31.55	31.56	G	D				R							D											
5H-3, 85–86	36.45	36.46	M	C	R	R		R			R	F	F		C	R							C			R
5H-4, 135–136	38.45	38.46	M	C				C					F		A								C	F		
5H-7, 15–16	41.75	41.76	M	R	R			F			R															
5H-7, 32–33	41.92	41.93	M	F	R			F							R									R		
6H-3, 132–133	46.42	46.43	P	F				F					F		F											
7H-1, 132–133	52.92	52.93	M	F				F					R						R					F		
7H-2, 45–46	53.55	53.56	G	D											D									A		
9H-2, 50–51	72.60	72.61	M	F				C							R						F			F		
9H-5, 75–76	77.35	77.36	M	A		F		C							C	R			F					R		

Table T5 (continued).

Core, section, interval (cm)	Top depth CSF-A (m)	Bottom depth CSF-A (m)	Preservation	Abundance	*Braarudosphaera bigelowii*	*Calcidiscus leptoporus*	*Calcidiscus macintyrei*	*Coccolithus pelagicus*	*Cyclicargolithus floridanus*	*Emiliania huxleyi*	*Gephyrocapsa caribbeanica*	*Gephyrocapsa muellerae*	*Gephyrocapsa oceanica* s.s.	*Gephyrocapsa* spp. (>4 µm)	*Gephyrocapsa* spp. (<4 µm)	*Helicosphaera carteri*	*Helicosphaera sellii*	*Helicosphaera* spp.	*Pontosphaera japonica*	*Pontosphaera multipora*	*Pontosphaera* spp.	*Pseudoemiliania lacunosa*	*Reticulofenestra minuta*	*Reticulofenestra minutula*	*Reticulofenestra* spp.	*Syracosphaera* spp.
10H-2, 130–131	82.86	82.87		B																						
15H-1, 75–76	128.35	128.36		B																						
15H-CC	132.80	132.85		B																						
16H-3, 85-86	136.45	136.46	M	R											R											
16H-CC	142.41	142.46		B																						
17H-CC	151.91	151.95	M	R											F											
22H-CC	192.33	192.38		B																						
23H-CC	201.90	201.95		B																						
24H-CC	211.42	211.47		B																						
25H-CC	220.78	220.83		B																						
26H-CC	230.10	230.15		B																						
27H-CC	239.95	240.00		B																						
28H-CC	249.47	249.52		B																						
346-U1423C-																										
2H-CC	123.79	123.84		B																						
3H-CC	133.37	133.42		B																						
6H-CC	159.95	160.00		B																						
8H-CC	171.02	171.05		B																						
9H-CC	180.86	180.91		B																						

* = indicates species not in situ. Preservation: G = good, M = moderate, P = poor. Abundance: D = dominant, A = abundant, C = common, F = few, R = rare, B = barren. Shaded intervals = barren.

Table T6. Preservation and estimated abundance of radiolarians, Holes U1423A and U1423B.

Core, section	Top depth CSF-A (m)	Bottom depth CSF-A (m)	Preservation	Abundance	*Actinomma boreale*	*Actinomma leptodermum*	*Amphimelissa setosa*	*Axoprunum acquilonium*	*Carpocanarium papillosum*	*Ceratospyris borealis*	*Cornutella profunda*	*Cycladophora cornutoides*	*Cycladophora davisiana*	*Cycladophora nakasekoi*	*Cycladophora sakaii*	*Cyrtopera languncula*	*Dictyocoryne profunda*	*Dictyocoryne truncatum*	*Dictyophimus bullatus*	*Didymocyrtis tetrathalamus tetrathalamus*	*Euchitonia furcata*	*Hexacontium parviakitaensis*	*Hymeniastrum euclidis*	*Larcopyle polyacantha* group	*Larcopyle pylomaticus*	*Lychnocanoma sakaii*	*Octopyle/Tetrapyle* group	*Peripyramis circumtexta*	*Peripyramis woodringi*	*Phorticium pylonium* group	*Plectacantha oikiskos*	*Pseudodictyophimus gracilipes*	*Siphocampe arachnea* group	*Sphaeropyle antarctica*	*Sphaeropyle langii*	*Sphaeropyle robusta*	*Spongaster tetras tetras*	*Spongodiscus* sp.	*Spongopyle osculosa*	*Stichocorys delmontensis*	*Stichocorys peregrina*	*Stichocorys* spp. group	*Stylochlamydium venustum*	*Thecosphaera japonica*	*Thecosphaera pseudojaponica*
346-U1423A-																																											
1H-CC	7.22	7.26	G	F						R			A					R					R		F	F																	
2H-CC	16.97	17.02	M	A			C						F				P			P			C		A																	
3H-CC	26.58	26.63	M	R					P	F			R										R		F			F			R				F					R		
4H-CC	36.07	36.12	M	A			F			F				P									A			F				F					P	A						
5H-CC	45.38	45.43	G	C						A			R		P							P								F						F						
6H-CC	54.91	54.96	G	A								P	A				F	R					C	F				R		F	R											
7H-CC	64.64	64.69	G	A	R	F				C			C				F	F		R	P		R	F		F				F	P	P			A						
8H-CC	74.14	74.19	G	A			C			A									P					C				P		F									A		
9H-CC	83.60	83.64	P	R						C				P	P																								P		
10H-CC	93.17	93.21	G	A	F	F		C		A			A					P						C	F		R	P	C			F	R								
11H-CC	102.55	102.60	G	A	R	C		F		C						P									C			R	C			R						F	F	
12H-CC	112.06	112.11	G	A						P	C	R	F		F			P						C	C			P	P			R						F	P	
13H-CC	121.70	121.74	G	A						F	F				C									F	F							F					F	C	P	
14H-CC	131.19	131.24	G	A							F				C							R			F			P	R		P	F							F	
15H-CC	140.51	140.56	G	C				P			C				F							F		F	P							F							F	
16H-CC	150.20	150.24	G	C				R			R				F							C																	F	
17H-CC	159.12	159.17	G	C				R			C				F	P						C		F	F				F			F							F	R	R
18H-CC	168.88	168.93	G	A				F			F				C							F						R				F		P	P				F	F	
19H-CC	178.34	178.39	G	C				P			R				C													R				C					R		P	P
20H-CC	187.73	187.77	G	A				P							A				P						C			P	P			A							P	P	
21H-CC	197.22	197.27	G	A				P	P		P				C				R													A							P		
22H-CC	206.97	207.02	G	A				P			R				A																	A							P		P
346-U1423B-																																										
22H-CC	192.33	192.38	G	A							P				A				P						P				R			A					P			R		
23H-CC	201.90	201.95	G	A							R				C										P							A					P			R		P
24H-CC	211.42	211.47	G	A				R			F				A	P								F	P							A			P			R		F	R	
25H-CC	220.78	220.83	G	A				R			F				C										R							A			C			P		C	P	
26H-CC	230.10	230.15	G	A				F			F				C										R							F			P		F	A	C			
27H-CC	239.95	240.00	G	A				P			F				C										R				P			F							F		
28H-CC	249.47	249.52	G	A				P			C				C									F	F			P				R						P		C		R

Preservation: G = good, M = moderate, P = poor. Abundance: A = abundant, C = common, F = few, R = rare, P = present.

Table T7. Preservation and estimated abundance of diatoms, Holes U1423A and U1423B.

Core, section	Top depth CSF-A (m)	Bottom depth CSF-A (m)	Preservation	Abundance	*Actinocyclus curvatulus*	*Actinocyclus oculatus*	*Actinoptychus senarius*	*Aulacoseira* spp.	*Azpeitia endoi*	*Azpeitia nodulifera*	*Chaetoceros* spp. and similar spores	*Cocconeis costata*	*Cocconeis scutellum*	*Coscinodiscus marginatus*	*Coscinodiscus oculus-iridis*	*Coscinodiscus radiatus*	*Denticulopsis dimorpha*	*Neodenticula kamtschatica*	*Neodenticula koizumii*	*Neodenticula seminae*	*Paralia sulcata*	*Proboscia curvirostris*	*Rhaphoneis amphiceros*	*Rhaphoneis miocenica*	*Rhizosolenia bergonii*	*Rhizosolenia styliformis*	*Shionodiscus oestrupii*	*Stephanopyxis turris*	*Stephanopyxis* spp.	*Thalassionema nitzschioides*	*Thalassiosira eccentrica*	*Thalassiosira jacksonii*	*Thalassiosira leptopus*	*Thalassiosira lineata*	*Thalassiosira manifesta*	*Thalassiosira nidulus*	*Thalassiosira pacifica*	*Thalassiosira trifulta*	*Thalassiothrix frauenfeldii*	Comments
346-U1423A-																																								
1H-CC	7.22	7.26	G	F					F	F	F												F				F			F			F					F	
2H-CC	16.97	17.02	G	C			F		F		C									F	F		R	R		F	F			C				F						Spicules
3H-CC	26.58	26.63	G	F			R				R						R	F	R											F			R							Silicoflagellates
4H-CC	36.10	36.12	G	C							Ma	R	R	R		R	R					C	F	F		R	F		R	C	R			R				R		Spicules
5H-CC	45.38	45.43	G	A	R		R	R	R		A							R				C					R		R	R			R							Silicoflagellates, *Chaetoceros* branches
6H-CC	54.91	54.96	G	F		C		R			Ma				R	R	R	R	R	R			R				R			C										Phytoliths, spicules, *Chaetoceros* branches
7H-CC	64.60	64.69	G	F	F						Ma	R	R			R	R	R	R											R			R							*Chaetoceros* branches
8H-CC	74.14	74.19	G	D		C			F		F			R			R		C	C							C		F	C			C				R			*Chaetoceros* branches, silicoflagellates
9H-CC	83.60	83.64	G	C	R						R						R	F	R	R					R		C			R	R					R				Big *Coscinodiscus marginatus*, silicoflagellates, *Chaetoceros* branches
10H-CC	93.17	93.21	G	C	R	A					F	R				R		F	C	F							C			R	R									Spicules
11H-CC	103.00	102.60	G	C					R		F							F	C	R		C					C		R											*Chaetoceros* branches
12H-CC	112.10	112.11	G	D							Ma			F				F	C	R		R				R	C		R											Big *Coscinodiscus marginatus*, spicules
13H-CC	121.70	121.74	G	A	F		F			R	F			F				C	C	R							C		F	C	R		R		R		R			*Chaetoceros* branches
14H-CC	131.20	131.24	G	D	R				R		Ma			F			R	A	A								C		C	C	R				R					Big *Coscinodiscus marginatus*, *Chaetoceros* vegetative cell remains
15H-CC	140.50	140.56	G	D		R					A	R		R			F	A									F		R	C	R									
16H-CC	150.20	150.24	G	A							F	R				R	F	F								R	F		F	C				R						Spicules, *Chaetoceros* branches
17H-CC	159.12	159.17	G	D			R				F	R	R	F				A									C			C	R		R		R		R			Big *Coscinodiscus marginatus*, *Chaetoceros* branches
18H-CC	168.88	168.93	G	A			C				F	R		F				A									F		C	R	R				R					Big *Coscinodiscus marginatus*, silicoflagellates, *Chaetoceros* branches
19H-CC	178.34	178.39	G	A							R			F			F	A			R						F			R										Big *Coscinodiscus marginatus*, silicoflagellates, spicules
20H-CC	187.73	187.77	G	D			R		R		C			C			R	Ma									F		R	C		R								Silicoflagellates, spicules
21H-CC	197.20	197.27	G	D		R	R				C	F		C				Ma									C		R	C					R					Big *Coscinodiscus marginatus*, silicoflagellates, *Chaetoceros* branches
22H-CC	206.97	207.02	G	A			R				R	R		R			R	Ma									F		F	R	R						R			Big *Coscinodiscus marginatus*, *Chaetoceros* vegetative cell remains
346-U1423B-																																								
15H-CC	132.80	132.85	G	A							C			F			F	A	C								F	r		A			R							Spicules
16H-CC	142.41	142.46	G	C							C		F	A			R	A	R								C	F								R	R				Spicules
17H-CC	151.91	151.95	G	C			R		R		C	R		C		R	R	A									C	r		C	R									*Chaetoceros* branches
22H-CC	192.33	192.38	G	A	R	R	R				R	R	R				R	C			F						F	R		C		R				R				*Chaetoceros* branches, silicoflagellates, spicules
23H-CC	201.90	202.00	G	A			C		R		R	R		C		R	R	A									C	F		R	R		R							Silicoflagellates, spicules
24H-CC	211.42	211.47	G	C	R		C		R		R	R		F			F	A					R				R	R												Spicules
25H-CC	221.00	220.83	G	C			A		R		R	R		F			F	C									A	R		F										Spicules
26H-CC	230.10	230.15	G	C			R		R		F	R	R	R			F	A			R						A	R		F					R	R				*Chaetoceros* branches, silicoflagellates, spicules
27H-CC	240.00	240.00	G	A	F		R				R			F				A			R						A	R					R							*Chaetoceros* branches, silicoflagellates, spicules
28H-CC	249.47	249.52	G	D	R						R			C				A			R						A	F		R	R	C	R							*Chaetoceros* branches, silicoflagellates, spicules

Preservation: G = good. Abundance: Ma = massive, D = dominant, A = abundant, C = common, F = few, R = rare.

Table T8. Preservation and estimated abundance of planktonic foraminifers, Holes U1423A and U1423B. (Continued on next page.)

Core, section, interval (cm)	Top depth CSF-A (m)	Bottom depth CSF-A (m)	Preservation	Abundance	% Planktonic foraminifers	*Globigerina bulloides*	*Globigerina umbilicata*	*Globigerina quinqueloba*	*Globigerina* sp.	*Globorotalia praeinflata*	*Neogloboquadrina* cf. *asanoi*	*Neogloboquadrina dutertrei*	*Neogloboquadrina incompta*	*Neogloboquadrina kagaensis* and *Neogloboquadrina inglei*	*Neogloboquadrina pachyderma*	*Neogloboquadrina pachyderma* (d)	*Neogloboquadrina pachyderma* (s)	*Neogloboquadrina* sp.	*Orbulina universa*	Total number of planktonic foraminifers	Total planktonic foraminifers/10 cm^3
346-U1423A-																					
1H-CC	7.22	7.26	G	A	99	25	3					2				2	68			100	33.3
2H-CC	16.97	17.02		A	20	14										2	6			22	7.33
3H-CC	26.58	26.63		A	99	30							2			1	67			100	33.3
4H-CC	36.07	36.12	G	A	95	33											72			105	35
5H-4, 77–78	41.07	41.08	M	A	100	38	9	4	1			2		4		3	46			107	1070
5H-CC	45.38	45.43	P	A	88	22	1									1	76			100	33.3
6H-CC	54.91	54.96	G	A	88	49	6					1		8		2	27	1		94	31.3
7H-CC	64.64	64.69	M	R	80	12	3										4			19	6.33
8H-CC	74.14	74.19	M	R	100	3											2			5	1.67
9H-CC	83.60	83.64		B																0	0
10H-5, 18–19	89.48	89.49		B																0	0
10H-CC	93.17	93.21		B																0	0
11H-5, 91–92	99.71	99.72		B																0	0
11H-7, 36–37	102.16	102.17	P	R														1		1	10
11H-CC	102.55	102.60		B																0	0
12H-6, 119–120	110.99	111.00		B																0	0
12H-CC	112.06	112.11		B																0	0
13H-3, 70–71	115.50	115.51		B																0	0
13H-CC	121.70	121.74		B																0	0
14H-CC	131.19	131.24		B																0	0
15H-CC	140.51	140.56		B																0	0
16H-2, 98–99	142.78	142.79	M	R	100	6		7			1		1	1	1	4	1			22	220
16H-CC	150.20	150.24	G	A	70	25	30	3			10	18		37		20			3	146	48.7
17H-1, 20–21	150.00	150.01		B																0	0
18H-CC	168.88	168.93		B																0	0
19H-CC	178.34	178.39		B																0	0
20H-CC	187.73	187.77		B																0	0
21H-CC	197.22	197.27		B																0	0
22H-CC	206.97	207.02	G	R	18	3											1			4	1.33
346-U1423B-																					
4H-4, 53–54	28.10	28.11	M	D	100	21										1	77			99	990
4H-6, 64–65	31.21	31.22	M	D	90	30	1	2					2			1	75			111	1110
4H-6, 98–99	31.55	31.56	M	D	100	20	5	17				1	2			2	53			100	1000
5H-3, 85–86	36.45	36.46	M	D	100	38	3	4				2					55			102	1020
5H-4, 135–136	38.45	38.46	G	D	100	1							1			1	97			100	1000
5H-7, 32–33	41.92	41.93	G	D	100	65	1	1					1			1	28			97	970
6H-3, 132–133	46.42	46.43	G	D	100	48						1	1	1			36			87	870
6H-5, 48–49	48.58	48.59	G	D	99	30	2	3						2		3	55			95	950
7H-1, 132–133	52.92	52.93	G	D	100	43	6							5		2	44			100	1000
7H-2, 45–46	53.55	53.56	G	D	100	40	6	5				7		20		2	23	1		104	1040
8H-2, 118–119	63.78	63.79	M	D	100	40	3							6		3	46			98	980
8H-6, 43–44	69.03	69.04	G	D	88	49	4							5		6	37			101	1010
9H-2, 50–51	72.6	72.61	P	D	95	51	1	3			3	2		21		5	2			88	880
9H-5, 75–76	77.35	77.36	P	F	100	2										2				4	40
10H-2, 130–131	82.86	82.87		B																0	0
15H-CC	132.80	132.85	M	A	81	32	7		1	19	4					6	13			82	27.3
16H-CC	142.41	142.46		B																0	0
17H-CC	151.91	151.95		B																0	0

Table T8 (continued).

Core, section, interval (cm)	Top depth CSF-A (m)	Bottom depth CSF-A (m)	Preservation	Abundance	% Planktonic foraminifers	*Globigerina bulloides*	*Globigerina umbilicata*	*Globigerina quinqueloba*	*Globigerina* sp.	*Globorotalia praeinflata*	*Neogloboquadrina* cf. *asanoi*	*Neogloboquadrina dutertrei*	*Neogloboquadrina incompta*	*Neogloboquadrina kagaensis* and *Neogloboquadrina inglei*	*Neogloboquadrina pachyderma*	*Neogloboquadrina pachyderma* (d)	*Neogloboquadrina pachyderma* (s)	*Neogloboquadrina* sp.	*Orbulina universa*	Total number of planktonic foraminifers	Total planktonic foraminifers/10 cm^3
22H-CC	192.33	192.38		B																0	0
23H-CC	201.90	201.95		B																0	0
24H-CC	211.42	211.47		B																0	0
25H-CC	220.78	220.83		B																0	0
26H-CC	230.10	230.15		B																0	0
27H-CC	239.95	240.00		B																0	0
28H-CC	249.47	249.52		B																0	0
346-U1423C-																					
2H-CC	123.79	123.84		B																0	0
3H-CC	133.37	133.42		B																0	0
4H-CC	142.65	142.70	P	R	40	8	6			4	0	2		9				3		32	10.7
6H-CC	159.95	160.00		B																0	
8H-CC	171.02	171.05		B																0	
9H-CC	180.86	180.91		B																0	

Numbers of specimens in core catcher samples refer to ~30 cm^3, whereas numbers in core samples refer to 1 cm^3. Preservation: G = good, M = moderate, P = poor. Abundance: D = dominant, A = abundant, F = few, R = rare, B = barren. Shaded intervals = barren.

Table T9. Benthic foraminifers, Site U1423. This table is available in an **oversized format.**

Table T10. Calcium carbonate, total carbon (TC), total organic carbon (TOC), and total nitrogen (TN) contents on interstitial water squeeze cake sediment samples, Site U1423.

Core, section, interval (cm)	Top depth CSF-A (m)	Calcium carbonate (wt%)	TC (wt%)	TOC (wt%)	TN (wt%)
346-U1423A-					
1H-1, 145–150	1.45	1.14	2.25	2.11	0.31
1H-4, 145–150	5.95	0.50	0.40	0.34	0.15
2H-1, 145–150	8.75	0.86	0.27	0.17	0.15
2H-4, 145–150	13.25	0.76	1.00	0.91	0.22
3H-1, 145–150	18.25	0.20	1.18	1.15	0.22
3H-4, 145–150	22.75	0.24	0.42	0.39	0.14
4H-1, 140–145	27.70	0.17	2.35	2.33	0.31
4H-4, 145–150	32.20	0.39	0.75	0.71	0.19
5H-1, 145–150	37.25	1.14	2.55	2.42	0.31
5H-4, 145–150	41.75	14.27	2.79	1.08	0.19
6H-1, 145–150	46.75	0.42	0.89	0.84	0.21
6H-4, 145–150	51.20	0.65	0.58	0.50	0.16
7H-1, 145–150	56.25	0.88	0.55	0.44	0.18
7H-4, 145–150	60.75	0.25	0.46	0.43	0.17
8H-1, 145–150	65.75	0.26	1.84	1.81	0.26
8H-4, 145–150	70.25	0.94	0.39	0.27	0.13
9H-1, 145–150	75.25	0.32	2.13	2.09	0.26
9H-4, 145–150	79.75	0.40	0.46	0.41	0.16
10H-1, 145–150	84.75	0.29	0.27	0.23	0.15
10H-4, 145–150	89.25	0.26	0.39	0.36	0.15
11H-1, 145–150	94.25	0.33	0.47	0.43	0.17
11H-4, 145–150	98.75	0.21	0.74	0.71	0.18
12H-1, 145–150	103.75	0.32	1.31	1.27	0.22
12H-4, 145–150	108.25	0.31	0.48	0.44	0.17
13H-1, 145–150	113.25	0.26			
13H-4, 145–150	117.75	0.27	0.56	0.52	0.17
14H-1, 145–150	122.75	0.26	0.44	0.41	0.15
15H-1, 145–150	132.25	0.32	0.53	0.49	0.18
16H-1, 145–150	141.75	0.26	0.72	0.69	0.19
17H-1, 145–150	151.25	0.27			
18H-1, 145–150	160.55	0.31	0.51	0.47	0.17
19H-1, 145–150	170.05	0.27	0.51	0.48	0.16
20H-1, 145–150	179.55	0.27	0.41	0.38	0.14
21H-1, 145–150	189.05	0.41	0.55	0.50	0.14
22H-1, 145–150	198.55	0.27	0.48	0.45	0.15
346-U1423B-					
23H-3, 145–150	196.55	0.21	0.65	0.63	0.17
24H-3, 145–150	206.05	0.29	0.41	0.38	0.15
25H-3, 145–150	215.55	0.27	0.49	0.45	0.16
26H-3, 145–150	225.05	0.23	0.61	0.58	0.16
27H-3, 145–150	234.55	0.28	0.52	0.49	0.16
28H-3, 145–150	244.05	0.12			

Blank cells = not analyzed.

Table T11. Interstitial water geochemistry, Site U1423.

Core, section, interval (cm)	Top depth CSF-A (m)	Sample type	Volume squeezed (mL)	Alkalinity (mM) Titration	pH ISE	Salinity (‰) Refract	Cl^- (mM) Titration	Cl^- (mM) IC	SO_4^{2-} (mM) IC	Br^- (mM) IC	Na (mM) ICP	Ca (mM) ICP	Mg (mM) ICP	K (mM) ICP	B (µM) ICP	Ba (µM) ICP	Fe (µM) ICP	Li (µM) ICP	Mn (µM) ICP	Si (µM) ICP	Sr (µM) ICP	NH_4^+ (µM) Spec	PO_4^{3-} (µM) Spec	H_4SiO_4 (µM) Spec
346-U1423A-																								
1H-1, 0–5	0.00	ML	50	2.4	7.6	35	541	564	28.6	0.86	468	10.2	51.7	10.1	412	BD	BD	22	BD	112	87	93	1.4	98
1H-1, 145–150	1.45	IW-Sq	50	6.1	7.5	35	548	564	25.8	0.87	472	9.8	49.8	11.7	583	6	BD	23	123	627	93	315	54.4	566
1H-4, 145–150	5.95	IW-Sq	42	12.0	7.7	35	537	562	19.7	0.87	461	8.5	47.1	11.8	556	15	4.8	18	23	516	87	771	79.3	500
2H-1, 145–150	8.75	IW-Sq	40	15.5	7.7	34	535	560	16.2	0.87	458	7.7	45.6	11.4	524	26	2.6	17	19	588	88	1047	94.6	535
2H-4, 145–150	13.25	IW-Sq	40	19.0	7.6	34	538	559	12.3	0.87	436	6.5	42.5	10.8	586	12	BD	15	16	589	83	1080	98.7	612
3H-1, 145–150	18.25	IW-Sq	36	21.5	7.7	34	535				445	5.6	41.3	10.8	623	9	BD	18	9	625	88	1521	102.3	599
3H-4, 145–150	22.75	IW-Sq	40	24.4	7.6	34	536	557	6.0	0.88	437	5.3	40.4	10.7	552	22	1.1	19	10	628	88	1761	105.6	620
4H-1, 140–145	27.70	IW-Sq	40	24.9	7.4	34	532	553	4.1	0.87	432	4.8	38.8	10.2	615	24	9.1	23	3	641	92	1946	105.3	665
4H-4, 145–150	32.20	IW-Sq	36	25.6	7.4	34	534	553	2.6	0.88	452	4.6	39.3	10.7	621	55	4.3	29	1	751	103	1852	101.8	720
5H-1, 145–150	37.25	IW-Sq	38	26.1	7.4	34	529	562	1.8	0.90	450	4.7	38.4	10.4	608	62	2.0	30	BD	750	107	2058	97.8	755
5H-4, 145–150	41.75	IW-Sq	42	27.1	7.4	34	535	560	1.0	0.90	438	4.7	37.0	10.2	651	229	6.7	36	BD	776	119	2201	93.5	747
6H-1, 145–150	46.75	IW-Sq	40	27.1	7.4	34	539				435	4.9	35.8	10.1	616	692	4.7	35	BD	736	120	2339	93.7	749
6H-4, 145–150	51.20	IW-Sq	42	27.7	7.4	34	542	562	0.6	0.90	436	5.0	35.4	10.0	629	1373	6.8	33	1	832	128	2346	76.7	804
7H-1, 145–150	56.25	IW-Sq	40			33					457	5.6	36.5	10.4	629	2455	3.7	32	BD	791	137	2352	69.9	813
7H-4, 145–150	60.75	IW-Sq	37	27.7	7.3	34	539				436	5.5	34.3	9.8	680	3375	5.1	32	BD	878	151	2185	63.9	845
8H-1, 145–150	65.75	IW-Sq	50			34		563	0.7	0.90	453	6.1	34.9	10.1	679	3453	2.9	31	1	848	147	2434	60.1	847
8H-4, 145–150	70.25	IW-Sq	44	27.3	7.4	34	540				470	6.4	35.4	10.5	763	4317	5.0	38	2	1024	172	2141	50.5	906
9H-1, 145–150	75.25	IW-Sq	40	26.4	7.4	34	541	563	0.4	0.91	467	6.6	34.5	10.3	758	4325	BD	38	3	912	162	2317	43.3	904
9H-4, 145–150	79.75	IW-Sq	50	26.3	7.5	34	543				471	7.0	34.5	10.2	653	4454	1.1	40	4	894	162	2337	38.6	899
10H-1, 145–150	84.75	IW-Sq	40	26.2	7.4	34	541				464	7.2	33.8	10.0	711	4606	4.6	45	7	933	167	2106	38.1	938
10H-4, 145–150	89.25	IW-Sq	44	25.8	7.4	33	543	567	0.4	0.92	468	7.4	33.4	10.1	743	4763	3.8	46	9	934	167	2233	38.0	959
11H-1, 145–150	94.25	IW-Sq	46	24.8	7.5	34	544	559	0.5	0.90	467	7.7	32.7	10.0	718	4775	BD	52	9	927	172	2144	34.2	933
11H-4, 145–150	98.75	IW-Sq	38	24.6	7.4	34	542	561	0.5	0.91	462	7.8	32.4	9.9	769	4967	BD	55	11	1006	177	2307	32.5	992
12H-1, 145–150	103.75	IW-Sq	48	23.9	7.3	33	544				468	8.0	32.3	9.6	830	5289	2.0	59	12	1039	184	2298	35.9	998
12H-4, 145–150	108.25	IW-Sq	52	23.9	7.7	33	543				466	8.1	31.6	9.7	831	5056	3.9	61	12	1111	177	2387	26.7	1095
13H-1, 145–150	113.25	IW-Sq	48	23.1	7.4	33	543	564	0.5	0.92	466	8.3	31.1	9.6	831	5048	2.4	65	12	1064	184	2271	24.9	1040
13H-4, 145–150	117.75	IW-Sq	56	22.3	7.4	33	537				470	8.4	30.9	9.6	827	4863	4.3	67	11	1116	180	2369	21.2	1065
14H-1, 145–150	122.75	IW-Sq	44	22.1	7.3	33	544	564	0.5	0.91	472	8.6	30.6	9.5	871	4737	2.1	72	11	1136	183	2004	21.8	1098
14H-4, 145–150	127.25	IW-Sq	52	21.8	7.3	33	545				467	8.6	30.0	9.5	866	4539	5.0	76	10	1145	184	2199	13.4	1115
15H-1, 145–150	132.25	IW-Sq	51	20.8	7.3	33	542															2172	12.8	1103
15H-4, 145–150	136.75	IW-Sq	43	21.0	7.5	33	542				468	8.8	29.5	9.4	827	4097	5.7	81	7	1105	182	2229	16.1	1115
16H-1, 145–150	141.75	IW-Sq	42	19.9	7.3	33	551				471	9.0	29.2	9.1	957	4159	2.0	92	7	1193	196	1994	6.6	1140
16H-4, 145–150	146.25	IW-Sq	48	20.0	7.1	33	543	560	0.4	0.91	472	9.0	29.1	9.2	904	3882	4.2	87	7	1201	185	2059	6.5	1220
17H-1, 145–150	151.25	IW-Sq	44	19.8	7.2	33	543	559	0.5	0.91	471	9.5	28.3	8.9	922	3612	3.7	92	14	1160	186	2463	7.4	1182
17H-4, 145–150	155.75	IW-Sq	47	19.8	7.3	33	545	563	0.4	0.92	461	9.6	28.0	8.9	910	3595	1.0	92	15	1183	186	1982	7.0	1204
18H-1, 145–150	160.55	IW-Sq	52	19.4	7.3	33	541				468	10.1	27.8	8.8	909	3391	1.1	95	18	1133	187	1970	5.2	1164
18H-4, 145–150	165.05	IW-Sq	47	19.1	7.5	33	544				464	10.2	27.2	8.7	872	3427	1.2	96	18	1109	189	2168	6.7	1122
19H-1, 145–150	170.05	IW-Sq	48	19.0	7.3	33	540				454	10.2	26.2	8.4	947	3291	1.6	98	23	1206	191	1890	5.0	1208
19H-4, 145–150	174.55	IW-Sq	56	19.0	7.3	32	547	560	0.4	0.91	462	10.5	26.3	8.6	1009	3462	2.0	104	25	1317	199	2235	9.0	1254
20H-1, 145–150	179.55	IW-Sq	45	18.5	7.3	33	541				468	11.0	26.5	8.5	970	3364	1.3	102	24	1273	196	1975	4.0	1260
20H-4, 145–150	184.05	IW-Sq	54	18.6	7.3	32	537	555	0.4	0.90	458	10.8	25.4	8.4	1026	3374	2.2	101	25	1291	195	1996	6.2	1302
21H-1, 145–150	189.05	IW-Sq	44	18.5	7.2	32	540				471	11.4	25.9	8.5	1118	3599	2.1	114	30	1563	217	1968	6.8	1434
21H-4, 145–150	193.55	IW-Sq	48	18.2	7.2	33	538	562	0.4	0.92	469	11.6	25.8	8.3	1009	3245	4.0	103	27	1377	196	1874	7.2	1420
22H-1, 145–150	198.55	IW-Sq	45	17.9	7.2	33	540				458	11.4	25.4	8.1	1028	3190	1.2	102	25	1315	196	2079	7.7	1368
22H-4, 145–150	203.05	IW-Sq	44	17.9	7.3	32	534				465	11.6	25.1	8.1	1089	3236	BD	109	27	1382	203	1910	5.0	1387
346-U1423B-																								
23H-3, 145–150	196.55	IW-Sq	36	18.0	7.2	33	541	550	0.5	0.90	466	11.8	25.1	8.0	1042	3079	1.8	103	25	1353	192	1916		1354
24H-3, 145–150	206.05	IW-Sq	40	17.9	7.3	32	544				461	11.8	25.1	8.2	1047	3150	BD	104	24	1339	198	1948		1344
25H-3, 145–150	215.55	IW-Sq	44	16.6	7.3	32	539				459	12.1	24.7	7.8	1004	2960	BD	106	25	1326	199	1866		1347
26H-3, 145–150	225.05	IW-Sq	40	16.3	7.1	32	540	560	0.6	0.91	457	12.3	24.0	7.8	1138	2953	1.2	113	29	1550	206	2030		1512
27H-3, 145–150	234.55	IW-Sq	52	16.0	7.2	32	539				466	12.9	24.1	7.5	1062	2812	BD	108	27	1412	198	1796		1452
28H-3, 145–150	244.05	IW-Sq	44	15.4	7.3	33	539				463	13.2	23.3	7.4	1072	2860	BD	110	25	1403	202	1776		1415

ML = mudline, IW-Sq = interstitial water from whole-round squeezing. ISE = ion-selective electrode, Refract = refractometer, IC = ion chromatograph, ICP = inductively coupled plasma–atomic emission spectroscopy, Spec = UV-VIS spectrophotometer. BD = below detection.

Table T12. Headspace (HS) gas concentrations, Site U1423.

Core, section, interval (cm)	Top depth CSF-A (m)	Sample type	Sediment volume (cm^3)	CH_4 (ppmv) measured	CH_4 (ppmv) normalized
346-U1423A-					
1H-2, 0–5	1.50	HS	4.00	7.95	9.94
1H-5, 0–5	6.00	HS	4.00	1.88	2.35
2H-2, 0–5	8.80	HS	2.00	1.73	4.33
2H-5, 0–5	13.30	HS	4.00	0.00	0.00
3H-2, 0–5	18.30	HS	4.00	3.42	4.28
3H-5, 0–5	22.80	HS	4.00	5.26	6.58
4H-2, 0–5	27.75	HS	3.60	24.41	33.90
4H-5, 0–5	32.25	HS	4.00	97.56	121.95
5H-2, 0–5	37.30	HS	4.00	155.76	194.70
5H-5, 0–5	41.80	HS	4.00	232.16	290.20
6H-2, 0–5	46.80	HS	4.00	350.17	437.71
6H-5, 0–5	51.25	HS	4.00	343.62	429.53
7H-2, 0–5	56.30	HS	3.20	665.77	1040.27
7H-5, 0–5	60.80	HS	4.80	1076.44	1121.29
8H-2, 0–5	65.80	HS	4.00	1377.24	1721.55
8H-5, 0–5	70.30	HS	3.00	1203.62	2006.03
9H-2, 0–5	75.30	HS	3.00	903.74	1506.23
9H-5, 0–5	79.80	HS	3.00	876.44	1460.73
10H-2, 0–5	84.80	HS	3.00	621.05	1035.08
10H-5, 0–5	89.30	HS	3.20	403.45	630.39
11H-2, 0–5	94.30	HS	3.00	253.79	422.98
11H-5, 0–5	98.80	HS	3.00	228.66	381.10
12H-2, 0–5	103.80	HS	3.00	308.96	514.93
12H-5, 0–5	108.30	HS	3.00	180.52	300.87
13H-2, 0–5	113.30	HS	3.00	105.75	176.25
13H-5, 0–5	117.80	HS	3.20	122.16	190.88
14H-2, 0–5	122.80	HS	2.60	30.20	58.08
14H-5, 0–5	127.30	HS	3.20	37.48	58.56
15H-2, 0–5	132.30	HS	3.20	13.72	21.44
15H-5, 0–5	136.80	HS	3.40	10.23	15.04
16H-2, 0–5	141.80	HS	2.80	6.78	12.11
16H-5, 0–5	146.30	HS	3.20	8.25	12.89
17H-2, 0–5	151.30	HS	3.00	6.49	10.82
17H-5, 0–5	155.80	HS	3.60	6.63	9.21
18H-2, 0–5	160.60	HS	3.00	3.93	6.55
18H-5, 0–5	165.10	HS	2.60	3.42	6.58
19H-2, 0–5	170.10	HS	3.00	3.45	5.75
19H-5, 0–5	174.60	HS	3.40	3.82	5.62
20H-2, 0–5	179.60	HS	3.20	2.87	4.48
20H-5, 0–5	184.10	HS	3.40	2.66	3.91
21H-2, 0–5	189.10	HS	3.80	3.39	4.46
21H-5, 0–5	193.60	HS	3.40	3.03	4.46
22H-2, 0–5	198.60	HS	2.80	2.78	4.96
22H-5, 0–5	203.10	HS	2.80	2.95	5.27
346-U1423B-					
23H-4, 0–5	196.60	HS	3.00	2.69	4.48
24H-4, 0–5	206.10	HS	3.20	2.29	3.58
25H-4, 0–5	215.60	HS	3.40	3.46	5.09
26H-4, 0–5	225.10	HS	3.20	2.63	4.11
27H-4, 0–5	234.60	HS	3.00	2.77	4.62
28H-4, 0–5	244.10	HS	2.60	3.46	6.65

Table T13. FlexIT tool core orientation data, Hole U1423A.

Core	Orientation angle (°)	Orientation standard (°)
346-U1423A-		
2H	91.03	1.45
3H	234.20	0.57
4H	295.28	0.62
5H	213.33	0.64
6H	152.64	0.39
7H	157.09	0.59
8H	28.57	0.28
9H	113.44	0.18
10H	16.54	0.35
11H	151.09	0.61
12H	32.27	4.44
14H	265.66	0.18
15H	215.65	0.22
16H	0.57	0.25
17H	114.14	0.11
18H	54.03	0.33
19H	143.18	0.24
20H	31.85	0.37
21H	332.78	0.23
22H	19.60	0.27

Table T14. Core disturbance intervals, Site U1423. (Continued on next page.)

Core, section	Comments on disturbance	Drilling disturbance intensity
346-U1423A-		
1H-2, 26–30	Soupy	High
1H-2, 125–125	Washed out ash layer?	
1H-3, 14–109	Disturbance and ash	
1H-4, 71–88	Ash mixed layer	
1H-4, 110–113	Flow-in	
1H-CC, 0–16		High
2H-1, 0–8	Slurry	Moderate
2H-CC, 0–16		Moderate to high
3H-1, 38–40	Disturbance	
3H-1, 66–71	Void	Destroyed
3H-1, 102–150	Crack	Moderate to high
3H-1, 120–122	Void	Destroyed
3H-5, 0–12	Disturbance	
3H-CC, 0–18		Moderate
4H-5, 118–150	Flow-in	High
4H-6, 122–127	Disturbance	
5H-1, 0–3	Disturbance	
5H-7, 52–56	Disturbance	
5H-CC, 0–25		Moderate
6H-1, 0–36	Thick soupy ash and disturbance	
6H-2, 140–145		
6H-CC, 0–22		Moderate
7H-1, 0–10	Disturbance	
7H-1, 15–15	Ash mixed layer	
7H-2, 80–80	Ice-rafted debris	
7H-5, 15–30	Microfault	
7H-5, 85–93	Microfault	
7H-CC, 0–29		Slight
8H-2, 125–135	Tilted	
8H-4, 92–139	Tilted	
8H-5, 110–150	Tilted	
8H-7, 16–32	Bowed	Moderate
8H-CC, 0–32		Slight
9H-1, 0–10	Disturbance	
9H-6, 89–150	Microfault	
9H-CC, 0–8		Slight
12H-4, 31–44	Deformed?	
12H-5, 6–8	Microfault	
13H-1, 0–42	Disturbance	
13H-2, 109–122	Tilted	
13H-2, 131–135	Tilted	
13H-3, 0–15	Disturbance	
13H-4, 36–41	Disturbance	
13H-7, 0–10	Disturbance	
14H-, 0–61	Suck in	Severe
14H-, 240–994	Suck in	Destroyed
15H-3, 23–70	Suck in	Severe
16H-1, 0–61	Suck in	Severe
16H-, 240–994	Suck in	Destroyed
17H-1, 0–70	Flow-in?	
17H-4, 0–all to bottom	Flow-in?	
17H-CC, 18–22		Moderate to high
18H-1, 0–15	Disturbance	
18H-2, 0–36	Fall-in	Moderate to high
19H-1, 0–20	Disturbance	
19H-CC, 0–29		Slight
20H-1, 0–25	Disturbance	
20H-3, 49–73	Flow-in	
20H-3, 115–140	Microfault	
20H-6, 83–95	Ash and deformed	
20H-CC, 0–23		Slight
21H-3, 0–83	Flow-in?	
21H-CC, 0–17		Slight
22H-6, 80–87	Tilted	
22H-CC, 16–20		Moderate

Table T14 (continued).

Core, section	Comments on disturbance	Drilling disturbance intensity
346-U1423B-		
1H-1, 0–3	Fall-in	Moderate
2H-1, 67–70	Void	Destroyed
2H-CC, 18–20		Slight
4H-1, 0–10	Soupy	Moderate to high
5H-1, 0–5		Slight
9H-1, 0–3		Destroyed
11H-1, 128–150		Slight
11H-7, 9–19		Slight
12H-CC, 0–19		Moderate
13H-CC, 0–4		Slight
14H-CC, 5–20		Moderate
15H-1, 0–6	Fall-in	Moderate
15H-CC, 0–4		Slight
15H-CC, 11–13		Slight
16H-1, 0–4		Slight
17H-1, 0–11	Fall-in	Moderate to high
17H-CC, 0–23		Slight
19H-1, 0–2		Slight
20H-CC, 10–18		Moderate
21H-CC, 0–2		Moderate
21H-CC, 7–13		Slight
22H-1, 0–4		Slight
22H-CC, 0–25		Slight
23H-1, 0–5		Slight
23H-CC, 0–4		Slight
24H-CC, 0–4		Slight
25H-1, 0–12		Slight to moderate
26H-7, 30–40		Slight
28H-4, 38–74		Slight to moderate
28H-6, 99–150		Slight to moderate
346-U1423C-		
2H-1, 0–20		Severe
2H-1, 131–138	Microfault	
2H-6, 0–8	Disturbance	
3H-3, 47–61	Disturbance	
3H-5, 0–12	Disturbance	
3H-CC, 17.5–20		Moderate
6H-1, 1–3		Moderate
6H-5, 1–5		Moderate
6H-CC, 16–20		High
8H-1, 77–82	Tilted	
8H-1, 122–130	Tilted	
8H-CC, 0–6		Moderate to high
8H-2, 121–126	Ash disturbed layer	
9H-6, 34–44	Tilted and mixed two different lithology	
9H-CC, 11–25		Moderate

Table T15. NRM inclination, declination, and intensity data after 20 mT peak field AF demagnetization, Site U1423.

Core, section, interval (cm)	Depth CSF-A (m)	Inclination (°)	Declination (°)	FlexIT-corrected declination (°)	Intensity (A/m)
346-U1423A-					
1H-1, 0	0				
1H-1, 5	0.05				
1H-1, 10	0.10				
1H-1, 15	0.15	62.8	59		0.024861
1H-1, 20	0.20	64.5	60.7		0.031384
1H-1, 25	0.25	68.6	79.2		0.039737
1H-1, 30	0.30	68.2	75.3		0.051894
1H-1, 35	0.35	72.1	82.4		0.058857
1H-1, 40	0.40	76.9	80.5		0.066982
1H-1, 45	0.45	77.4	58.8		0.089149
1H-1, 50	0.50	76.8	59.1		0.1255
1H-1, 55	0.55	74.7	67.9		0.11079
1H-1, 60	0.60	66.8	80.6		0.089831
1H-1, 65	0.65	67.8	86.4		0.083761
1H-1, 70	0.70	69.3	71.9		0.065555
1H-1, 75	0.75	68.1	62.2		0.062376
1H-1, 80	0.80	65.9	59.8		0.069185
1H-1, 85	0.85	65.2	59.7		0.056174
1H-1, 90	0.90	67.3	62.4		0.050081
1H-1, 95	0.95	65.5	76		0.048367
1H-1, 100	1.00	67	109.4		0.043859
1H-1, 105	1.05	67.2	108.3		0.041108
1H-1, 110	1.10	63.3	98.5		0.047328
1H-1, 115	1.15	64.1	97.7		0.054528
1H-1, 120	1.20	66.7	95.5		0.064302
1H-1, 125	1.25	65.7	95.6		0.06854
1H-1, 130	1.30	64.2	92.4		0.063498
1H-1, 135	1.35	60.7	93		0.056491
1H-1, 140	1.40				
1H-1, 145	1.45				
1H-1, 150	1.50				
1H-2, 0	1.50				
1H-2, 5	1.55				
1H-2, 10	1.60				
1H-2, 15	1.65	62.6	90.4		0.064971
1H-2, 20	1.70	65.5	84.3		0.070444
1H-2, 25	1.75	73.6	78.6		0.066624
1H-2, 30	1.80				
1H-2, 35	1.85	73.7	96.9		0.05686
1H-2, 40	1.90	74.4	94.5		0.054415
1H-2, 45	1.95	72.8	98.2		0.045478
1H-2, 50	2.00	74.8	100.6		0.035453
1H-2, 55	2.05	72.7	99.3		0.030256
1H-2, 60	2.10	67.2	95.3		0.030193
1H-2, 65	2.15	68.4	96.8		0.031033
1H-2, 70	2.20	68.3	84.2		0.03413
1H-2, 75	2.25	61.2	74.5		0.038089
1H-2, 80	2.30	62.4	80.3		0.040814
1H-2, 85	2.35	70.9	80.3		0.043866
1H-2, 90	2.40	66.2	53.6		0.059384
1H-2, 95	2.45	65	75		0.043951
1H-2, 100	2.50	63.7	107		0.031946
1H-2, 105	2.55	65.7	101.3		0.030403
1H-2, 110	2.60	71.9	81.2		0.042755
1H-2, 115	2.65	74.3	104.4		0.045477
1H-2, 120	2.70	74	88.2		0.03286
1H-2, 125	2.75				
1H-2, 130	2.80	72.2	106.6		0.034496
1H-2, 135	2.85	71.8	93.1		0.039783
1H-2, 140	2.90				
1H-2, 145	2.95				

Blank cells indicate depth levels where data were either not available (i.e., FlexIT-corrected declination data for nonoriented cores) or removed because of disturbance, voids, or measurement edge effects. Only a portion of this table appears here. The complete table is available in **ASCII.**

Table T16. Polarity boundaries, Site U1423.

Core, section, interval (cm)		Polarity boundary	Age (Ma)	Depth CSF-A (m)				Depth CCSF-D (m)			
Top	Bottom			Top	Bottom	Midpoint	±	Top	Bottom	Midpoint	±
346-U1423A-	346-U1423A-										
6H-5, ~45	6H-6, ~55	(B) C1n (Brunhes/Matuyama)	0.781	51.70	**53.30**	**52.50**	0.80	54.09	55.69	**54.89**	0.80
7H-2, ~10	7H-3, ~40	(T) C1r.1n (Jaramillo)	0.988	56.40	58.20	**57.30**	0.90	59.40	61.20	**60.30**	0.90
7H-5, ~20	7H-5, ~60	(B) C1r.1n (Jaramillo)	1.072	61.00	61.40	**61.20**	0.20	64.00	64.40	**64.20**	0.20
8H-7, ~45	9H-2, ~105	(T) C2n (Olduvai)	1.778	73.76	76.36	75.06	1.30	77.60	80.20	78.90	1.30
11H-2, ~130	11H-2, ~20	(B) C2n (Olduvai)	1.945	93.40	95.60	94.50	1.10	97.89	100.09	98.99	1.10
13H-1, ~80	13H-1, ~20	(B) C2r (Matuyama/Gauss)	2.581	111.40	112.60	112.00	0.60	116.30	117.50	116.90	0.60
346-U1423B-	346-U1423B-										
7H-1, ~10	7H-1, ~50	(B) C1n (Brunhes/Matuyama)	0.781	51.30	52.10	**51.70**	0.40	53.40	54.20	**53.80**	0.40
7H-5, ~130	7H-5, ~80	(T) C1r.1n (Jaramillo)	0.988	57.90	58.90	**58.40**	0.50	60.00	61.00	**60.50**	0.50
8H-1, ~150	8H-1, ~120	(B) C1r.1n (Jaramillo)	1.072	62.00	62.60	62.30	0.30	64.29	64.89	64.59	0.30
9H-4, ~110	9H-4, ~90	(T) C2n (Olduvai)	1.778	75.80	76.20	76.00	0.20	78.61	79.01	78.81	0.20
—	—	(B) C2n (Olduvai)	—	—	—	—	—	—	—	—	—
13H-4, ~150	13H-4, ~50	(B) C2r (Matuyama/Gauss)	2.581	112.60	114.60	113.60	1.00	117.80	119.80	118.80	1.00

Bold = boundaries that are relatively well defined. B = Bottom, T = top. — = not observed.

Table T17. Results from APCT-3 temperature profiles, Site U1423.

Core	Minimum temperature at mudline (°C)	Average temperature at mudline (°C)	Depth CSF-A (m)	In situ temperature (°C)	Thermal resistance (m^2K/W)
346-U1423A-					
4H	0.21	0.48	35.8	5.50	37.91
7H	0.23	0.43	64.3	9.55	68.03
10H	0.22	0.47	92.8	13.54	98.10
13H	0.24	0.48	121.3	17.45	128.12
Average:	0.23	0.47			

In situ temperatures were determined using TP-Fit software by Martin Heesemann. Thermal resistance was calculated from thermal conductivity data (see **"Physical properties"**) corrected for in situ conditions (see **"Downhole measurements"** in the "Methods" chapter [Tada et al., 2015b]).

Table T18. Vertical offsets required to correlate specific features among cores from adjacent holes, Site U1423.

Core	Vertical offset (m)	Y/N
346-U1423A-		
1H	0	N
2H	0.474	Y
3H	0.862	Y
4H	1.537	Y
5H	2.135	Y
6H	2.387	Y
7H	3.001	Y
8H	3.599	Y
9H	3.835	Y
10H	4.185	Y
11H	4.488	Y
12H	4.006	Y
13H	4.903	Y
14H	4.977	Y
15H	5.439	Y
16H	6.317	Y
17H	6.341	Y
18H	6.830	Y
19H	7.480	Y
20H	7.615	Y
21H	7.914	Y
22H	8.091	Y
346-U1423B-		
1H	0.233	Y
2H	0.435	Y
3H	0.804	Y
4H	1.161	Y
5H	1.432	Y
6H	2.135	Y
7H	2.104	Y
8H	2.286	Y
9H	2.811	Y
10H	3.548	Y
11H	4.278	Y
12H	4.740	Y
13H	5.198	Y
14H	5.782	Y
15H	5.886	Y
16H	5.549	Y
17H	6.274	Y
18X	6.274	N
19H	6.907	Y
20H	7.188	Y
21H	7.082	Y
22H	7.211	Y
23H	7.446	Y
24H	7.616	Y
25H	7.616	N
26H	7.616	N
27H	7.616	N
28H	7.616	N
346-U1423C-		
2H	6.417	Y
3H	6.708	Y
4H	6.095	Y
5X	5.978	Y
6H	6.194	Y
7X	6.194	N
8H	6.373	Y
9H	7.908	Y

Table T19. Splice intervals, Site U1423.

Hole, core, section	Depth in section (cm)	Depth CSF-A (m)	Depth CCSF-D (m)	Hole, core, section	Depth in section (cm)	Depth CSF-A (m)	Depth CCSF-D (m)	Data used to tie
346-				346-				
U1423A-1H-1	0.0	0.00	0.00	U1423A-1H-5	74.5	6.74	6.74	Blue
U1423B-2H-2	71.0	6.31	6.74	U1423B-2H-6	136.7	12.97	13.40	Blue
U1423A-2H-4	112.9	12.93	13.40	U1423A-2H-6	126.4	16.06	16.54	Blue
U1423B-3H-2	63.4	15.73	16.54	U1423B-3H-7	30.3	22.90	23.71	Blue
U1423A-3H-5	4.5	22.84	23.71	U1423A-3H-7	1.2	25.81	26.67	Blue
U1423B-4H-2	91.3	25.51	26.67	U1423B-4H-7	41.1	32.48	33.64	Blue
U1423A-4H-4	135.4	32.10	33.64	U1423A-4H-6	142.5	35.17	36.71	Blue
U1423B-5H-2	118.0	35.28	36.71	U1423B-5H-6	134.8	41.45	42.88	Blue
U1423A-5H-4	44.5	40.75	42.88	U1423A-5H-7	11.4	44.72	46.86	Blue
U1423B-6H-2	112.4	44.72	46.86	U1423B-6H-6	63.4	50.23	52.37	Blue
U1423A-6H-4	23.2	49.98	52.37	U1423A-6H-7	8.0	54.14	56.53	Blue
U1423B-7H-2	132.3	54.42	56.53	U1423B-7H-6	129.6	60.40	62.50	Blue
U1423A-7H-4	19.9	59.50	62.50	U1423A-7H-6	87.9	63.18	66.18	Blue
U1423B-8H-2	129.3	63.89	66.18	U1423B-8H-6	86.9	69.47	71.76	Blue
U1423A-8H-3	85.7	68.16	71.76	U1423A-8H-6	89.5	72.69	76.29	Blue
U1423B-9H-2	138.3	73.48	76.29	U1423B-9H-7	16.6	79.77	82.58	Blue
U1423A-9H-4	44.1	78.74	82.58	U1423A-9H-6	137.0	82.67	86.51	Blue
U1423B-10H-2	139.7	82.96	86.51	U1423B-10H-6	48.4	88.04	91.59	Blue
U1423A-10H-3	110.8	87.41	91.59	U1423A-10H-7	12.4	92.42	96.61	Blue
U1423B-11H-2	123.1	92.33	96.61	U1423B-11H-6	109.5	98.19	102.47	Blue
U1423A-11H-4	68.5	97.99	102.47	U1423A-11H-6	144.6	101.75	106.23	Blue
U1423B-12H-2	89.4	101.49	106.23	U1423B-12H-7	15.5	108.25	112.99	Blue
U1423A-12H-5	68.8	108.99	112.99	U1423A-12H-7	17.2	111.47	115.48	Blue
U1423B-13H-2	18.0	110.28	115.48	U1423B-13H-5	114.8	115.75	120.95	Blue
U1423A-13H-3	124.3	116.04	120.95	U1423A-13H-6	62.3	119.92	124.83	Blue
U1423B-14H-1	94.5	119.04	124.83	U1423B-14H-5	118.9	125.29	131.07	Blue
U1423A-14H-4	29.4	126.09	131.07	U1423A-14H-7	64.5	130.94	135.92	Blue
U1423B-15H-2	93.5	130.04	135.92	U1423B-15H-3	95.8	131.56	137.44	Blue
U1423A-15H-1	120.6	132.01	137.44	U1423A-15H-6	36.2	138.67	144.11	Blue
U1423C-4H-4	51.6	138.02	144.11	U1423C-4H-6	136.6	141.87	147.96	Blue
U1423A-16H-1	134.3	141.64	147.96	U1423A-16H-2	94.4	142.74	149.06	Blue
U1423B-17H-1	68.7	142.79	149.06	U1423B-17H-6	146.6	151.07	157.34	Blue and GRA
U1423C-6H-1	114.6	151.15	157.34	U1423C-6H-7	20.0	159.25	165.44	MS point
U1423B-19H-1	43.8	158.54	165.44	U1423B-19H-6	3.0	165.60	172.51	GRA
U1423A-18H-5	57.8	165.68	172.51	U1423A-18H-7	30.5	168.41	175.23	Blue
U1423B-20H-1	44.7	168.05	175.23	U1423B-20H-5	134.0	174.94	182.13	Blue
U1423A-19H-5	4.7	174.65	182.13	U1423A-19H-7	3.2	177.63	185.11	Blue
U1423B-21H-1	93.1	178.03	185.11	U1423B-21H-4	53.4	182.13	189.22	Blue
U1423A-20H-3	50.1	181.60	189.22	U1423A-20H-6	27.1	185.87	193.49	MS and GRA
U1423B-22H-3	67.5	186.27	193.49	U1423B-22H-7	18.0	191.78	198.99	GRA
U1423A-21H-3	47.7	191.08	198.99	U1423A-21H-5	148.2	195.08	203.00	GRA
U1423B-23H-3	45.0	195.55	203.00	U1423B-23H-6	127.1	200.87	208.32	GRA
U1423A-22H-3	12.6	200.23	208.32	U1423A-22H-6	68.1	205.28	213.37	GRA
U1423B-24H-3	115.5	205.76	213.37	U1423B-24H-7	0.6	211.25	218.80	

GRA = gamma ray attenuation, MS = magnetic susceptibility, Blue = RGB blue datum, MS point = point magnetic susceptibility.

Table T20. CCSF-C depth scale, Holes U1423A and U1423B.

Hole U1423A					Hole U1423B				
Core, section	Depth in section (cm)	Depth CCSF-C (m)	RGB (Blue)	Depth CSF-A (m)	Core, section	Depth in section (cm)	Depth CCSF-C (m)	RGB (Blue)	Depth CSF-A (m)
346-U1423A-					346-U1423B-				
1H-1	5	0.05	18.00	0.05	1H-1	5	0.23	27.80	0.05
1H-1	5.5	0.06	27.00	0.06	1H-1	5.5	0.23	27.90	0.06
1H-1	6	0.06	29.60	0.06	1H-1	6	0.22	28.30	0.06
1H-1	6.5	0.07	30.80	0.07	1H-1	6.5	0.22	28.60	0.07
1H-1	7	0.07	29.90	0.07	1H-1	7	0.22	28.30	0.07
1H-1	7.5	0.08	31.00	0.08	1H-1	7.5	0.22	29.20	0.08
1H-1	8.01	0.08	31.20	0.08	1H-1	8.01	0.22	29.30	0.08
1H-1	8.51	0.09	30.40	0.09	1H-1	8.51	0.22	28.50	0.09
1H-1	9.01	0.09	29.20	0.09	1H-1	9.01	0.22	28.90	0.09
1H-1	9.51	0.10	29.10	0.10	1H-1	9.51	0.22	28.70	0.10
1H-1	10.01	0.10	31.00	0.10	1H-1	10.01	0.22	29.60	0.10
1H-1	10.51	0.11	32.70	0.11	1H-1	10.51	0.22	30.40	0.11
1H-1	11.01	0.11	30.50	0.11	1H-1	11.01	0.22	30.90	0.11
1H-1	11.51	0.12	21.90	0.12	1H-1	11.51	0.22	25.30	0.12
1H-1	12.01	0.12	20.90	0.12	1H-1	12.01	0.22	27.50	0.12
1H-1	12.51	0.13	16.00	0.13	1H-1	12.51	0.22	21.80	0.13
1H-1	13.01	0.13	17.00	0.13	1H-1	13.01	0.21	19.60	0.13
1H-1	13.51	0.14	15.80	0.14	1H-1	13.51	0.21	18.20	0.14
1H-1	14.01	0.14	18.80	0.14	1H-1	14.01	0.21	16.90	0.14
1H-1	14.51	0.15	19.80	0.15	1H-1	14.51	0.21	17.40	0.15
1H-1	15.01	0.15	29.80	0.15	1H-1	15.01	0.21	17.60	0.15
1H-1	15.51	0.16	29.10	0.16	1H-1	15.51	0.21	15.70	0.16
1H-1	16	0.16	22.60	0.16	1H-1	16	0.21	16.10	0.16
1H-1	16.5	0.17	26.30	0.17	1H-1	16.5	0.21	22.40	0.17
1H-1	17	0.17	26.60	0.17	1H-1	17	0.21	24.70	0.17
1H-1	17.5	0.18	30.40	0.18	1H-1	17.5	0.21	30.80	0.18
1H-1	18	0.18	31.60	0.18	1H-1	18	0.21	28.70	0.18
1H-1	18.5	0.19	37.00	0.19	1H-1	18.5	0.21	28.90	0.19
1H-1	19	0.19	33.70	0.19	1H-1	19	0.21	30.20	0.19
1H-1	19.5	0.20	36.80	0.20	1H-1	19.5	0.21	31.80	0.20
1H-1	20	0.20	34.80	0.20	1H-1	20	0.20	34.70	0.20
1H-1	20.5	0.21	35.80	0.21	1H-1	20.5	0.20	31.10	0.21
1H-1	21	0.21	37.00	0.21	1H-1	21	0.20	28.50	0.21
1H-1	21.5	0.22	37.60	0.22	1H-1	21.5	0.20	22.40	0.22
1H-1	22	0.22	35.50	0.22	1H-1	22	0.20	21.70	0.22
1H-1	22.5	0.23	36.20	0.23	1H-1	22.5	0.20	25.20	0.23
1H-1	23	0.23	32.20	0.23	1H-1	23	0.20	23.30	0.23
1H-1	23.5	0.24	30.50	0.24	1H-1	23.5	0.20	24.70	0.24
1H-1	24	0.24	29.80	0.24	1H-1	24	0.20	26.80	0.24
1H-1	24.5	0.25	33.50	0.25	1H-1	24.5	0.20	29.30	0.25
1H-1	25	0.25	33.90	0.25	1H-1	25	0.20	27.20	0.25
1H-1	25.5	0.26	34.00	0.26	1H-1	25.5	0.20	24.60	0.26
1H-1	26	0.26	32.80	0.26	1H-1	26	0.20	21.00	0.26
1H-1	26.5	0.27	29.40	0.27	1H-1	26.5	0.20	22.60	0.27
1H-1	27	0.27	27.00	0.27	1H-1	27	0.19	24.30	0.27
1H-1	27.5	0.28	22.20	0.28	1H-1	27.5	0.19	26.20	0.28
1H-1	28	0.28	25.00	0.28	1H-1	28	0.19	30.70	0.28
1H-1	28.5	0.29	27.60	0.29	1H-1	28.5	0.19	28.30	0.29
1H-1	29	0.29	24.70	0.29	1H-1	29	0.19	30.60	0.29
1H-1	29.5	0.30	29.60	0.30	1H-1	29.5	0.19	30.50	0.30
1H-1	30	0.30	27.10	0.30	1H-1	30	0.19	31.00	0.30
1H-1	30.5	0.31	31.30	0.31	1H-1	30.5	0.19	31.00	0.31
1H-1	31	0.31	31.50	0.31	1H-1	31	0.19	30.60	0.31
1H-1	31.5	0.32	29.00	0.32	1H-1	31.5	0.19	29.50	0.32
1H-1	32.01	0.32	28.20	0.32	1H-1	32.01	0.19	32.40	0.32
1H-1	32.51	0.33	28.10	0.33	1H-1	32.51	0.19	29.80	0.33
1H-1	33.01	0.33	28.30	0.33	1H-1	33.01	0.19	31.80	0.33
1H-1	33.51	0.34	27.80	0.34	1H-1	33.51	0.19	29.30	0.34
1H-1	34.01	0.34	28.00	0.34	1H-1	34.01	0.20	29.20	0.34
1H-1	34.51	0.35	27.10	0.35	1H-1	34.51	0.20	29.50	0.35
1H-1	35.01	0.35	27.90	0.35	1H-1	35.01	0.21	29.80	0.35

Only a portion of this table appears here. The complete table is available as **ASCII.**